FLAME STABILIZATION AND MIXING CHARACTERISTICS IN A STAGNATION POINT REVERSE FLOW COMBUSTOR

A Dissertation
Presented to
The Academic Faculty

by

Mohan K. Bobba

In Partial Fulfillment
of the Requirements for the Degree
Doctor of Philosophy in
Aerospace Engineering

Georgia Institute of Technology

December 2007

FLAME STABILIZATION AND MIXING CHARACTERISTICS IN A STAGNATION POINT REVERSE FLOW COMBUSTOR

Approved By:

Dr. Jerry M. Seitzman, Advisor
Associate Professor
School of Aerospace Engineering
Georgia Institute of Technology

Dr. Timothy C. Lieuwen
Associate Professor
School of Aerospace Engineering
Georgia Institute of Technology

Dr. Ben T. Zinn
Regents Professor, David S. Lewis Chair
School of Aerospace Engineering
Georgia Institute of Technology

Dr. Samuel V. Shelton
Associate Professor
School of Mechanical Engineering
Georgia Institute of Technology

Dr. Jechiel J. Jagoda
Professor, Associate Chair for Graduate Studies and Research
School of Aerospace Engineering
Georgia Institute of Technology

Dr. Sergei Filatyev
Heavy Oil Research and Development
ConocoPhillips

Date Approved: 2nd October 2007

To my parents

ACKNOWLEDGEMENTS

I would like to thank, first and foremost, my advisor Dr. Jerry M. Seitzman for his guidance and support throughout my graduate career. His enthusiasm and passion for research has inspired me all along and I could not have imagined having a better mentor. I am also extremely grateful to the members of my committee, Dr. Ben Zinn, Dr. Jeff Jagoda, Dr. Tim Lieuwen, Dr. Samuel Shelton and Dr. Sergei Filatyev, for their input and interest in this research.

I would like to thank Jayaprakash, Murgi, Priya, Satish, Preetham, Thao, Santosh S, Nelson, Santosh H, Qingguo, and Suraj for their help. I have learnt a lot from the discussions I had with them. I am also indebted to Karthik for all the assistance with acquiring and processing the data presented in this thesis.

Special thanks to Master Nils Onsager and others from the martial arts school for their friendship and helping me take my mind off from research when I was overwhelmed. Also thanks to my wonderful roommates, Kapil, Mudhakar and Rajeev, who have encouraged me at every step and made my stay at GeorgiaTech delightful. Finally, I would like to express my deepest gratitude to my parents and family for their constant encouragement and love throughout my educational pursuit.

TABLE OF CONTENTS

LIST OF TABLES

LIST OF FIGURES

SUMMARY

Gas turbine combustors have been driven towards leaner, premixed operation in order to meet increasingly stringent emission regulations. Premixing fuel and air in lean proportions lowers peak flame temperatures and thereby reduces NO_x emissions. Premixing, however, can lead to undesirable phenomenon like autoignition and very lean premixed operation can adversely impact combustor stability, e.g., through enhanced susceptibility to blowout. To address these issues, a novel combustor design, referred to as the Stagnation-Point Reverse-Flow (SPRF) combustor was recently developed. This combustor is able to operate stably at very lean fuel-air mixtures and with low NO_x emissions (around 1 ppm referenced at 15% excess O_2) even when the fuel and air are not premixed before entering the combustor, making it an exciting option for ground power and aircraft gas turbines.

The primary objective of this work is to elucidate the underlying physics behind the excellent stability and emissions performance of the SPRF combustor. The approach is to experimentally characterize velocities, species mixing, heat release and flame structure in an atmospheric pressure SPRF combustor with the help of various optical diagnostic techniques: OH Planar Laser-Induced Fluorescence (PLIF), chemiluminescence imaging, Particle Image Velocimetry (PIV) and Spontaneous Raman Scattering (SRS).

Results indicate that the combustor is primarily stabilized in a region downstream of the injector that is characterized by low average velocities and high turbulence levels; this is also the region where most of the heat release occurs. High turbulence levels in the shear layer lead to increased product entrainment levels, elevating the reaction rates and

thereby enhancing the combustor stability. Here product entrainment is quantified by the product fraction (f_P), defined as the ratio of the measured product gas mass to the reactant mass in a fluid element entering the flame zone. The effect of product entrainment on chemical timescales and the flame structure is illustrated with simple reactor models. Although reactants are found to burn in a highly preheated (1300 K) and turbulent environment due to mixing with hot product gases, the residence times are sufficiently long compared to the ignition timescales such that the reactants do not autoignite. Turbulent flame structure analysis indicates that the flame is primarily in the thin reaction zones regime throughout the combustor, and it tends to become more flamelet like with increasing distance from the injector.

Fuel-air mixing measurements in case of non-premixed operation indicate that the fuel is shielded from hot products until it is fully mixed with air, providing nearly premixed performance without the safety issues associated with premixing. Exhaust gas recirculation in the combustor does not seem to have a significant effect on the NO_x emission levels. Therefore, the reduction in NO_x emissions in the SPRF combustor are primarily due to its ability to stably operate under ultra lean (and nearly premixed) condition within the combustor. Further, to extend the usefulness of this combustor configuration to various applications, combustor geometry scaling rules were developed with the help of simplified coaxial and opposed jet models.

CHAPTER 1

INTRODUCTION AND MOTIVATION

1.1 Introduction

The drive towards reduced pollutant emissions has prompted the gas turbine industry to develop cleaner, more environmentally friendly power and propulsion systems, while simultaneously maintaining (or improving) efficiency, operability and performance. The production of at least one of the regulated emissions, oxides of nitrogen or NOx, tends to be a strong function of flame temperature and of the residence time that combustion products have in regions of high temperature. Among the mechanisms by which NO_x is formed [1,2], the most prominent at the high temperatures found in many combustion systems, is the Zeldovich mechanism [3], also known as the thermal NO_x mechanism. For a given O_2/N_2 ratio, the amount of thermal NO_x produced at a temperature of around 1800 K in a few seconds is comparable to the NO_x produced in just a few milliseconds when the temperature is closer to 2100 K [3].

Lean premixed combustion systems have been used to lower flame temperatures and to avoid stoichiometry non-uniformities that arise due to incomplete mixing of fuel and air. The goal is to limit peak flame temperatures below a value where thermal NO_x production is greatly reduced, for example 1800 K. However, operation of these premixed systems can lean to undesired phenomenon like autoignition and flashback. High temperatures in a premixer caused by autoignition or flashback can result in damage or shutdown of an engine. Hence, it is advantageous if fuel and air can be injected into the combustor separately and then allowed to mix rapidly before they burn. The main

means of achieving this are through careful design of the aerodynamics of burners and enclosures, and thus control over the mixing mechanisms and residence time. For example, high velocity coaxial air in jet diffusion flames has been successfully demonstrated to reduce NO_x emission levels in hydrocarbon flames [4]. Enhanced shear produced by the high velocity coaxial air results in enhanced mixing between fuel and air before combustion and also lowers the residence times resulting in lower emission levels. Another attractive scheme for NO_x reduction is staged combustion with staging performed on either the introduction of fuel [5] or air [6]. By introducing fuel or air at multiple stages, the combustion can occur at completely fuel rich or lean proportions, with subsequent rapid mixing with excess air to minimize NO_x production. But implementation of this technology requires sophisticated designs with increased capital investment.

An alternative approach to lowering NOx is flue gas recirculation (FGR). Dilution of the reactants with *cooled*, (inert) combustion products lowers the oxygen concentration before combustion and the final flame temperature; together, these tend to lengthen the ignition delay [7]. With sufficient FGR, the combustion zone can be spread out over the entire mixing region rather than in a thin front. The increased ignition delay also allows sufficient time for premixing of fuel and air (in nonpremixed systems) before burning occurs. The result is a more uniform temperature distribution that helps to lower NO_x levels. However, these combustors are prone to loss of static stability, as the combustion process is weakened due to mixing with cold inert gases.

To meet these conflicting requirements of for low emissions and high static stability, a simple and compact combustor design called the Stagnation-Point Reverse-

Flow (SPRF) combustor, incorporating some of the above mentioned methodologies, has recently been demonstrated [8]. The combustor design consists of a tube that is open at one end and closed at the other. As seen in the flow schematic of the combustor in Figure 1, the reactants are injected along the combustor center line without any swirl, while the products flow in the reverse direction to exit the combustor. Products leaving the combustor flow over the injector, providing "internal" preheating of the reactants before injection.

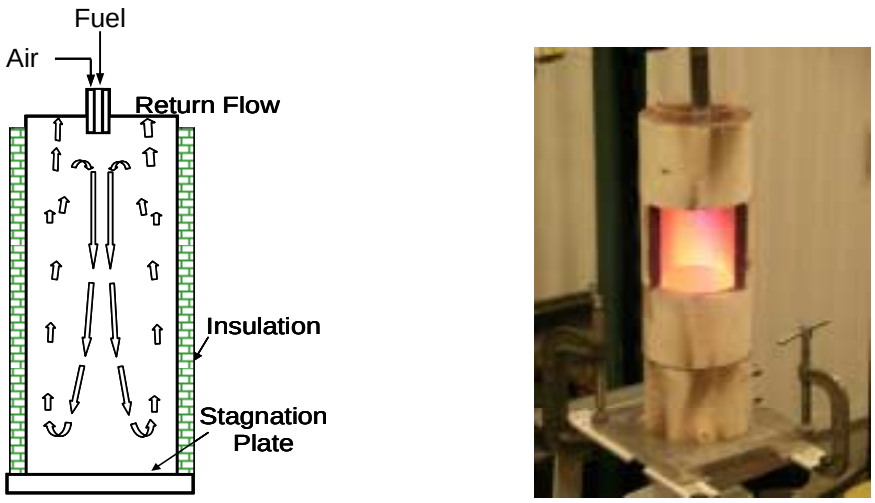

Figure 1. Schematic of the SPRF combustor and photograph of the combustor operating on natural gas.

1.2 Motivation

The SPRF configuration has been shown to operate *stably* with ultra low NO_x emissions in both premixed and non-premixed modes of operation over a wide range of combustor operating conditions. Figure 2a shows NO_x emissions at the exit of the premixed SPRF combustor for various equivalence ratios plotted as a function of the adiabatic flame temperature. The NO_x emissions measured in this combustor are found to

be below 1 ppm for the leanest operating condition (ϕ~0.51). For comparison, the figure also shows NO_x levels from a laminar, one-dimensional, premixed flame, based on a CHEMKIN simulation and the GRIMech 3.0 mechanism [9] over a range of equivalence ratios. The model results represent the NO_x produced in the flame front, i.e., where the heat release has dropped to 1% of its peak value, as opposed to thermal NO_x produced in the product gases. In this sense, the model results represent a minimum expected emission level for a premixed flame at a given stoichiometry. The measured emissions from the combustor are reasonably close to the minimum levels, until the flame temperatures exceed ~1800-1900 K, where thermal NO_x formation in the post-flame region is expected to become significant. While the NO_x emissions are comparable to other premixed combustors, the SPRF combustor is able to produce a compact, stable flame even under very lean conditions, without external preheating or swirl. For example, the leftmost point in Figure 2a was acquired with the combustor operating at ϕ=0.51 and with a combustor power density of 20 MW/m^3 (at atmospheric pressure). At these conditions, the combustor is still stable. This is very close to the lean flammability limit of ϕ = 0.46 for methane at room temperature [10].

Another key feature of the SPRF combustor is its inherent flexibility to operate in both premixed and non-premixed modes. The emissions levels obtained in non-premixed mode were found to be very close to those obtained in the premixed mode of operation, as shown in Figure 2b. Again, it is seen that loading does not have a significant effect on the emission levels. Since premixing requires added hardware and introduces the possibility of flashback or autoignition in the premixer, non-premixed operation is definitely advantageous.

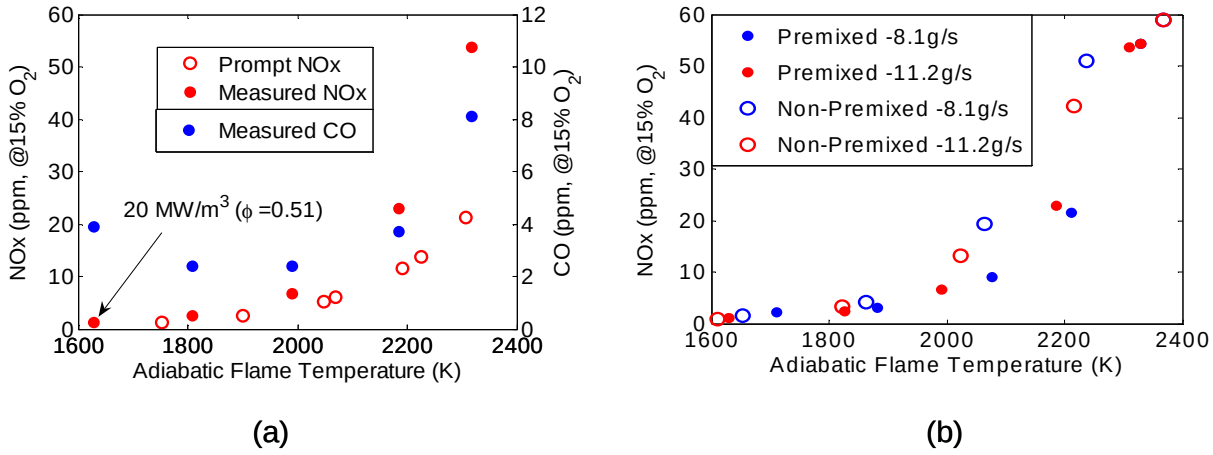

Figure 2. Variation of NOx emissions with adiabatic flame temperature based on overall equivalence ratio and measured inlet temperature in (a) premixed case in comparison to a laminar flame model and (b) in non-premixed mode in comparison to the premixed case.

1.3 Overview of Present Work

The present investigation examines features of the Stagnation Point Reverse Flow (SPRF) combustor that contribute to its stability and low NO_x emissions even with non-premixed fuel injection. The requirements for good emission performance and flame stability for both non-premixed and premixed modes are closely associated with local flow and burning velocities, and mixture preparation. To this end, combustion and mixing processes in this unique reverse flow configuration that have a profound effect on the performance and flame stability are surveyed.

Specifically, this effort focuses on 1) characterizing reactant-product mixing for premixed combustion and additionally fuel-air mixing for nonpremixed operation of the combustor, and 2) determination of the combustion and flow field characteristics that lead to the combustor's robust flame stabilization. To further the usefulness of this

combustor configuration to various applications, this thesis also investigates 3) the effect of combustor geometry and operating condition changes on the mixing characteristics and thereby the combustor performance.

Chapter 2 of the thesis provides a brief background and review of literature relevant to the current work. The experimental facility, instrumentation and the data analysis techniques used for the measurements reported are outlined in Chapter 3. The combustor configurations and conditions are also discussed there. Chapter 4 details the investigation of the flame stabilization mechanisms in the premixed SPRF combustor. Chapter 5 covers fuel-air mixing in the non-premixed operation of the combustor. In addition, it also includes the effect of scaling various combustor dimensions on the mixing characteristics. Lastly, conclusions and suggestions for future research are presented in Chapter 6.

CHAPTER 2

BACKGROUND

This chapter provides a brief background of various concepts that provide a basis for the ideas presented in this thesis. The first section describes different factors that affect flame stability and methodologies for stability enhancement, while the second section describes stabilization mechanisms in a turbulent jet flame. The next two sections outline features of mixing and jet penetration in coaxial and counter flow jets. Lastly, an overview of different diagnostics used in the past to study flame and mixing characteristics is provided.

2.1 Flame Stability

One of the major challenges facing designers of low NO_x combustion systems (like lean premixed combustion and flue gas recirculation) is flame stability; as the weaker combustion process is more vulnerable to small perturbations in combustor operating conditions. Since further reduction of NO_x will likely require even leaner (or more diluted) mixtures, schemes for lean stability extension must be considered.

Stability of the combustor is linked to the type of combustion process that occurs within it. If the burning occurs in a thin flame zone that is mixing limited, combustor stability can be dependent on the balance between flow and flame propagation velocities. In combustors where combustion is limited by reaction rates, for example a stirred reactor, the stability at a given stoichiometry is primarily limited by the residence time. However, practical combustors do not operate in either limit. The relative importance of

reaction to the mixing timescales in a combustor is usually expressed in terms of the Dahmkohler number (*Da*). Knowledge of this quantity can helps us conceptualize, model and identify the parameters that control static stability of a given combustor.

Due to engine flow rate requirements, the injection velocities in a typical combustor are usually a few orders of magnitude higher than laminar flame propagation velocities. Therefore, to stabilize a flame in the desired region of interest, various stabilization methodologies are adopted that either enhance the flame propagation speeds or create zones with low velocities where a flame can be sustained, or do both. Many designs are used by combustion researchers to create low velocity zones, including bluff body and swirl arrangements, where a flame can be sustained in the recirculation zone, and turbulent jets, where the flame is stabilized in the low velocity shear layer. On the other hand, various schemes for enhancement of reaction rates, including reactant preheating, exhaust gas recirculation or the use of an ignition source like a pilot flame to make the flame more stable, have been explored.

Gupta [11,12] reported that flames with highly preheated combustion air were much more stable and homogeneous (both temporally and spatially) as compared to room-temperature combustion air and hence could operate at much leaner equivalence ratios. However, by this approach the reduction in NO_x emission levels due to leaner operation is partially offset by the increased flame temperature due to preheating. Alternatively in a recent paper, Kalb *et al*. [13] suggested that stability can also enhanced by Exhaust Gas Recirculation (EGR), which involves mixing reactants with hot combustion products laden with radicals prior to combustion. They argued that the presence of radicals in the mixture lowers its ignition temperature and, thus, allows stable

combustion of mixtures that would otherwise not be flammable. Unlike simple reactant preheating, where the adiabatic flame temperature is increased, in EGR the reactants reach a high preheat temperature due to mixing with hot (adiabatic) products while maintaing a fixed adiabatic flame temperature. Hence, premixing the reactants with radicals to lower the combustion process temperature should allow low temperature combustion and therefore ultra low NO_x emissions.

Very high levels of internal recirculation in combustors, combined with other restrictions such as significant combustor heat loss, can lead to a process called "mild combustion," where no visually distinct flame is observed [13,14]. In these combustors with extensive exhaust gas recirculation, the amount of product entrainment is typically quantified by a single quantity such as the product fraction (f_P), which is normally defined to be the ratio of mass flow rate of products to that of the reactants previous to reactant combustion;

$$f_P = \frac{\dot{m}_E}{\dot{m}_F + \dot{m}_A}$$

where the subscripts, E, F and A stand for recirculated exhaust gas, fuel and combustion air.

Wunning *et al*. [15] have identified flame stability limits for furnace combustors over a range of recirculation ratios and process temperatures. In their work, when air injected into the furnace is mixed with products, they suggested that stable flames are possible over a range of combustor chamber temperature if the air is not significantly vitiated ($f_P < 0.3$). For moderately high recirculation rates ($0.3 < f_P < 2.5$), they found the flame becomes unstable and is found to lift-off and finally blowout. If the diluted air temperature is over the fuel autoignition temperature and the recirculation ratio (f_P)

exceeds 2.5, the fuel can react in a very stable form of combustion known as 'flameless oxidation'. Although operation in this mode provides reduction in NO_x emissions by facilitating combustion at an ultra lean stoichiometry, the reduced burning intensity demands large combustion chambers that are undesirable in applications where space and weight come at a premium.

2.2 Turbulent Jet Flames

Turbulent jet flames are employed in wide range of practical combustion systems due to simplicity of the configuration and the ease with which they can be controlled. The flame in this arrangement is stabilized in the shear layers where velocities are low. With increased injection velocity this low velocity region occurs too close to the wall where the flame speeds drops due to heat and radical losses. Hence premixed flames typically cannot be stabilized in the fully turbulent regime (Re>2000) without the use of supplementary stabilization source like a pilot flame. For non-premixed flames on the other hand, the diffusion flame formed at low jet velocities starts to detach from the burner and can stabilize as a lifted flame when the velocity is increased. Most of the jet flame research work in the past is focused on these non-premixed flames due to a wider range of injector velocities over which the flame can be stable. Global parameters of these flames, such as entrainment rates and flame length, have been extensively studied for over 60 years [16,17]. The lift off phenomenon has been modeled as both the limiting cases of turbulent premixed flame propagation [18] and a laminar diffusion flamelet [19]. However liftoff height prediction from these theories was not able to explain the experimental data comprehensively.

With recent advances in reaction zone imaging, this question of the lifted flame stabilization has been revisited and stabilization at the base of a lifted flame is found to be due to a partially premixed turbulent leading edge flame as shown in Figure 3 [20]. Models based on this assumption have been able to successfully predict jet flame liftoff heights. The flame liftoff facilitates mixing of the injected fuel jet with the ambient oxidizer as shown in Figure 3, while the velocity of the jet decays due to momentum transfer to the ambient gases. The flame is lifted off to a region where the propagation velocity in the partially premixed mixture is able to counter the local flow velocities. Detailed velocity measurements in these flames indicated that base of the flame resides in low speed regions typically with velocities $U_{base}<3S_L$ (S_L is the maximum laminar flame speed of the fuel-air mixture) [21]. However, with a further increase in jet velocity (to the blow off velocity) the lifted flame also tends to blow off just like a premixed flame.

Figure 3. Fuel concentration distribution in a lifted turbulent jet flame from Mungal et al. [20] with the flame location superimposed on it.

2.3 Coaxial Jet Mixing

The coaxial jet configuration, consisting of turbulent jets issuing from two round coaxial nozzles as shown in Figure 4, represents a flowfield of interest in many engineering applications related to mixing tanks and combustion chambers. Coaxial jets differ from annular jets in that the former has a central or a primary core. This increases the jet turbulence complexity as there are two potential cores and two mixing regions that can interact. The velocity ratio U_a/U_f, where U_a and U_f are the velocity of the annular and central streams, is the most important parameter in determining the flow pattern in these jets.

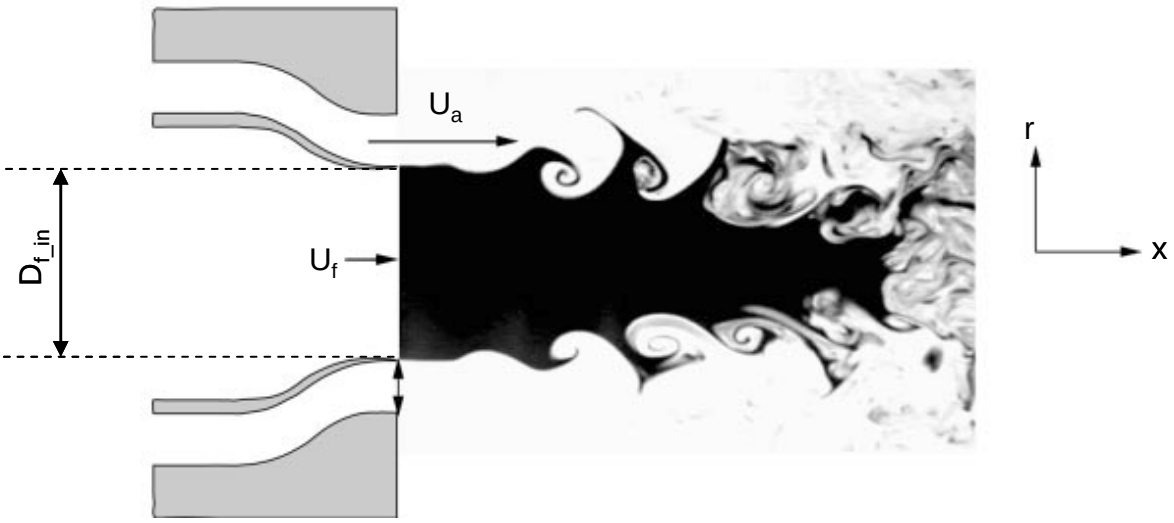

Figure 4. Sketch of the injector outlets and development of the flow [24].

Coaxial jets with a high annular to central jet velocity ratio are typically preferred for their ability to destabilize the inner jet and rapidly mix in short distances. The development of instabilities resulting from the interaction of the two nearby shear layers (one between the inner jet and outer jet, and the other between the outer jet and the surrounding medium) have been investigated in single phase coaxial jets [22]. The initial

region of the coaxial jets consist of two trains of vortex rings in the outer as well as inner mixing regions that are similar to the vortical motions in a single jet[23], and much of the mixing in these jets takes place in the developing region containing the potential cores.

Different regimes in the near field mixing of coaxial jets were studied in detail by Villermaux [24] for varying velocity ratios. Entrainment of air into the fuel jet can be quantified in terms of an entrainment velocity defined as the size of a given structure multiplied by the rate at which the structures are shed from the interface (but not necessarily mixed at molecular levels). For high velocity ratio jets ($U_a/U_f>>1$), the entrainment velocity tends toward, and can be approximated by, the outer air jet velocity (U_a) [24]. The extent of mixing in a coaxial jet system is typically defined in terms of a dilution length, defined as the axial distance by which the fuel jet dilutes down to a specified concentration level. This dilution length as estimated by Villermaux from the entrainment velocity and fuel iso-concentration contours is a function of the fuel jet diameter and the ratio of jet velocities.

$$L_d \sim D_{f\_in}\left(\frac{U_f}{U_a}\right)\left(\frac{C_o}{C_S}\right)$$

where C_o is the fuel concentration at the inner jet exit and C_s is the selected dilution level. This reasoning has been generalized to situations where the jets have different incoming densities, where the square root of the momentum ratio replaces the ratio of velocities.

2.4 Circular Jet in Counter-Flow

Turbulent mixing and dispersion of jets into a stagnant ambient has been extensively studied, however the counterflow case has received little attention. Preliminary mean velocity fields in a circular jet against a counterflow measured with

Pitot-static probes were reported in the Russian literature in the 1960's. Beltaos and Rajaratnam [25] have presented a conclusive review of the understanding based on these results. They found that the jet had a specific penetration length into the counter flow, beyond which the jet was deflected backward, as shown in Figure 5.

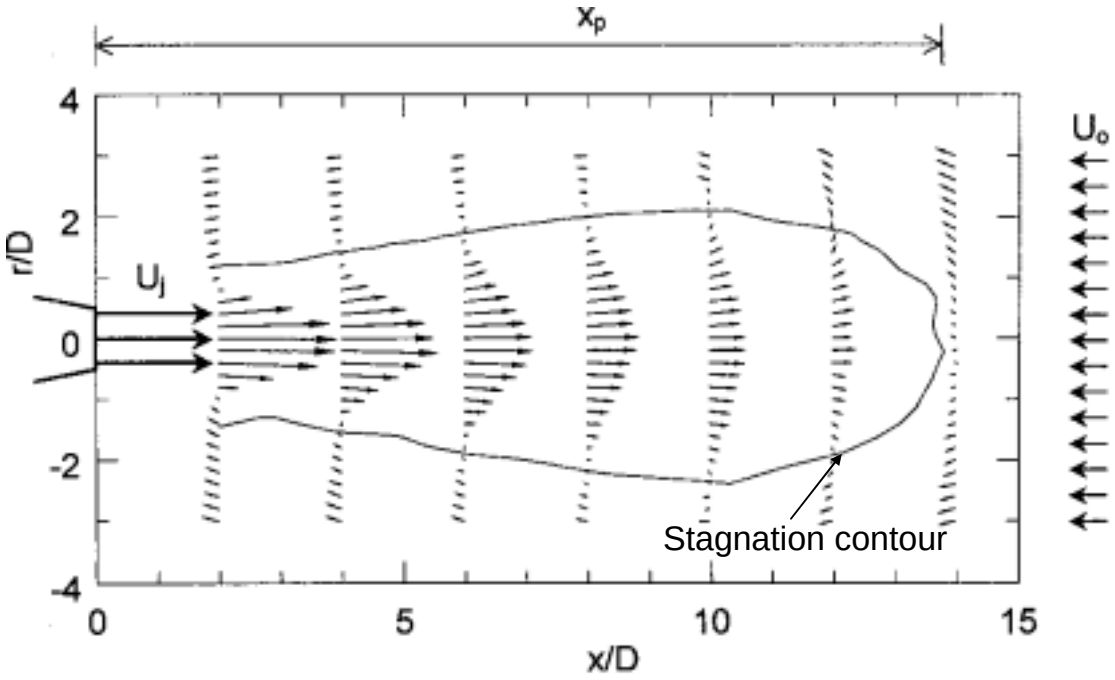

Figure 5. Mean velocity vectors and contour of zero mean axial velocity in a jet against a counterflow for U_j/U_o=5 [26].

The penetration length (x_P) is defined as a distance from the injector where the flow reaches zero velocity along the jet centerline (see Figure 5). Within the penetration length, the centerline velocity was found to decay more rapidly compared to a jet in a stagnant/quiescent ambient, and the centerline velocity data (for velocity ratios of 5 or more) were found to collapse onto a single-decay curve. A linear relationship between the penetration length and the jet-to-ambient current velocity ratio was derived from dimensional analysis and was supported by the experimental data,

$$\frac{x_P}{D} = 2.6\left(\frac{U_j}{U_o}\right)$$

where U_j is the initial jet axial velocity, U_o is the counter flowing velocity, and D is the jet exit diameter (see Figure 5).

According to Beltaos [27], the flow within a significant portion of the penetration distance retains many characteristics of a free jet, in terms of the velocity difference, $u + U_o$, where u is the axial velocity at a radial location r from the axis. However beyond x_P, the flow resembles the potential flow from a point source located at $x = 0.8\ x_P$. Additionally, the radial profiles of mean velocity also show a self-similar form and the corresponding half-width of the jet (b) can be expressed as:

$$\frac{b}{x_P} = \frac{0.2\left(\frac{x}{x_P}\right)}{\sqrt{\left(\frac{2.24\,x_P}{x}\right)^{\frac{2}{3}} - 1}}$$

Qualitative LIF measurements [28] showed large-scale meandering of jet penetration, which leads to significant temporal and spatial fluctuations in the location of the dividing interface between the incoming jet and the counterflow. Although, the concentration profiles follow similar trends as for mean velocities, the data could not be described with simple power-law decay.

2.5 Diagnostics Approaches

Since low emissions and the ability to produce a stable combustor for both non-premixed and premixed systems are dependent on local flow velocities and mixing, their measurement is essential to improving our understanding of flame stabilization and

mixing characteristics of the SPRF combustor. Various non-intrusive optical diagnostic techniques have been employed in past by various researchers in other combustion systems to explore these questions.

2.5.1 Particle Image Velocimetry (PIV)

Flow field (velocity) information in combustors can be obtained with various diagnostic methods, such as Laser Doppler Velocimetry (LDV) and Particle Image Velocimetry (PIV) [29]. As the latter is a two-dimensional imaging approach, it is advantageous when spatially correlated information is needed. With the incorporation of high resolution CCD imaging technology and the use of pulsed lasers for illumination, the PIV technique has been able to provide both temporally and spatially resolved velocity measurements, which are essential for exploring highly unsteady flows. For example, PIV has been successfully used to study various confined turbulent jet flame configurations [30]. Flow field measurements in various other combustor configurations have provided valuable information about flame stabilization and the fuel-air mixing characteristics [30].

2.5.2 OH PLIF and Chemiluminescence Imaging

Planar Laser Induced Fluorescence (PLIF) of the OH radical has been used to visualize thin cross sectional slices through the flame providing information about the combustion process [31]. An OH-PLIF image provides a cross sectional map of OH radicals in the combustor. Detectable levels of OH radicals are generally found in reaction zones (where OH can occur in super-equilibrium levels) and regions of mostly hot products (where equilibrium OH levels can be high) [32]. Thus these regions will

correspond to a high signal level (bright), whereas regions with cold reactants or cooled products will produce low signal levels (dark). Sharp gradients in PLIF intensity at the boundary of the dark region are due to production of OH at the flame front, providing data on the instantaneous flame front topology. CH-PLIF has also been used to mark the location of the flame front more accurately, as CH radicals are present only in the reaction zone and decay quite rapidly in the product gases. However, low concentration levels of CH in comparison to OH radicals especially in fuel lean environments result in reduced signal to noise ratios and CH PLIF imaging is usually limited to near stoichiometric equivalence ratios [33].

An even simpler imaging approach for studying combustion systems is chemiluminescence imaging [34]. Chemiluminescence is the radiative emission produced by species that are chemically formed in an excited energy state (typically an excited electronic level). After its chemical formation, the excited state molecule can transfer to a lower energy configuration through emission of a photon. Example sources of chemiluminescence in typical hydrocarbon flames are OH*, CH^* and CO_2^*. Chemiluminescence is generally considered to be good indicator of heat release rate in hydrocarbon flames [35].

2.5.3 Spontaneous Raman Scattering (SRS)

For quantitative measurements of major species, Spontaneous Raman Scattering (SRS) is often employed [36]. This is one of the few quantitative techniques that can provide spatially and temporally resolved, simultaneous multi-species concentrations of major combustion species (e.g., N_2, O_2, CO_2, H_2O and CH_4) and an estimate of the local temperature. By measuring mole fractions of all these major species in the combustion

zone, SRS can be used to quantify mixing of fuel with air and hot products. Because of the need to spectrally resolve the different wavelengths associated with each major species, these types of SRS data are typically acquired at a single point, or sometimes, along a line.

The Raman effect is an inelastic scattering process that occurs when light interacts with gas molecules. If the scattered photon gains energy from a medium, the scattering process is called anti-Stokes Raman scattering; conversely if it loses energy to the medium it is denoted Stokes Raman scattering. Stokes scattering is typically used for concentration measurements as it is stronger compared to anti-stokes scattering at the temperatures relevant to combustion processes [37]. However, the Raman scattered light signals are extremely weak. Cross-sections for SRS are about three orders of magnitude lower than elastic, Rayleigh scattering cross-sections for the same molecule (which in turn are three orders weaker than typical fluorescence cross-sections). Early studies of the Raman technique and its applications have mainly been restricted to measurements in simple flames of non-hydrocarbon fuels [38]. The range of applicability of the Raman technique has been extended to flames of hydrocarbon fuels with more complex flow geometries [39] in the past ten years. This has allowed the study of fuels of practical interest and for investigating complex turbulence-chemistry interactions in reacting flows, which is at the core of current combustion research.

In general, Raman scattering cross-sections, and thus the scattered-light energy, scales inversely with the fourth power of the excitation (laser) wavelength. Use of high-frequency UV laser radiation thus confers a large potential benefit in signal over use of visible radiation. Still, various laser sources in both UV and visible regions of the

spectrum have been employed in the past for single-shot Raman scattering measurements in flames.

Excimer lasers operating at 248 nm [40] (KrF) and 308 nm [41] (XeCl) have been used for Raman measurements in H_2 and methane flames. The excimer laser energies range from 200 to 250 mJ with a pulse length of about 30 nsec. Due to the high scattering cross-sections in the UV, 200mJ at 248 nm will scatter the same number of Raman photons as 2J at 532nm. However, the main disadvantage for the excimer lasers is the broadband interference generated from hydrocarbon fragments and fluorescence excitation of various species (OH, O_2 and H_2O) that interferes with the Raman signals. The interference problems, however, has been offset by using narrowband lasers or with the use of various filtering techniques based on polarization. The Raman scattered photons have the same polarization as the incident beam while the absorption and remission phenomenon like fluorescence and incandescence have photons emitted with all polarizations (unpolarized). This fact can be exploited to acquire nearly interference free Raman signals by recording the difference in spectra with polarization same as the incident beam and the polarization perpendicular to it. However, if the unpolarized interference signal is much larger than the polarized Raman signal, large errors result from attempting to determine the small the difference between the two polarizations. Also the spectral separation between the Raman lines of various species becomes smaller in the UV excitation region. This leads to small physical separation between the Raman peaks even when using a large spectrograph and hence requiring smaller detectors.

Flashlamp-pumped dye lasers in the visible range have also been successfully used for single shot measurements operating at 488 nm [42] and at 532 nm [43]. The

flashlamp-pumped dye laser produces high-pulse energies at reasonable repetition rates (more than one Joule per pulse at up to 10 Hz) and has a pulse duration of 3-5μs, which is long enough to avoid gas breakdown at the beam focus. The long pulse length, however, precludes the use of these lasers in high-speed flows. Another disadvantage of dye lasers is that the laser lineshape is less repeatable than for a solid-state or gas laser, and this can contribute to measurement uncertainties.

Solid state Nd:YAG lasers were not used typically in Raman applications due to the short pulse widths leading to gas break-down in the probe volume that restricts the amount of energy that can be supplied and hence lowers the Raman signals. This problem has been overcome, to a large extent, by optically stretching the laser pulse (with beam splitter and mirror arrangements) from 9 to about 40 ns [44]. This has allowed measurements with up to 1.6 J of energy per pulse at 532 nm to be used in a probe volume with a radius of about 800 μm. With pulse stretching, the high output energies of Nd:YAG lasers can allow for Raman imaging with thin laser sheets, and hence better spatial resolution without loss of Raman signal compared to UV lasers. Other approaches, such as multi-passing a single laser beam [45] through the probe volume or sequentially firing more than one YAG lasers [43], can also drastically increase the Raman signal output while maintaining low (less than breakdown) laser power. However, beam steering (for multi-passing) and cost (in the case of multiple lasers) can be problematic. Even with some loss in the number of scattered photons for visible compared to UV excitation, it can still be advantageous to employ visible laser sources, principally because of the availability of higher-efficiency optics and detectors for visible wavelengths.

The detector used for recording Raman spectra plays an important role in achieving good signal to noise ratios. A comparison of two detector options (an intensified CCD and an unintensified, back illuminated CCD) used for high-resolution imaging at visible wavelengths has been reported previously [46]. The SNR ratio that can be achieved from a detector can be represented as:

$$SNR = \frac{\eta N_{PP} Q}{\left(\eta N_{PP} \kappa Q^2 + N_x^2\right)^{\frac{1}{2}}}$$

$$\text{and} \qquad N_x^2 = N_{bin}\left(N_{spurious}^2 + N_{dark}^2\right) + N_{read}^2$$

where η is the quantum efficiency of the front-end detector (the photocathode in the intensified case and the CCD in the unintensified version), N_{pp} is the number of signal photons, Q *is* the electron gain between the photocathode and the CCD array, and k is the intensifier noise factor. N_x accounts for various noise terms due to dark charge and spurious charge generation on the chip along with the chip readout noise. Binning multiple CCD pixels together tends to reduce the contribution due to the dark and spurious charges and improves the SNR.

Intensified detectors have the advantage of fast gating capability, allowing the Raman signal, which occurs only during the laser pulse, to be differentiated from long duration background light. This is especially important in combustion systems where flame luminosity and wall radiation can be significant. Intensified detectors also have the advantage of internal gain due to which noise sources associated with the CCD detector and electronics are generally unimportant as compared with photoelectron shot noise. The best quantum efficiencies of conventional (Gen II) intensifier photocathodes in the visible wavelengths (570–670 nm) are relatively low and with additional noise factor of the

intensifier, the resulting signal-to-noise ratio (SNR) can be poor. On the other hand back-illuminated detectors have very high quantum efficiencies (85%), but noise sources associated with the charge readout, the thermally generated dark charge, and spurious charge generation can be important due to the lack of an internal gain mechanism. Moreover due to the limitation of mechanical shutters, fast gating of unintensified detectors becomes difficult. Typically, the SNR for intensified detectors is higher compared to back-illuminated unintensified system for very low light levels of the order of a hundreds of photoelectrons. However, with recent improvements in quantum efficiencies of photocathodes for Gen III intensifiers in the visible, the opportunity exists for higher SNR over a wider range of light levels in comparison to an unintensified detector.

CHAPTER 3

EXPERIMENTAL SETUP AND INSTRUMENTATION

This chapter describes the various experimental facilities, instrumentation and the data analysis techniques that were employed in this study. The first section describes the design of the Stagnation Point Reverse flow combustor, the injector configuration used and the range of operating and geometric parameters explored. The second section provides an overview of the instrumentation used for the various diagnostic techniques used in this study. Finally, the last section briefly explains the methods used for analyzing the measurements to obtain physical parameters like velocities, mole fractions and flame/heat release locations, which can be used to understand the physics behind the combustor operation.

3.1 SPRF Combustor Description

The SPRF combustor used for the current study is a laboratory scale, atmospheric pressure device. A schematic of the combustor facility is shown in Figure 6a. The combustor consists of a dual concentric tube injector centrally located in a quartz tube. A base plate, also made from quartz, forms the closed end of the tube and allows introduction of laser light for PIV, OH PLIF and Raman measurements. Quartz has been used for the combustor walls and the base plate as it can sustain high temperatures while allowing optical access for the diagnostic techniques mentioned above. The laser sheet enters the combustor through a diametric plane on the base plate and emitted light is collected perpendicular to the laser illuminated plane.

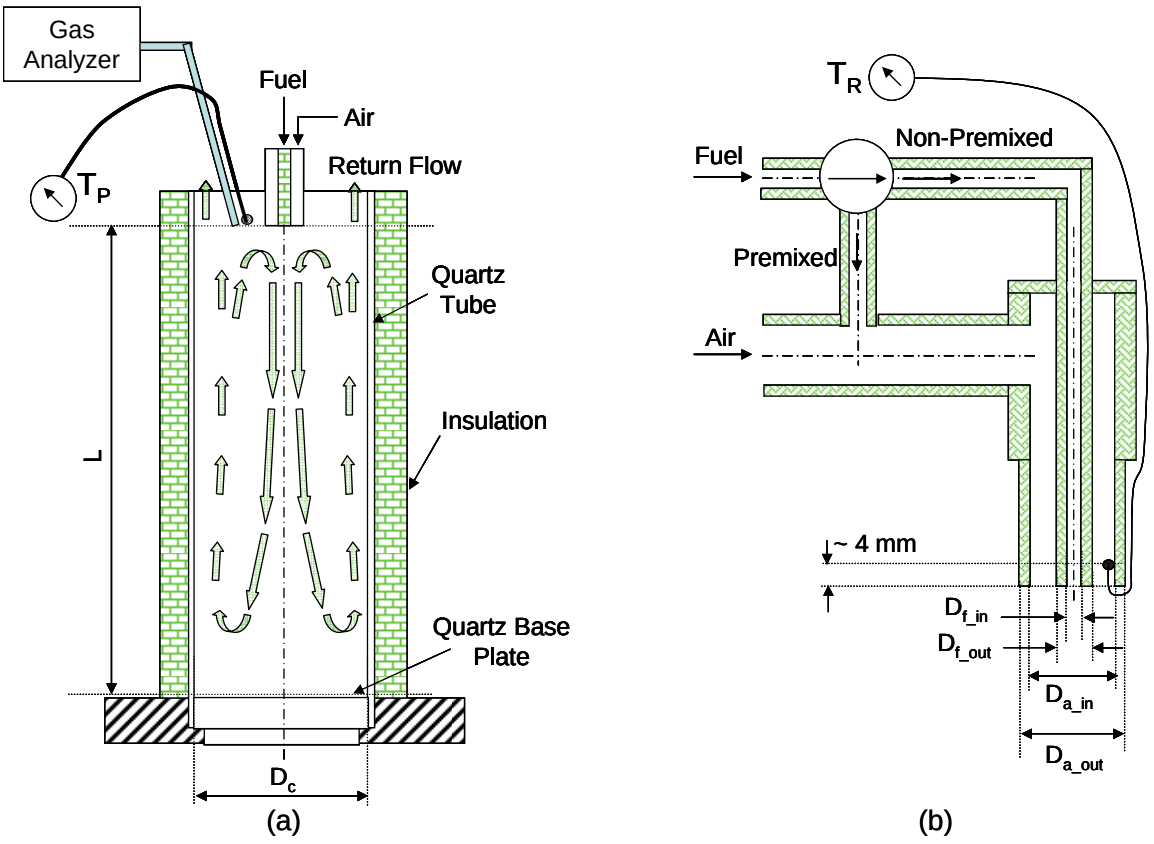

Figure 6. Layout of SPRF combustor and coaxial injector used for this work.

As shown in Figure 6b, the injector in this SPRF combustor operating on natural gas consists of a co-annular tube configuration (without swirl). In the premixed mode of operation, both fuel (natural gas) and air are injected through the outer annulus while the inner tube is closed off upstream. In the nonpremixed case, fuel comes in through the inner tube with a co-flow of air injected through the outer annulus; so no mixing can occur until the flows enter the combustor. This injection configuration allows for easy switching of the combustor between premixed and nonpremixed modes with a valve controlling the flow direction of the fuel stream as shown in Figure 6b. The fuel (natural gas) and air are supplied from the building facilities. Flow rates into the combustor are monitored independently and controlled with calibrated rotameters to produce a range of

equivalence ratios and non-preheated injection velocities ranging from 10 to 130 m/s. The calibration curves for the flowmeters used are presented in Appendix A. Both the streams are choked upstream of the premixing section to ensure a constant injection mass flow rate and equivalence ratio.

Table 1. Dimensions of the baseline SPRF combustor used.

Dimension	Size (mm)
Combustor diameter (D_c)	70
Combustor length (L)	279.4
Air tube outer diameter (D_{a_out})	17
Air tube inner diameter (D_{a_in})	12.6
Fuel tube outer diameter (D_{f_out})	6.25
Fuel tube inner diameter (D_{f_in})	4.7

The reference configuration, which is found to produce ultra-low emissions, consists of a combustor with 70 mm inner diameter and a length of 279.4 mm. The corresponding injector used for this case has an air tube diameter of 12.6 mm and a fuel tube 4.7 mm in diameter. Most of the measurements were performed for the baseline configuration and the geometry is summarized in Table 1. However, to understand the effect of geometry scaling on combustor performance, measurements were also acquired over a range of geometries where the combustor diameter, length and injector dimensions were modified (see Figure 6). The combustor diameter was modified by replacing the quartz tube with a tube of appropriate diameter. To concisely describe the various configurations, each is designated with a "D (D_c)/A (D_{a_in})/F (D_{f_in})" format. For

example, the reference configuration with a 70 mm combustor inner diameter and injector with 12.6 and 4.7 mm inner tube diameters for air and fuel respectively is designated D 70/A 12.6/F 4.7. The summary of all the geometry changes with respect to the reference configuration can be seen in Table 2. Additionally for each of the configurations shown in the table, the combustor length variation is also studied by moving the injector in or out of the quartz tube. The lengths used in this work are 279.4 (full length combustor), 254, 203.2 and 152.4 mm.

Table 2. Summary of the various configurations used to undestand the geometry scaling characteristics of SPRF combustor.

Configuration	D_c (mm)	D_{a_in} (mm)	D_{a_out} (mm)	D_{f_in} (mm)	D_{f_out} (mm)
D 70/A 12.6/F 4.7	70	12.6	17	4.7	6.25
D 70/A 21/F 4.7	70	21	26.8	4.7	6.25
D 70/A 21/F 10.4	70	21	26.8	10.4	13
D 90/A 21/F 10.4	90	21	26.8	10.4	13
D 90/A 26.7/F 16	90	26.7	33.5	16.8	19.1

To reduce heat losses, the combustor can be insulated with four close fitting hollow cylinders of alumina (ZIRCAR AL-30AAH), surrounding the whole quartz tube. To facilitate optical access, a 150° window is cut out of one of the sections, which can be placed at different axial locations. Thus the optical measurements are acquired for one-quarter of the combustor at a time wherever mentioned, and the complete field is derived by splicing them together.

3.2 Instrumentation

3.2.1 Global Measurements

The exhaust gases from the SPRF combustor are sampled with an uncooled ceramic probe, and the gas composition is determined with a PG-250 (Horiba CEMS) portable gas analyzer. The PG-250 system relies on electrochemical sensors for measuring composition of five different species (NO_x, SO_2, CO, CO_2 and O_2). NO_x concentration is estimated by measuring chemiluminescence intensity from NO_2^* that is formed when the oxides of nitrogen are exposed to ozone. Oxygen is measured by a galvanic cell (Pb and KOH). An infrared absorption technique is used to measure CO_2, CO and SO_2 concentration. For this study, only NO_x, CO and O_2 were recorded.

The Horiba system is frequently calibrated against a standard set of gases at different concentrations and the system is able to provide repeatable readings within 0.5% of full scale, and the zero drift is within 1% of full scale per day. The full scale settings used are listed in Table 3.

Table 3.Full scale values used on the Horiba system for measurement of emissions from the combustor.

Species measured	Full scale value used	Notes
NO_x	25 ppmv	for readings < 25 ppmv
	50 ppmv	for readings > 25 ppmv
CO	200 ppmv	For readings < 200 ppmv
	500 ppmv	For readings > 200 ppmv
O_2	25 % by volume	

The product gases exiting the SPRF combustor flow over the injector, increasing the temperature of the incoming reactants. The temperature of the reactants and the exhaust gases are monitored with a shielded K-type thermocouple, 1/16" (1.58 mm) in diameter. This particular thermocouple system is capable of measuring temperatures up to 1300 K. The thermocouple for measuring reactant temperature is placed in the injector annulus, roughly 4 mm upstream of the injector plane as shown in Figure 6b. The exhaust gas thermocouple and emissions sampling probe are placed together approximately 25 mm into the combustor. This positions them axially in the injector exit plane and radially about midway between the combustor and injector walls. These probes are not present, however, while the optical measurements are recorded.

3.2.2 Spontaneous Raman Scattering (SRS)

Instantaneous mole fractions of all the major species at a given point in the SPRF combustor are measured with Spontaneous Raman Scattering (SRS). As shown in the schematic for Raman measurements (Figure 7), the second harmonic output (532 nm) of a *Q*-switched Nd:YAG laser (Quanta-Ray Pro-250, Spectra Physics) is used. The pulse energy is restricted to 250 mJ (measured with an Ophir L30A-EX) at a 10 Hz repetition rate to prevent laser-induced spark/plasma formation at the probe volume, which can occur due to breakdown of the gas under the intense electric field generated by tightly focusing a Q-switched laser, and to avoid damage to the combustor quartz walls. The laser beam is focused into a flattened 2 mm × 300 μm probe volume with a combination of a spherical (50 mm diameter, 1 m focal length) and cylindrical (25×50 mm^2 with 1 m focal length) lens. This probe volume was chosen to maintain the laser fluence under the breakdown threshold and still provide good spectral resolution, by aligning the 300 μm

projection with the spectrometer slit width. The laser beam enters the combustor through the transparent quartz base plate at the bottom of the combustor, similar to the PLIF setup, but in this case is not spread out into a sheet.

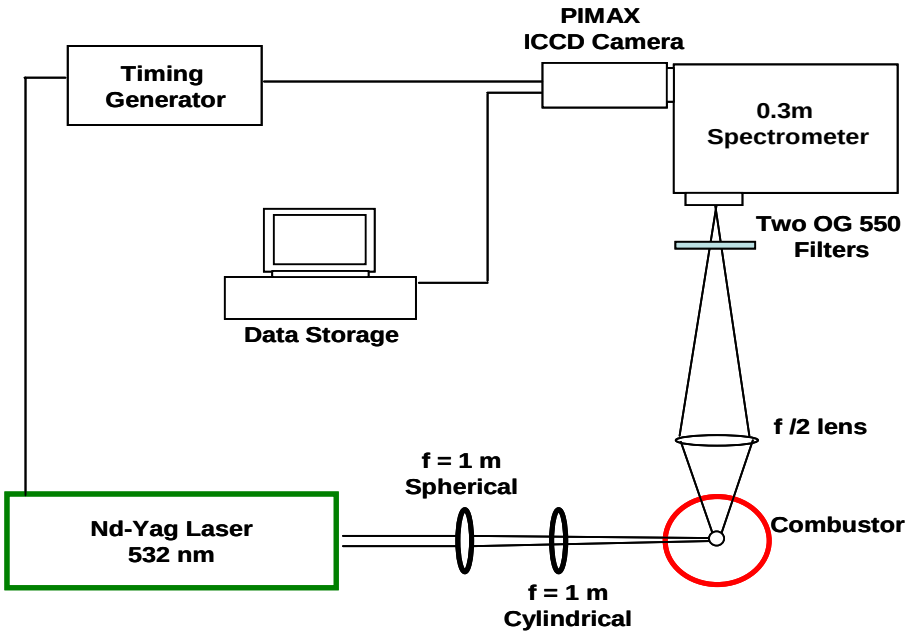

Figure 7. Optical layout of Spontaneous Raman Scattering (SRS) setup.

The Raman scattering signal is collected at a right angle relative to the beam propagation direction using an 80 mm diameter and 160 mm focal length spherical lens. The collected light is focused onto the 300 µm slit of a 0.3 m spectrometer (*f*/4, SpectraPro-300i, Acton Research Corporation) at *f*/5.3 and a magnification of 0.5. Two OG 550 Schott glass filters are used to attenuate Rayleigh and Mie scattered light (from dust particles) entering the spectrometer. The incident light is dispersed with a 300 grooves/mm grating, and then recorded on a PI Acton ICCD camera (512×512 pixels). The ICCD camera is equipped with an 18 mm Gen III (HB filmless) intensifier tube. This arrangement allowed us to capture a spectral range of 555-685 nm with a

resolution of 0.256 nm/pixel. The Gen III intensifier tube has a quantum efficiency of ~30% (see Figure 8) for the wavelength of interest as compared to the ~5% efficiency of the Gen II intensifiers used by most previous researchers for SRS measurements. The higher sensitivity of this ICCD helped us offset some of the signal-to-noise ratio deficit created by the use of a lower laser power then normally used (but which requires a complicated pulse-stretching arrangement [44]). The intensifier is gated for a 30 ns window synchronized with the laser pulse. This short gate timing helps reject background emissions from the flame and blackbody radiation from the combustor walls. The collected spectra are binned on-chip over 170 pixels in the spatial direction to increase the signal-to-noise ratio of the measurements, resulting in a spatial resolution of 2 mm along the laser beam. The combustor and injector assembly are mounted on a traversing platform, while the optics setup remained fixed. This configuration allowed us to make instantaneous single point Raman measurements from the injector plane to 200 mm into the combustor along the centerline axially or to 30 mm from the centerline radially. With this arrangement molefractions could be measured to an accuracy of about 6% at low temperatures (450 K) and to about 12% at flame temperatures (1700 K). Additional details about the uncertainties in the Raman system are provided in Appendix B. Raman systems with better accuracies (3%) have been developed by other researcher [36] for analyzing concentration profiles with large gradients (like within a flame front), but with the use of elaborate pulse stretching systems and about ten times higher laser power.

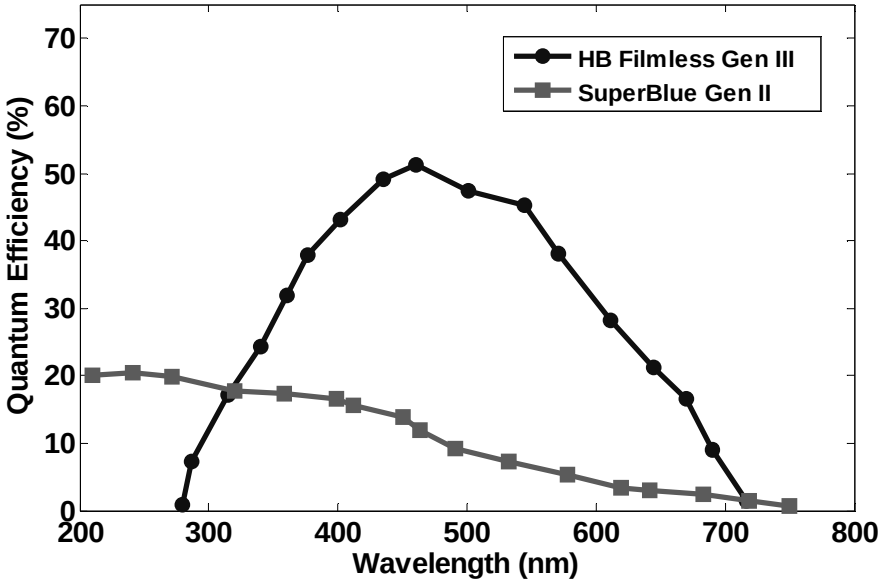

Figure 8. Quantum efficiency variation of the Gen III filmless intensifier used for this work in comparison to the Gen II (Super blue) inetsifier used by previous researchers.

3.2.3 Particle Image Velocimetry (PIV)

Instantaneous two-dimensional realizations of axial and radial velocity were obtained using Particle Image Velocimetry (PIV). The components of the PIV system are illustrated in Figure 9. For these measurements, both the combustion air and fuel are separately seeded with 1-2 μm aluminum oxide particles. The alumina particles have the advantage of a high melting point (2300 K) allowing for velocity measurements in the flame zone. The light source is a dual-cavity, frequency doubled pulsed Nd:YAG laser (Surelite I-10 PIV). The infrared emission (1064 nm) from both cavities is combined before entering a frequency-doubling crystal producing collinear beams of the same polarization. Each pulse has a maximum energy of 90 mJ (at 532 nm) and duration of ~9 ns. The output from the laser is directed into the combustor section with high power 532 nm laser mirrors (CVI Laser) and formed into a sheet using a 50 mm focal length,

25.4 mm diameter, plano-convex cylindrical glass lens followed by a 500 mm focal length, 90 mm diameter, plano-convex cylindrical lens. The coplanar vertically-expanding laser sheets (approximately 400 μm thick) illuminate particles seeded along the injector center-plane from the closed end of the combustor (Figure 9).

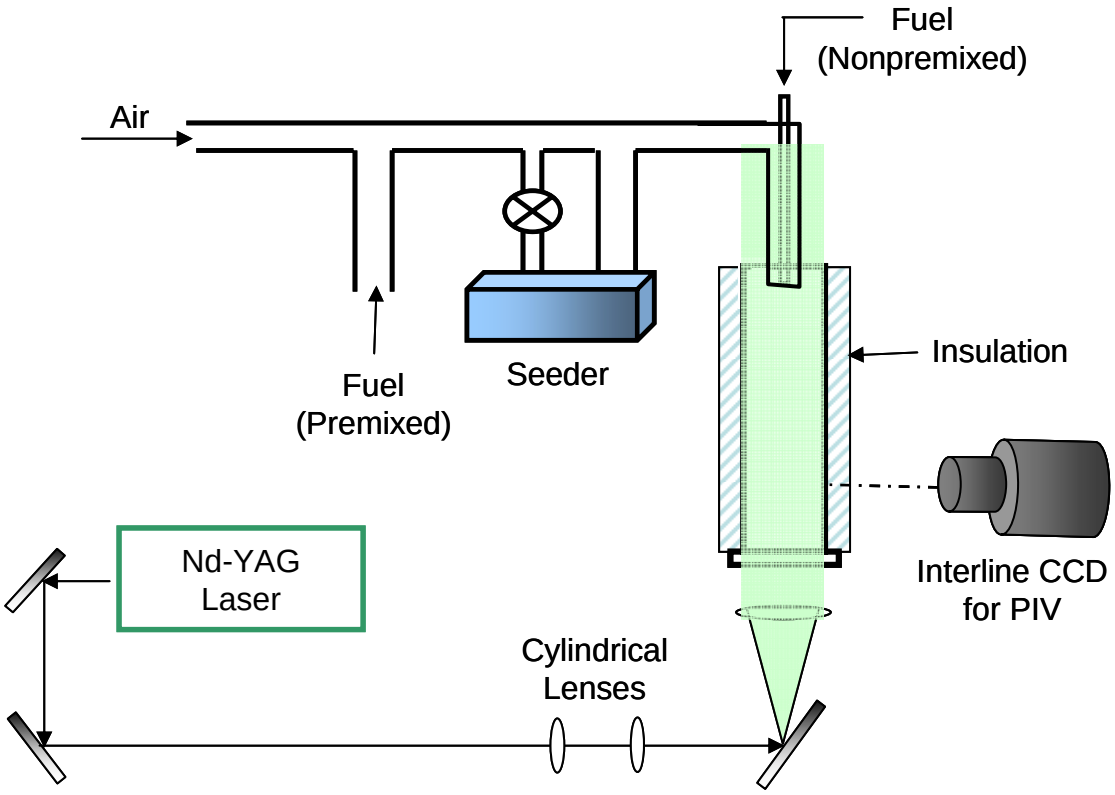

Figure 9. Experimental layout of the Particle Image Velocimetry (PIV) setup.

Scattering from the particles is collected at right angles onto an interline CCD camera (MicroMax) fitted with a 50 mm *f*/1.8 Nikon lens. The camera has a high resolution array with 1300×1030 pixels, where each pixel is a 6.7 μm square, and a 12-bit signal resolution. The timing of the two laser heads and the camera shutter are synchronized with a delay generator (Stanford Research Systems DG-535). Pulse delays between the image pairs vary from 3 to 11 μs for different regions of the combustor

based on the optical magnification and the gas velocities in the field of view. The images are acquired for 55×89 mm segments of the combustor and then spliced together to produce the complete averaged combustor velocity field.

3.2.4 Planar Laser Induced Fluorescence of OH

The OH PLIF system, as shown in the optical layout of Figure 10, consists of a Lambda Physik dye laser system pumped by the second harmonic of a Nd:YAG laser (the same one used in the SRS setup). The output from this dye laser system (around 570 nm) is frequency-doubled with a tunable second harmonic generator (Inrad Autotracker, BBO crystal). The portion of light whose frequency is successfully doubled is separated from the rest of the light with a set of three dichroic turning mirrors that selectively reflect wavelengths from 280-300 nm. The resulting ultraviolet (UV) laser beam is then expanded into a sheet that is 65 mm wide and 300 μm thick with three fused silica lenses. The UV laser sheet enters the combustor through a diametric plane on the quartz disk at the bottom and illuminates the complete length, and nearly the complete width of the combustor.

The wavelength of the frequency doubled dye laser system is calibrated by measuring an OH excitation scan in a reference laminar flame and comparing it to a theoretically predicted OH spectrum for the $A^2\Sigma^+(v'=1)\leftarrow X^2\Pi(v''=0)$ band. The excitation scans of OH were obtained in a laminar premixed CH_4-air flame by recording the emitted fluorescence light with the help of a photomultiplier tube (Hamamatsu R928B). The measured spectra, seen in Figure 11, match the theoretical spectrum obtained using the LIFBASE software. These spectra are used to tune the frequency doubled dye laser wavelength to the $Q_1(6)$ line of the (1,0) band at 282.93 nm for fluorescence imaging in

the SPRF combustor. This line was chosen so that the measured OH PLIF signal is relatively independent of the local temperature. A temperature change from 1500 to 2000 K results in a change in PLIF signal by only about 15%. The average energy of the laser pulses (~10 ns long) entering the combustor was measured to be 12 mJ, and the maximum shot-to-shot variation in pulse energy during the experiments was less than 10%.

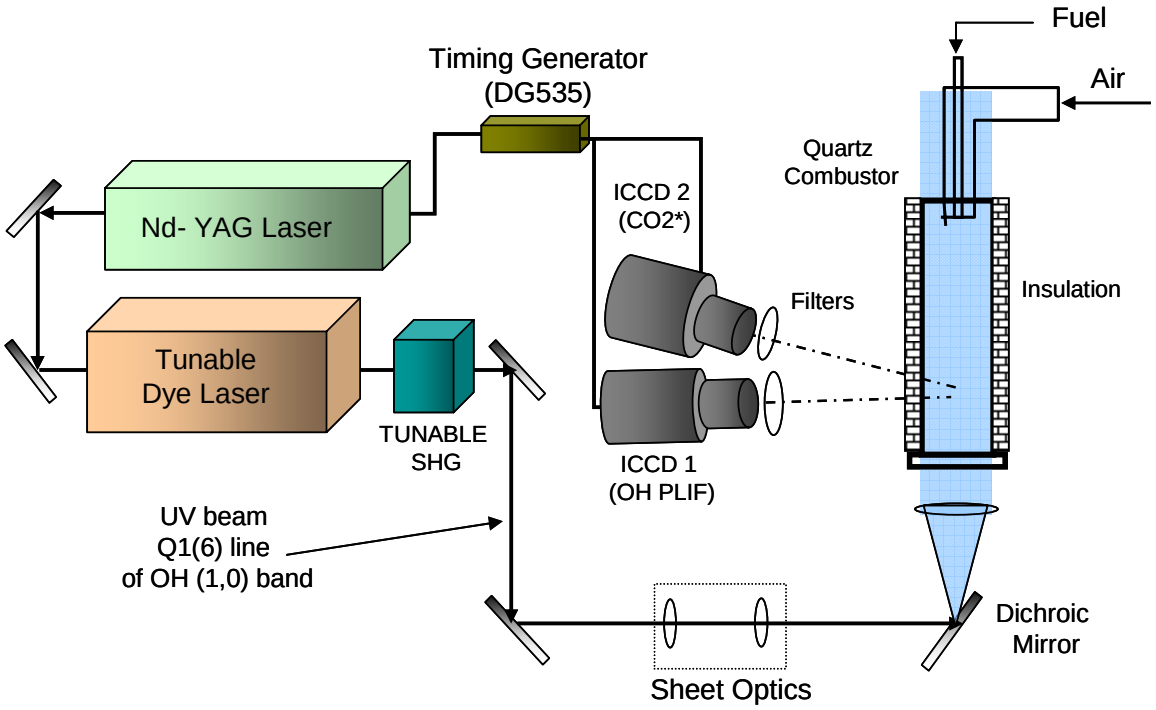

Figure 10. Layout of the OH PLIF and chemiluminescence setup.

The emitted fluorescence light is detected at right angles to the incident laser sheet with a 25 mm intensified PI-MAX camera (256×1024 pixels) equipped with a UV-Nikkor lens system (105 mm, *f*/4). The detected fluorescence signal is limited to 300–370 nm by WG305 and UG 11Schott glass filters placed in front of the camera lens. The

camera's field of view includes the whole width of the combustor in all the images, which results in a pixel resolution of approximately 300 μm.

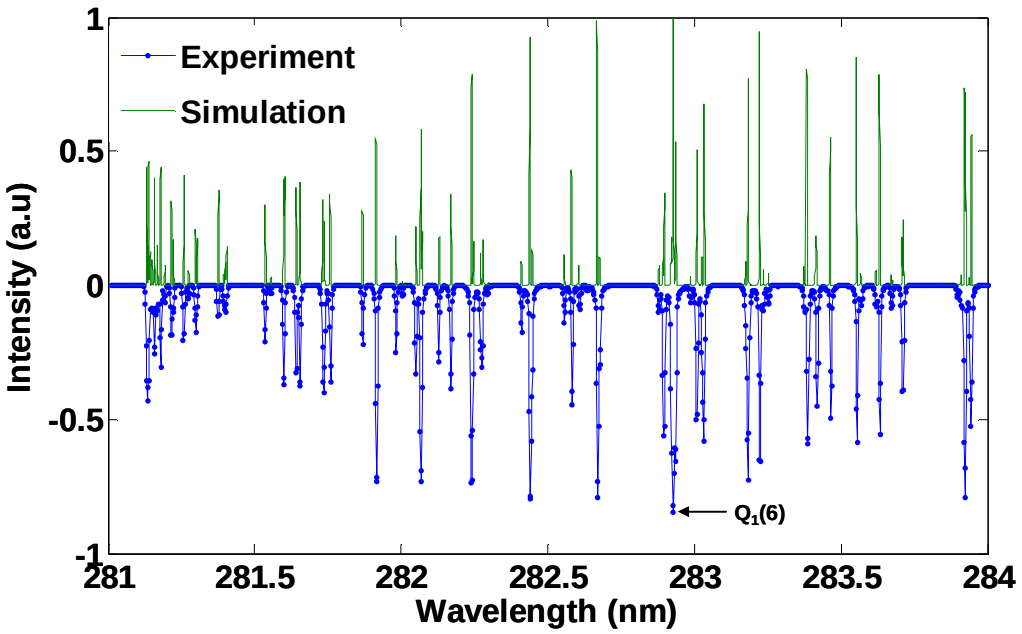

Figure 11. OH excitation scan obtained by scanning the dye laser output in comparison to a simulation of OH spectrum from the LIFBASE software.

3.2.5 Chemiluminescence Imaging

The flame chemiluminescence naturally emitted by chemically produced CH^* and CO_2^* molecules in the flame zone is also imaged at right angles to the laser sheet. The light is collected with a separate intensified camera (Princeton Instruments ICCD-576-S/RB-E with 18 mm intensifier and 384×576 pixels) equipped with a narrow band interference filter that passes CH emission (430±5 nm), along with a fraction of the broadband CO_2^* signal in that wavelength range. The camera is synchronized such that the exposure (250 μs long) begins 100 ns after the OH laser pulse. This allows for complete decay of the OH fluorescence before the chemiluminescence image is recorded.

Thus both cameras record nearly simultaneous features of the combustor. The field of view for this camera is also set to see the whole width of the combustor with a pixel resolution of 250 μm. Images of a reference grid are recorded with both cameras, and these are used to spatially match the corresponding PLIF and chemiluminescence frames.

3.3 Data Analysis and Interpretation

3.3.1 Spontaneous Raman Scattering

A typical SRS spectrum recorded in the flame zone of the SPRF combustor operating at an equivalence ratio of 0.6 is shown in Figure 12. The labeled peaks correspond to each of the major species CO_2, O_2, N_2, CH_4 and H_2O present in the combustor. A list of Raman cross-sections of various species and the corresponding line positions for a pump wavelength (λ) of 532 nm is shown in Table 4. The signal under each of these peaks is a quantitative indication of the amount of the corresponding species in the measurement volume. However, before these can be determined, the background offset due to the instrumentation needs to be removed from the signal. For this purpose a reference background spectrum was obtained when the spectrometer slit was blocked and this was subtracted off from each of the subsequently measured spectra.

The integrated area under the peaks in the Raman signal corresponds to the concentration of the species in the measurement volume. While it is relatively straight forward to establish limits for integrating the signal under the stand-alone peaks, if two or more peaks are in close proximity in the spectrum a more nuanced approach is required. In particular, such interference can be observed in the CO_2 and O_2 peaks, which are located close to each other, such that their signals partially overlap. Further, although not

apparent in the Figure 12, there is secondary Raman peak of CH_4 under the CO_2 and O_2 peaks as represented in the sketch in Figure 13a. This interference from the CH_4 signal also needs to be addressed for obtaining the interference-corrected signals of CO_2 and O_2.

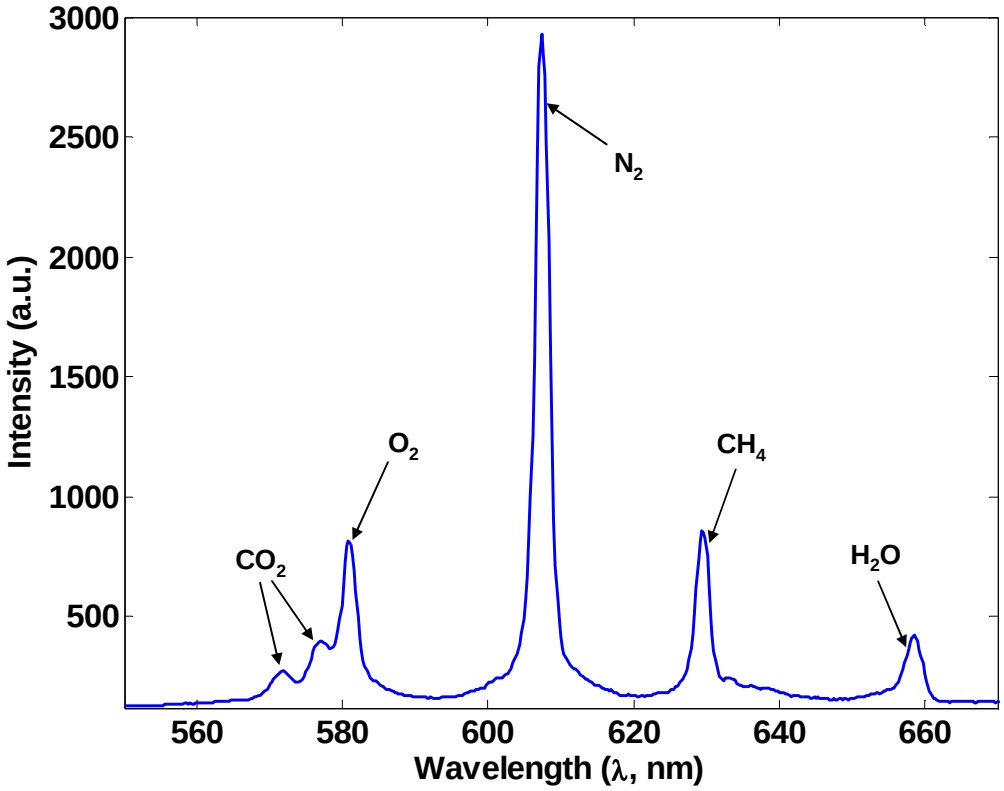

Figure 12. Mean Raman spectra over 500 instantaneous frames recorded close to the flame zone in the SPRF combustor at ϕ=0.58.

Table 4. List of the relative Raman crosssections of various species normalized to that of nitrogen. Also listed is the line positions of the scattered light for a pump wavelength of 532 nm.

Molecule / Formula	Raman Scattering Cross-Section (normalized to N_2)	Line Position (nm) (λ_{Pump} = 532 nm)
Hydrogen, H_2	3.86	682.98
Water, H_2O	3.51	660.28
Ethylene (ν_1), C_2H_4	6.4	633.83
Methane (ν_3), CH_4	5.7	633.71
Methane (ν_1), CH_4	8.55	629.6
Nitrogen, N_2	1	607.31
Carbon monoxide, CO	0.93	600.46
Acetylene, C_2H_2	6.2	594.39
Ethylene (ν_2), C_2H_4	2.12	582.28
Water, H_2O	0.008	581.33
Oxygen, O_2	1.04	579.98
Carbon Dioxide (ν_1), CO_2	1.13	574.42
Ethylene, C_2H_4	2.8	572.9
Carbon Dioxide ($2\nu_2$), CO_2	0.75	571.04
Ethane, C_2H_6	1.72	561.67

3.3.1.1 Interference Correction

The first step in correcting for this interference between the CO_2 (571.04 and 574.42 nm) and O_2 peaks (579.98 nm) is to determine the point that can be used as a delineator or the limit of integration between the signals of CO_2 and O_2. To determine

this point, we use an average spectrum of 500 instances collected in the product gases of the combustor. At this location, the concentration of CO_2 and O_2 is relatively constant with almost no CH_4. For the purpose of interference correction, it is assumed that the interference-free (or pure O_2) signal is roughly symmetric about its peak. Therefore, the pure O_2 spectrum is obtained simply by reflecting the right half of the observed O_2 peak. Then by subtracting this pure O_2 spectrum from the measured signal gives us the interference-corrected or the pure CO_2 spectrum as well. Plotting these two pure spectra together readily yields the intersection point, as shown in the sketch in Figure 13a.

The intersection point represents the integration limit between the CO_2 and the O_2 peaks. The area under the peak to the left of this intersection point is treated as the measured CO_2 signal (S_{CO_2}), while the area to the right of this intersection point is treated as the measured O_2 signal (S_{O_2}). The corresponding signals obtained after correction are denoted as $\hat{S}_{CO_2}$ and $\hat{S}_{O_2}$. Additionally we have overlap signals labeled in $\hat{S}_{X,Y}$ format, which represent the contribution of the species *X* to the signal of peak *Y*. For example, the contribution of O_2 to CO_2 ($\hat{S}_{O_2,CO_2}$) is shown in Figure 13b. These signals are then used to find the ratio of the pure O_2 signal within the integration limits of the CO_2 signal to the corrected O_2 signal (α) along with an analogous ratio for CO_2 (β). These can be expressed in a mathematical form as follows:

$$\alpha = \frac{\hat{S}_{O_2,CO_2}}{\hat{S}_{O_2}} \qquad \text{and} \qquad \beta = \frac{\hat{S}_{CO_2,O_2}}{\hat{S}_{CO_2}}$$

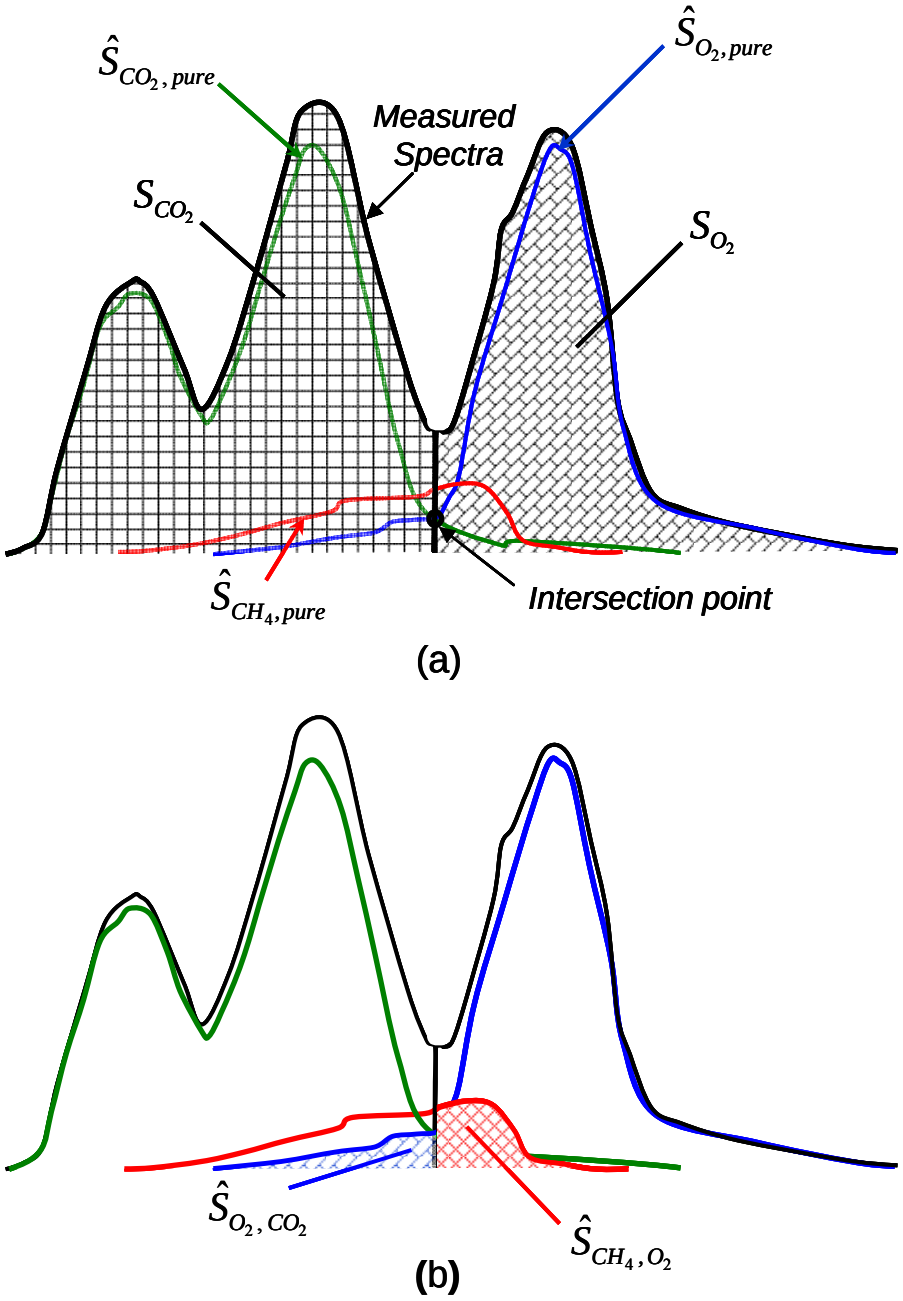

Figure 13. Sketch of the CO_2 and O_2 region of the Raman spectrum illustrating overlaps and terminology of various signals used.

Furthermore, the presence of the secondary CH_4 peak also causes the integrated signals of CO_2 and O_2 to be artificially increased (Figure 13b). In order to quantify this effect, a reference Raman spectrum is obtained in a stream of pure CH_4. Such a spectrum

shows the primary CH_4 peak at 629.6 nm as well as the secondary peak in question. The ratio of the part of the secondary peak within the limits of CO_2 signal to the primary CH_4 peak (γ) and the corresponding ratio for the O_2 signal (δ) are found using this data.

$$\gamma = \frac{\hat{S}_{CH_4,CO_2}}{\hat{S}_{CH_4}} \qquad \text{and} \qquad \delta = \frac{\hat{S}_{CH_4,O_2}}{\hat{S}_{CH_4}}$$

With the four constants (α, β, γ and δ), the measured signals S_i (integrated area under the curve within the integration limits of each species) can be corrected for interference to obtain the interference corrected signals $\hat{S}_i$ by multiplying with an interference correction matrix Q.

$$\begin{bmatrix} \hat{S}_{CO_2} \\ \hat{S}_{O_2} \\ \hat{S}_{N_2} \\ \hat{S}_{CH_4} \\ \hat{S}_{H_2O} \end{bmatrix} = [Q] \begin{bmatrix} S_{CO_2} \\ S_{O_2} \\ S_{N_2} \\ S_{CH_4} \\ S_{H_2O} \end{bmatrix}$$

Where,

$$Q = \begin{bmatrix} \frac{1-\alpha}{1-(\alpha+\beta)} & \frac{-\alpha}{1-(\alpha+\beta)} & 0 & -\left(\frac{(1-\alpha)\gamma}{1-(\alpha+\beta)} + \frac{-\alpha\delta}{1-(\alpha+\beta)}\right) & 0 \\ \frac{-\beta}{1-(\alpha+\beta)} & \frac{1-\beta}{1-(\alpha+\beta)} & 0 & -\left(\frac{-\beta\gamma}{1-(\alpha+\beta)} + \frac{(1-\beta)\delta}{1-(\alpha+\beta)}\right) & 0 \\ 0 & 0 & 1 & 0 & 0 \\ 0 & 0 & 0 & 1 & 0 \\ 0 & 0 & 0 & 0 & 1 \end{bmatrix}$$

For the instrumentation used in this current work the interference correction matrix that was used is shown below.

$$Q = \begin{bmatrix} 1.08 & -0.25 & 0 & -0.01 & 0 \\ -0.08 & 1.25 & 0 & -0.06 & 0 \\ 0 & 0 & 1 & 0 & 0 \\ 0 & 0 & 0 & 1 & 0 \\ 0 & 0 & 0 & 0 & 1 \end{bmatrix}$$

Signal interpretation can also be complicated by fluorescence interactions from PAH (Polycyclic Aromatic Hydrocarbons) and soot produced in flame zones. These interactions are expected to be negligible in the current work due to lean operation of the combustor and hence have been neglected.

3.3.1.2 Calibration

The SRS signal ($\hat{S}_i$) of the species *i* is proportional to the concentration of the species present in the probe volume, which can be expressed in terms of the species mole fraction (X_i) and the local temperature (T).

$$\hat{S}_i = \frac{C_i X_i}{T}$$

The constant of proportionality (C_i) has to be found for each of the major species (CO_2, O_2, N_2, CH_4, H_2O) to make quantitative concentration measurements. This is done by calibrating the Raman signals in a set of standard gas mixtures through a preheated laminar jet (300 – 800 K) issuing at a known temperature. Air has been used for calibration constants of N_2 and O_2, while pure CH_4 and CO_2 gases are used for their calibration constants. Due to the difficulty of producing a known concentration stream of water, its signal was calibrated with measurements at the exit of the SPRF combustor (at ϕ=0.58), where the equilibrium water concentration is known to be twice the CO_2 concentration. The calibration constants so measured are found to not vary significantly

(< 10% variation) for a temperature change from 300 to 750 K as shown in **Error! Reference source not found.**. Therefore, mean calibration constant values (independent of the temperature) are used for estimating the mole fractions.

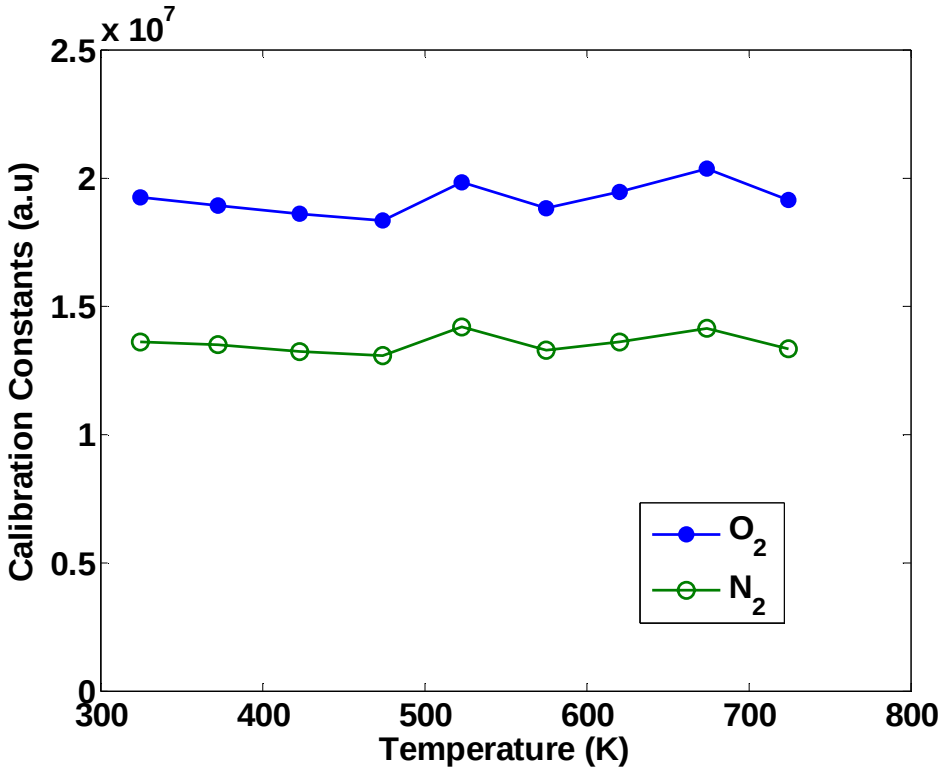

Figure 14. Variation of calibration constants of O_2 and N_2 with gas temperature measured in laminar preheated air jet.

3.3.1.3 Matrix Formulation

Once the measured Raman signals are corrected for interferences and calibration constants are determined, we are left with six unknowns (X_{CO_2}, X_{O_2}, X_{N_2}, X_{CH_4}, X_{H_2O} and T) and five equations, one for each species. Thus to close this system we make another assumption that CO_2, O_2, N_2, CH_4 and H_2O are the only major species present in the measurement volume. This can be written as:

$$\sum X_i = 1$$

The error in major species concentrations calculated as above, neglecting CO and other minor species, is estimated from equilibrium calculations and found to be within 2% of the actual value. For the ease of data processing the above equation system has been formulated in a matrix form

$$\begin{bmatrix} C_{CO_2} & 0 & 0 & 0 & 0 & -\hat{S}_{CO_2} \\ 0 & C_{O_2} & 0 & 0 & 0 & -\hat{S}_{O_2} \\ 0 & 0 & C_{N_2} & 0 & 0 & -\hat{S}_{N_2} \\ 0 & 0 & 0 & C_{CH_4} & 0 & -\hat{S}_{CH_4} \\ 0 & 0 & 0 & 0 & C_{H_2O} & -\hat{S}_{H_2O} \\ 1 & 1 & 1 & 1 & 1 & 0 \end{bmatrix} \begin{bmatrix} X_{CO_2} \\ X_{O_2} \\ X_{N_2} \\ X_{CH_4} \\ X_{H_2O} \\ T \end{bmatrix} = \begin{bmatrix} 0 \\ 0 \\ 0 \\ 0 \\ 0 \\ 1 \end{bmatrix}$$

By inverting this matrix, all the species concentrations are obtained.

3.3.2 Particle Image Velocimetry

The velocity field is calculated from the frames obtained by imaging the seeding particles with the help of the Insight 6 software from TSI. The cross-correlation to find the average particle displacement is evaluated using a FFT based algorithm. The recorded image pairs are divided into 64×64 pixel interrogation windows with a 50% overlap. This configuration yields a total of 1209 vectors over each quarter of the combustor. The particle displacements are obtained to an accuracy of 0.1 pixels using a sub-pixel interpolation algorithm. Based on the sheet thickness used and the interrogation window size, each velocity vector represents an average over a 2.19×2.19×0.4 mm.

The velocity was measured only in a plane so the total velocity statistics were estimated by assuming the out of plane velocity component (u_z) was comparable to the in-plane lateral component (u_y). Hence, the total rms velocity (u'_{rms}) in terms of the rms

velocities along the axial and the in-plane lateral components at a point can be expressed as follows.

$$u'_{rms} = \sqrt{\frac{u'^{2}_{x} + 2\,u'^{2}_{y}}{3}}$$

The integral length scale (L_T) is obtained from the instantaneous velocity field by evaluating the spatial correlation coefficient (R_L) as a function of a correlation length r. The integral of this coefficient over all length scales is a measure of the local integral length scale,

$$L_T = \int_0^{\infty} R_L(r)\, dr$$

where,

$$R_L(r) = \frac{\overline{[U(x) - \overline{U(x)}]\ [U(x+r) - \overline{U(x+r)}]}}{u'_{rms}(x)\ \ u'_{rms}(x+r)}\ .$$

3.3.3 OH PLIF and Chemiluminescence Imaging

The acquired OH PLIF and chemiluminescence images were first cropped to view only the combustor region. The combustor outline is located using a reference image obtained with same camera configuration but without any filters. All images are subsequently cropped to this region of interest. Figure 15a shows one such image and the combustor location is marked in yellow on the frame. The subsequent processing of the recorded images is illustrated in Figure 15b-d. The first frame (Figure 15b) shows a raw OH PLIF image acquired in the combustor. The dark noise from this image is then eliminated by subtracting out the corresponding dark image and a 3×3 pixel smoothing

filter is then used to reduce image noise (Figure 15c,d). A similar approach is taken to process the chemiluminescence images.

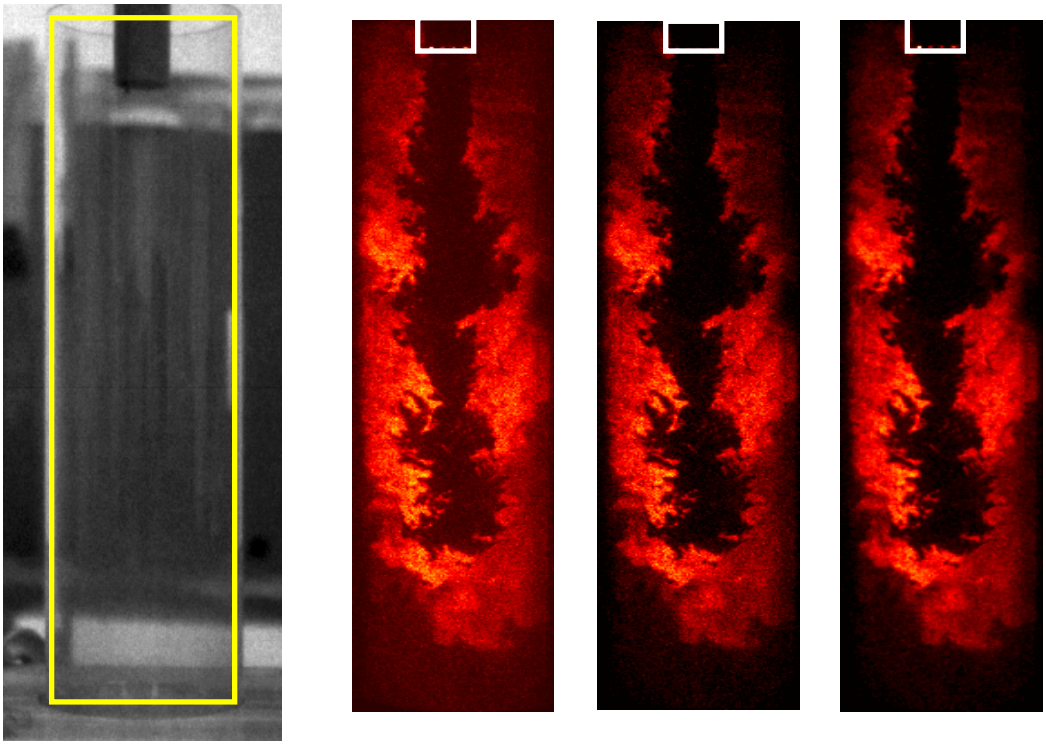

Figure 15. (a) Reference image showing extent of the SPRF combustor. (b) Raw OH PLIF, (c) background subtracted and, (d) final smoothed image recorded in the combustor.

As the OH radical is a combustion intermediate as well as a combustion product, reaction zones and regions of mostly hot products will show up as bright (high PLIF signal) regions, whereas regions with cold reactants will show up as dark regions in the PLIF images shown above. So the extent of the dark region starting at the injector reflects how far reactants penetrate into the combustor. Sharp gradients in intensity at the boundary of this dark region are due to production of OH at the flame front.

These OH PLIF images were analyzed by tracking the high gradient contours that mark the flame edge due to production of OH at the flame front. Raw PLIF images are first smoothed with a median filter to suppress noise and then intensity gradients are calculated at each point. Only gradients over a certain threshold are accepted and a contour of such high gradients is taken as the flame location. The location of the flame estimated from this method is in good agreement with the raw PLIF images obtained in the 2nd quarter of the combustor (x=70-150 mm) as shown in Figure 16.

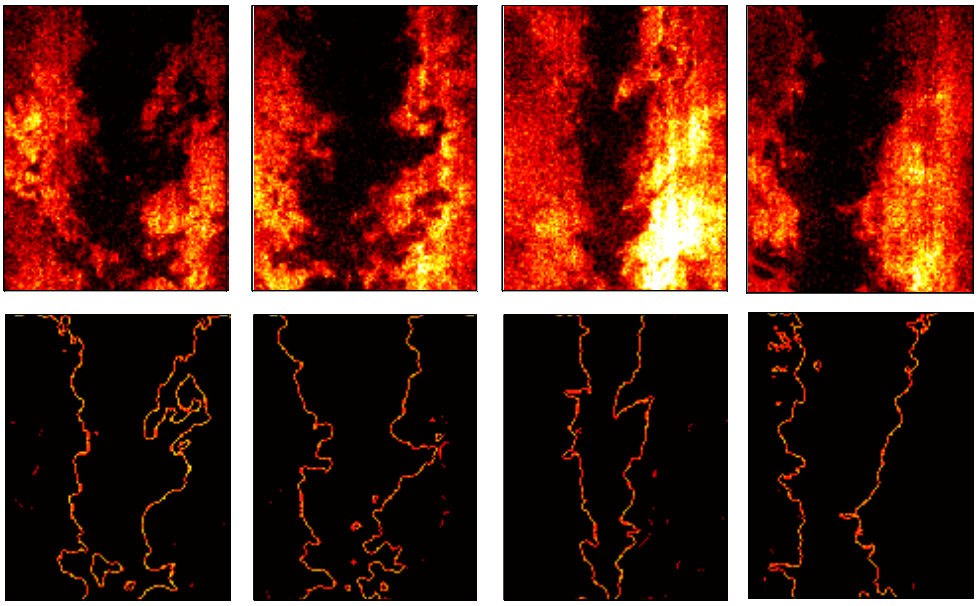

Figure 16. Sample single shot OH PLIF images from the 2nd quarter of the combustor (x=70-150 mm) along with the corresponding tracked flame edge.

CHAPTER 4

FLAME STABILIZATION IN SPRF COMBUSTOR

This chapter describes the results of an investigation to determine the reasons for the ability of the SPRF combustor to burn fuel stably very close to its lean flammability limit. For this purpose we begin be examining the velocity field in the combustor (Section 4.1) in order to identify features that would influence flame stability. The various flame stabilization mechanisms exhibited in the combustor are explored in Section 4.2 over a range of combustor mass loadings, both at fuel lean and stoichiometric conditions. Also the level of product entrainment that is characteristic of this unique geometry is quantified and its effects on various combustion characteristics, such as the ignition time scales and flame structure, are explored in Sections 4.3-4.5.

4.1 Premixed Combustor Flow Field

The time-averaged flow field in the combustor is shown in Figure 17a as a combination of axial velocity contours and interpolated streamlines. These results were obtained by averaging 300 instantaneous PIV images for a total mass flow rate of 8.1 g/s and at an equivalence ratio of 0.58, where the SPRF combustor was found to produce NO_x emissions of around 1 ppm (corrected to 15% O_2). The reactant temperature in the injector, after heating by the exiting products, was nearly 450 K. Thus the velocity right at the injector exit, based on the measured flow rate and inlet temperature, should be 130 m/s. The PIV velocity data starts from an axial location (x) of 22 mm (x/D_{a_in}=1.8) from the injector exit plane. The average velocity measured at this location was 120 m/s closely matching the air injection velocity estimate.

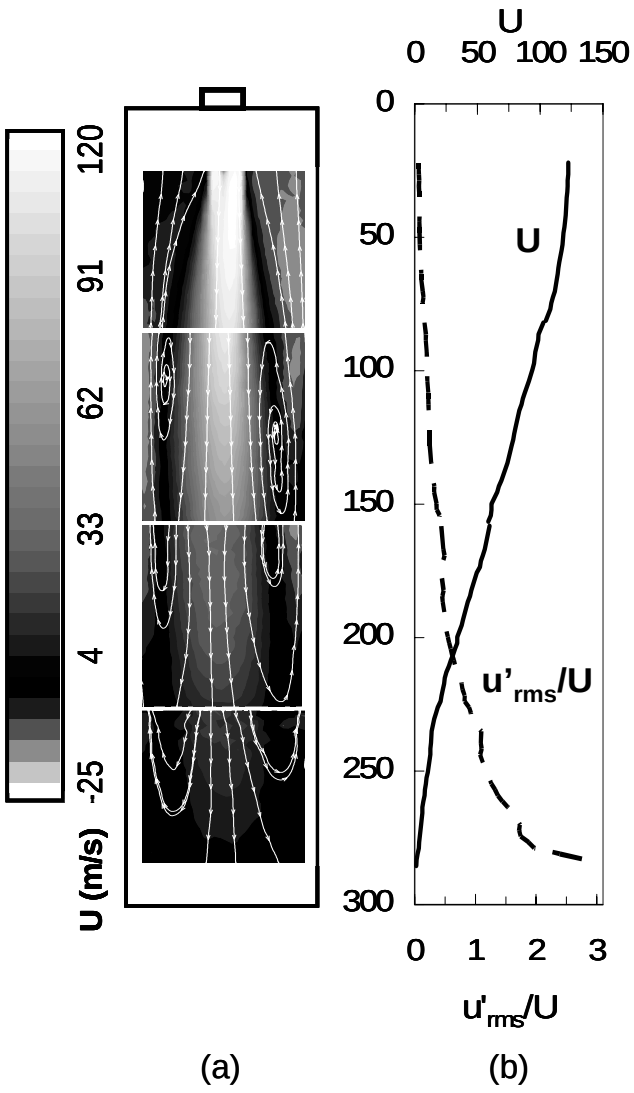

Figure 17. (a) Mean axial velocity contours, (b) mean centerline velocity and turbulence velocity profiles in the premixed SPRF combustor at ϕ=0.58 and a loading of 8.1 g/s.

In some ways the flow field resembles that of a confined jet, but the presence of the closed end causes the axial velocity to decay rapidly. As seen in Figure 17b, the average axial velocity (U) drops to half its initial value by x=150 mm (x/D_{a_in}=12). At the same time, the rms fluctuations (u'_{rms}) and turbulence intensity rapidly increase, with the centerline u'_{rms}/U increasing from 0.23 to 0.5 over a small distance (x/D_{a_in}=10-12.5).

Thus the geometry of the SPRF combustor ensures the existence of a region of both "low" average velocity (though still tens of m/s) and high fluctuating velocity, which should exists over a wide range of combustor loadings.

The rapid decay in velocity results from the high shear between the incoming forward flow and the reverse flow of the exiting gases. On average, the incoming "jet" spreads rapidly, as evidenced by the highly diverging streamlines near the open end of the combustor. Essentially, the reverse flow increases the width of the shear layer compared to a simple confined jet. This can also lead to entrainment of exiting high temperature products and flame radicals into the incoming reactants, which can significantly enhance chemical reaction rates [13]. The temperature increase due to mixing with hot product gases along with the presence of radicals tends to increase the mixture reactivity, while the dilution of this reactant mixture with inert product gases tends to reduce it. As shown later, the net effect is an increase in reactivity with increasing product recirculation at the levels found in the SPRF combustor.

4.2 Stabilization Mechanisms

The influence of the flow field features on flame stabilization mechanisms was investigated by imaging the OH field in the SPRF combustor over a range of combustor loadings. These images were acquired at stoichiometric conditions so that we can explore all the possible stabilization mechanisms in the combustor, some of which are not evident in fuel lean conditions. In these instantaneous images (Figure 18), the reaction zone is usually indicated by the sharp gradients in the OH PLIF signal adjacent to the reactant gases. For the lowest loading (0.14 g/s), the velocities in the combustor are laminar, and the combustor flow is essentially an annular, Bunsen-like jet flame. Since the inner tube

of the annular injector is closed-off upstream in premixed operation, the flame can stabilize on both the outer rim of the injector and the inner, bluff body-like recirculation zone. For this low velocity condition, the flame sits just above the injector, and what is primarily seen in Figure 18a is the decrease in OH concentration as the products cool (since OH equilibrium concentrations are extremely temperature sensitive). For increasing injection velocity (Figure 18b,c), the increased strain causes the flame to progressively lift at the outer rim, while it remains anchored on the inner tube. For these low velocity conditions, the shear between the inflow and exhaust is low. In addition, the lack of OH PLIF signal in the exhaust gases indicates the combustion products are relatively cool, likely due to heat losses to the combustor walls.

Only at higher loadings (beyond ~1.8 g/s) does the entrainment of high temperature products appear to return the flame closer to the highly strained outer lip region (as indicated by the OH signal in the reverse flow of Figure 18d,e). At 1.8 g/s, there is still a small flame in the inner recirculation zone, but it does not stabilize the rest of the combustor. Beyond this loading, the inner region disappears and the flame appears stabilized on the outer shear layer (Figure 18e).

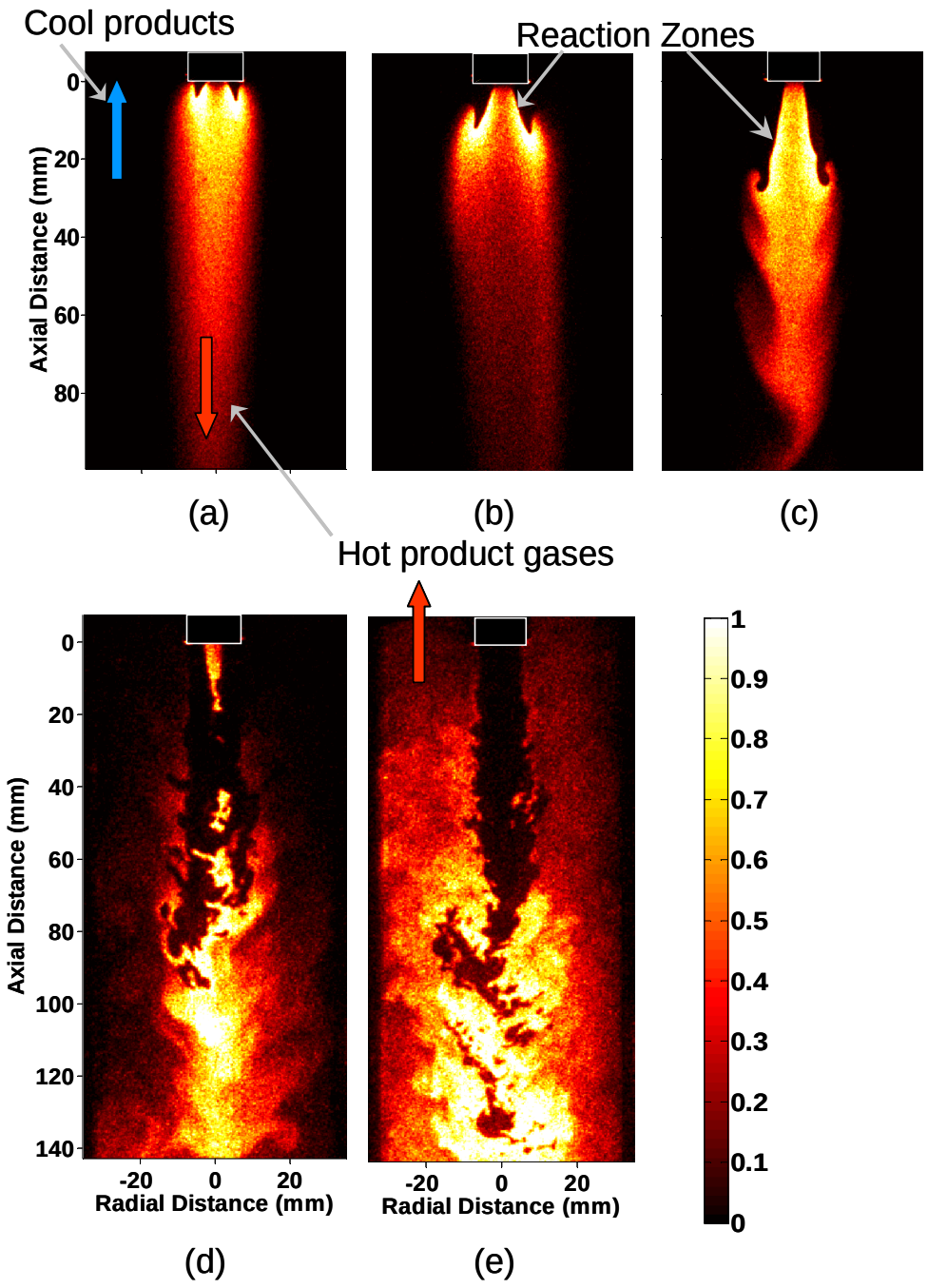

Figure 18. Single shot PLIF images showing near injector region in the combustor at ϕ=1 and loadings of (a) 0.14 (b) 0.2 (c) 0.43 (d) 1.8 and (e) 5.7 g/s.

The high OH concentrations at the bottom of the combustor (x=120-230 mm) suggests that the temperatures there are high or that much of the heat release occurs in

this region. This roughly coincides with the low average velocity region observed in the velocity data for the insulated combustor operating lean and at high loadings. This suggests another possible stabilization mechanism. High turbulence intensity in this part of the combustor creates a highly distorted flame front (seen in Figure 18e) that can propagate against a relatively low mean flow (which is still 20-50 m/s). Like the stabilization process near the outer rim of the injector discussed earlier, any entrainment of hot products into the reactants before reaching the low velocity region will also tend to increase the flame speed and lowering ignition energies as suggested by Kalb and Sattelmayer [13] and contribute to the stability of the combustor.

These observations are verified with OH PLIF and chemiluminescence fields measured in the insulated, premixed SPRF combustor under the same lean (ϕ=0.58) flow conditions as the PIV data. Figure 19a,b shows simultaneously acquired instantaneous PLIF and chemiluminescence images. Image pairs acquired at different times from different "window" regions are stacked in the figure to reveal overall combustor features. The bottom portion of the combustor (x=230-303 mm) lacks interesting features, hence large images sets were not acquired in this region, which is represented by a blank frame in Figure 19. Although the averaged velocity fields indicate a clean symmetric flow, the instantaneous flame images look drastically different. The region closest to the injector shows significant OH signal present in the product stream heading upward and the corresponding chemiluminescence image indicates the presence of a weak flame extending close to the injector. The dark region starting at the injector in the OH PLIF images reveals how far unburned reactants penetrate into the combustor, while sharp gradients in intensity at the boundary of this dark region are due to production of OH at

the flame front. These regions of reactants seen in the OH PLIF image appear to fit just inside of the simultaneously measured chemiluminescence emission (Figure 19a,b), which is an indication of where heat release is occurring. This suggests a distinct flame-like structure, i.e., the reactants are probably not burning in a widely distributed reaction zone.

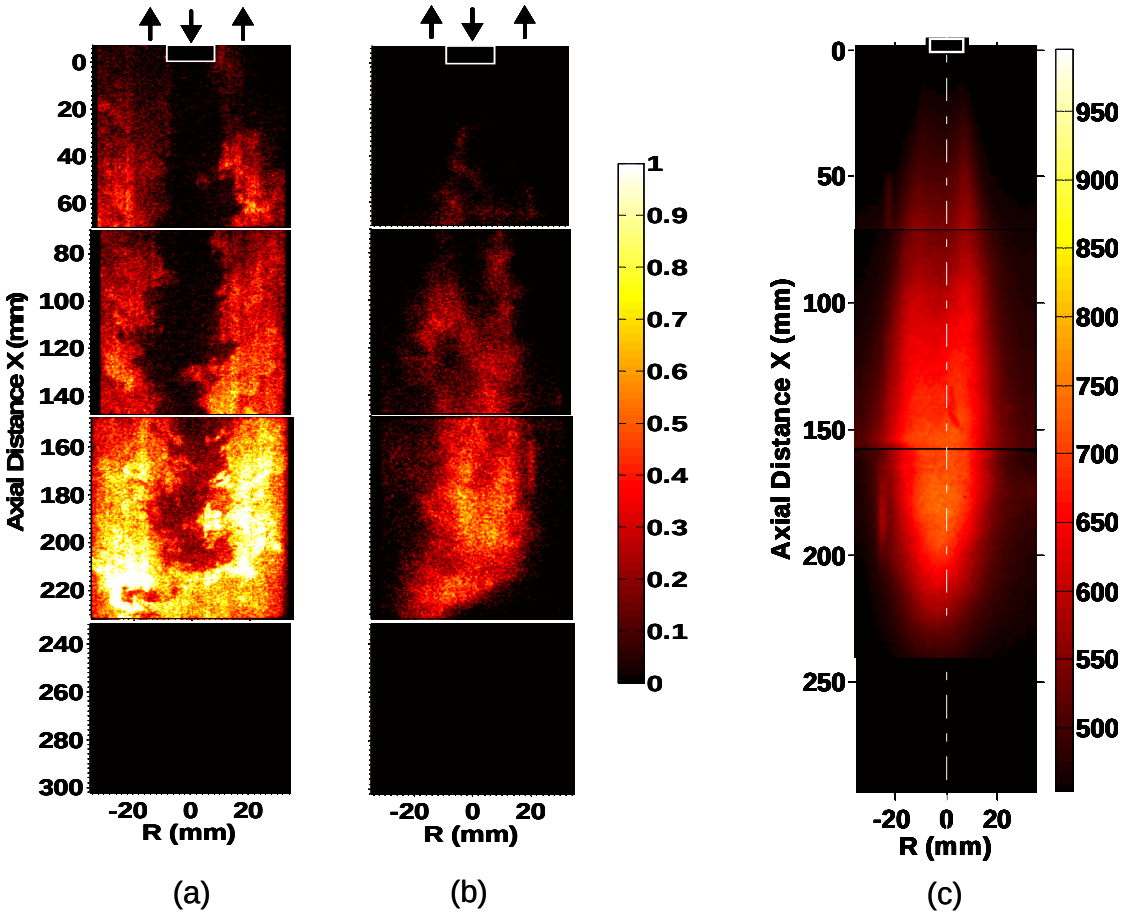

Figure 19. (a) Instantaneous OH PLIF frames acquired with simultaneous (b) chemiluminescence signal at ϕ=0.58 and loading of 8.1 g/s in the premixed insulated combustor. (Different windows not acquired simultaneously) (c) Average chemiluminescence field at the same conditions.

The mean chemiluminescence field (Figure 19c), obtained by averaging 100 instantaneous images, again shows the presence of a weak flame extending close to the injector. Most of the heat release in the combustor occurs downstream of the cold reactant core, as opposed to the upstream edges of the jet, and the main heat release zone coincides with the low U, high u'_{rms} region, as mentioned earlier.

The penetration of reactants into the primary stabilization region near the middle of the combustor is further investigated for varying injection velocities at a lean equivalence ratio, ϕ=0.65 (see Figure 20). The combustor configuration is similar to the one used in the previous set of experiments, however the camera's field of view has been adjusted to image the full length of the combustor to capture the instantaneous whole field features (the also necessitated removing the insulation to gain complete optical access to the combustor). The instantaneous OH PLIF shots shown in the figure correspond to flames operating stably at *Re* from 10^4 to 5.7×10^4, where conventional jet flames would have already blown off. The reactant jet, represented by the dark regions extending from the injector in these images, is found to penetrate somewhat deeper into the combustor with increasing injection velocity (Figure 20a-e). The stagnation condition imposed by the end wall, however, makes the jet penetration much less sensitive to loading at high loading conditions (e.g., Figure 20c-e) than conventional jet flames, where flame length would continue to increase with injected velocity.

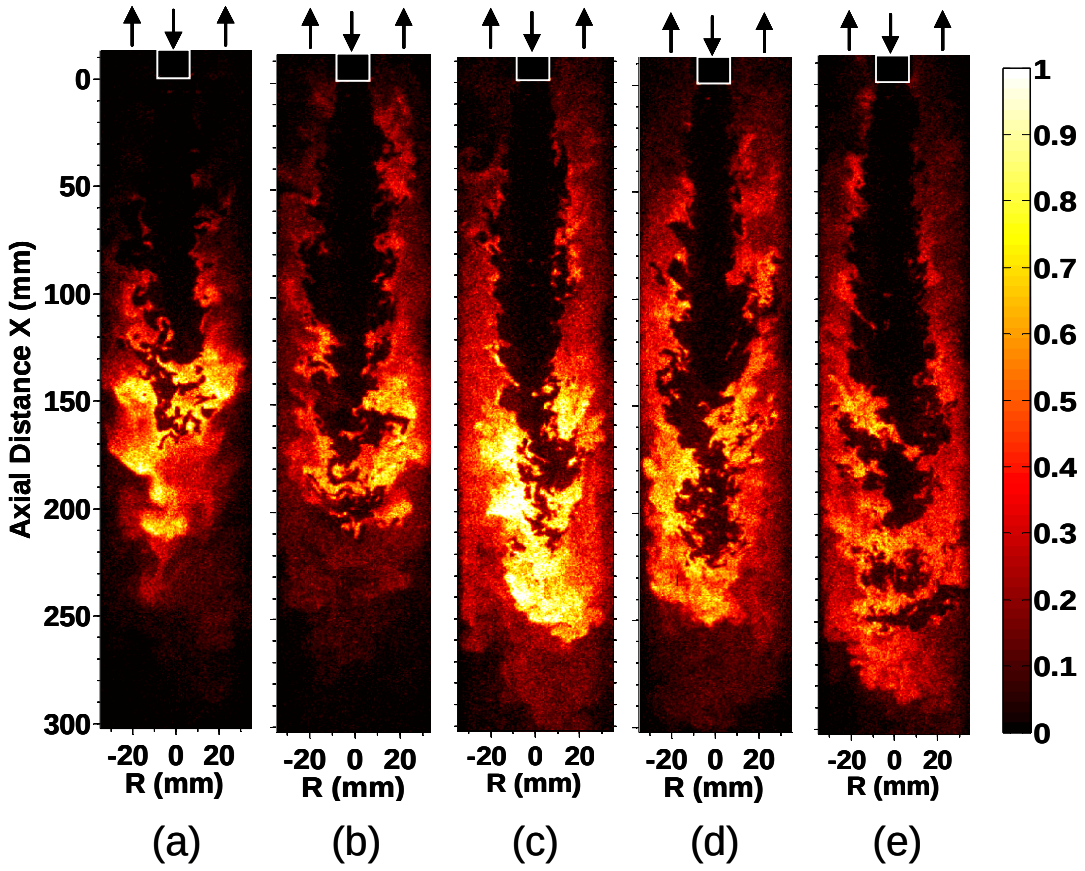

Figure 20. Instantaneous PLIF images covering the whole combustor at ϕ=0.65 at loadings of (a) 2 (b) 4.5 (c) 7.2 (d) 9.4 and (e) 10.7 g/s. Reynolds number based on injector diameter (Re_j) is estimated to vary from 10,000 to 57,000 for lowest to the highest loading case.

The trend of reactant penetration observed in the instantaneous flame images can also be seen statistically from the two-dimensional histograms representing the combustor "flame brush" (regions in the combustor where the flame zone is most likely located). Histogram images based on more than 300 images of instantaneous flame location shown in Figure 21 indicate that the jet penetration does not change significantly (only ~15% increase) even when the combustor loading is doubled. This is an indication that the flame structure remains the same when loading is increased (at nominally high

loadings). Also, based on the combustor geometry, we can postulate that the increasing loading does not affect the flow field features significantly. The independence of the NO_x emissions with variation in loading illustrated in chapter 1 may be explained based on these arguments. Starting approximately 150 mm downstream of the injector (where the increase in turbulence intensity was also seen in Figure 17), gradients in OH PLIF signal intensity are less steep due to entrainment of hot products into the reactant stream.

This interesting low velocity region in the bottom half of the combustor, with a highly convoluted flame front, is further explored by examining the set of correlated OH and chemiluminescence frames shown in Figure 22 acquired at the same flow conditions as the Figure 17 results. The chemiluminescence in these images again occurs around the dark reactant regions in the PLIF image. At these high loadings, the reactant jet is found to become more unsteady. This unsteadiness in the flame zone can be clearly seen from the large scale movement of the heat release zone, again suggesting the presence of large vortical structures in this region. The chemiluminescence signal is spatially integrated normal to the laser sheet and hence also captures out of plane heat release. This likely accounts for the small regions of heat release seen in a few of the chemiluminescence frames without a corresponding reactant region in the PLIF images (marked with ellipses in Figure 22).

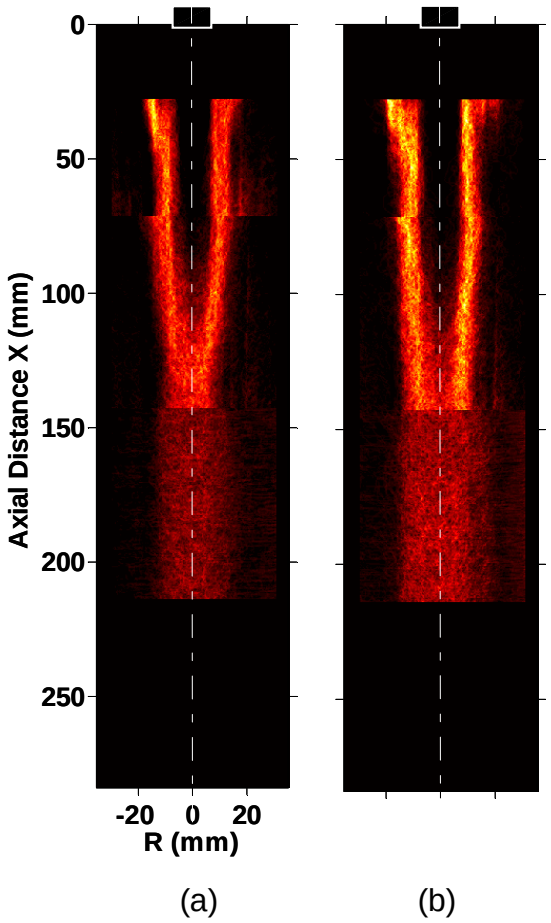

Figure 21. Histogram of flame location for constant ϕ of 0.58 at (a) nominal loading of 8.14 g/s and a (b) high loading of 13.13 g/s.

The unsteady flame motion in the combustor is quantified with the tracked flame edge statistics and velocity statistics. A plot of probability (C_x) of finding a flame at a position along the combustor axis is obtained by normalizing the histogram counts with the maximum value along the centerline shown in Figure 23. A reaction zone is almost never found along the centerline before 80 mm (x/D_{a_in}=6.4), where u′/U = 0.14. Most of the time, the reaction zone appears beyond 120 mm (x/D_{a_in}>9.6, u′/U>0.23). Again, this shows the flame resides in a region of relatively high velocity fluctuations.

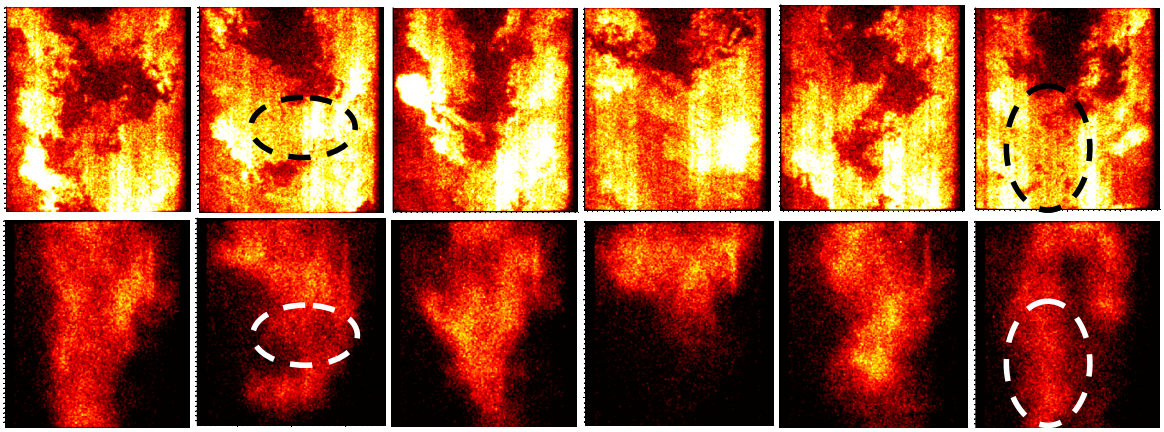

Figure 22. Single shot OH PLIF (top) and simultaneous chemiluminescence (bottom) images acquired over part of the insulated combustor ranging from x ~ 150 to 230 mm. (ϕ=0.58, loading of 8.1 g/s)

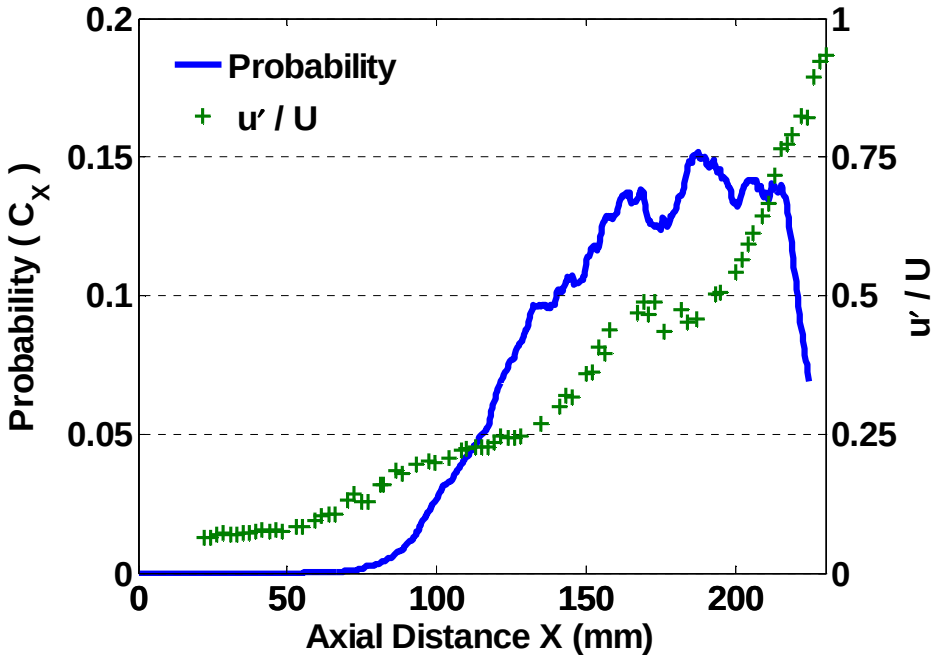

Figure 23. Probability of finding a flame edge (C_x) and turbulence intensity variation along the centerline for a flow rate of 8.1 g/s and ϕ=0.58.

4.3 Product Entrainment

Unlike a standard confined jet, where vortices are initiated at the initial shear region and propagate downstream, the SPRF geometry allows vortices carried by the return flow to propagate back towards the injector resulting in higher turbulence levels. The high speed inlet "jet" is highly turbulent and moves around a lot, leading to the creation of large vortices between the incoming and outgoing flows, as shown in Figure 24b. In the same general vicinity, the instantaneous (but non-simultaneous) OH PLIF results show regions of hot products being entrained into the cold reactants. Thus there is clear evidence of internal exhaust gas recirculation in the SPRF geometry. If the flame is lifted or the reaction zone is broken, as seen in Figure 24a, this can allow entrainment of products into the reactant stream. Also, the size of these vortical structures increases as we move downstream from the injector. The presence of larger eddies downstream, are also likely to cause the reactant jet to break down and mix with surrounding hot products. The hot products entrained and mixed into the reactants will tend to increase reaction rates (and flame speeds), enhancing flame stabilization in the downstream regions.

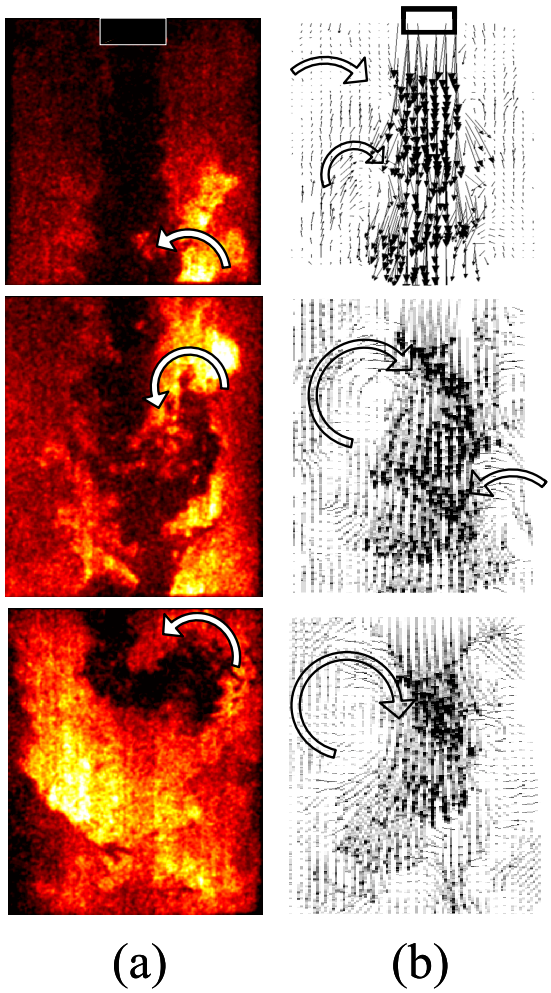

Figure 24. Product entrainment images (x/D_{a_in}=1.8-18): (a) instantaneous velocity fields, (b) instantaneous OH fields (acquired non-simultaneously), where arrows are used to mark large vortices in velocity field and apparent vortices in the OH field.

The possibility of hot product entrainment is further explored by making concentration measurements of all the major species in the combustor using Spontaneous Raman Scattering (SRS) at the same loading of 8.1 g/s and equivalence ratio of 0.58. Figure 25 shows the axial variation (averaged over 500 acquisitions) of mean mole fractions of CO_2 and CH_4 along the combustor centerline. The data extends from close to the injector to half way into the combustor (x/D_{a_in} = 0.4-14). Results show the presence

of product gases (CO_2) as early as x/D_{a_in}=5 along the centerline. The chemiluminescence images shown previously rule out the possibility that significant reactant burning occurs in this region. Thus, the appearance of the products is primarily due to product entrainment that starts relatively close to the injector plane. The Raman temperature measurements acquired along the centerline indicate an inlet temperature 450 K, which matches the inlet temperature measured with the thermocouple at the injector to within 30 K. Beyond x/D_{a_in}=5, the temperature is found to increase nearly linearly, approaching the adiabatic flame temperature of 1750 K in this case. The spike in temperature at x/D_{a_in}=12 is attributed to a possible decrease in laser power while acquiring data at this point. Equilibrium values of the (adiabatic) flame temperature and CO_2 concentration are also indicated in the figure for reference. A minor overshoot of the CO_2 data points over the equilibrium value is within the noise levels in the data.

While the averaged data suggest mixing of reactants and entrained products within the reactant jet, it is also possible that little mixing has occurred, and the data simply represent intermittent packets of essentially pure products. To differentiate these two options, instantaneous results acquired in regions of essentially pure product gases can be eliminated by conditional averaging. Pure product gases were defined to be points when the CH_4 concentration is less than a threshold value chosen to be 10% of the injected global fuel fraction, which is at least twice the noise in the CH_4 mole fraction measurement.

$$\hat{X}_i(x,r) = mean\ \left\{\ \ X_i(x,r,t)\Big|_{X_{CH_4}(x,r,t) > \frac{X^o_{CH_4}}{10}}\ \ \right\}$$

The mean axial variation of species mole fractions conditionally averaged in this fashion is also shown in Figure 25. The results are nearly the same as the unconditioned

averages up to $x/D_{a\_in} \cong 9$. The mixing of product gases into the reactants, as represented by the rising amount of CO_2, starts at x/D_{a_in} of 5 and reaches significant levels before reaching the flame zone in the second half of the combustor, where most of the heat release occurs. The amount of product mixing seems to reach a plateau around x/D_{a_in} = 11. The distribution of the reactant temperature (with entrained products) in Figure 25 is quite similar to the unconditional average close to the injector, but it saturates at ~1300 K before reaching the heat release zone. The lower temperature values found after conditional averaging are due to exclusion of data points with pure hot products.

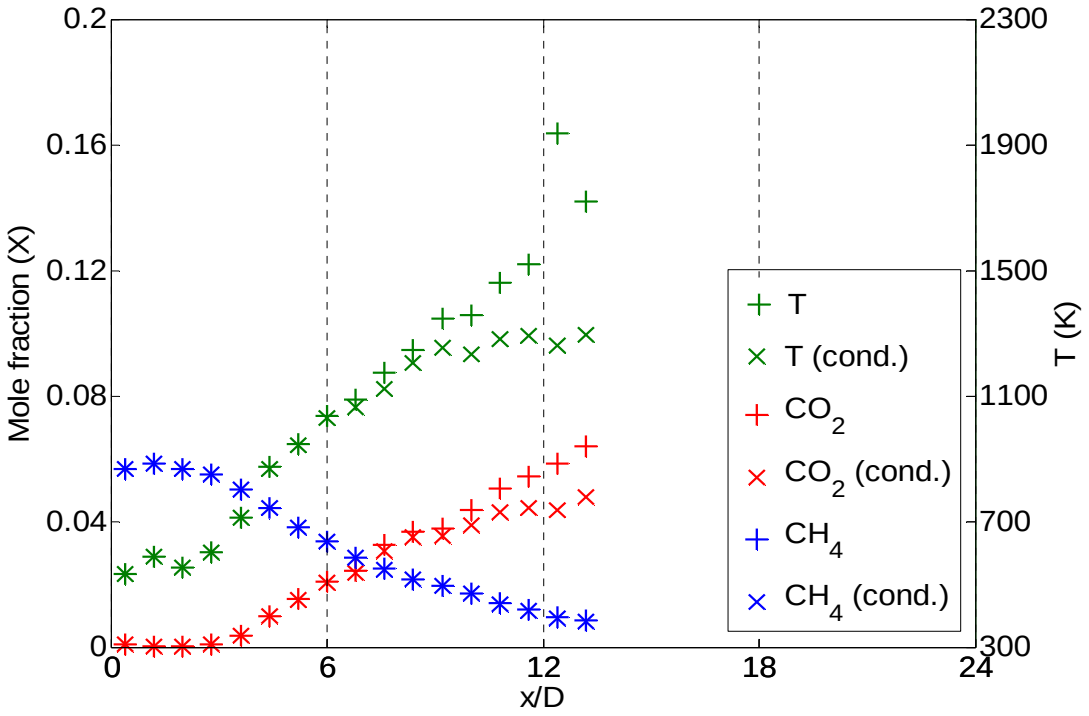

Figure 25. Axial variation of mean species mole fractions (CO_2, CH_4) and temperature along the combustor centerline. Conditionally averaged values of the same over data points only in the reactants are also plotted.

In systems with external recirculation of product gases, the amount of product entrainment is typically quantified by a single variable such as the product fraction (f_P),

which denotes the ratio of mass of products to that of the reactants at a given point. Based on this definition, f_P of 0 corresponds to pure reactants while pure products have a $f_P=\infty$. In the SPRF combustor, where the product gases are recirculated internally, the product fraction can be related to the local (measured) mass fractions as follows.

$$f_P = \frac{Y_{CO_2} + Y_{H_2O} + Y_{O_2)P} + Y_{N_2)P}}{Y_{CH_4} + (Y_{O_2} - Y_{O_2)P}) + (Y_{N_2} - Y_{N_2)P})};$$

$$Y_{O_2)P} = \frac{w_{O_2}}{w_{CO_2}}\left[\frac{2}{\phi} - 2\right]Y_{CO_2} \quad \text{and} \quad Y_{N_2)P} = \frac{w_{N_2}}{w_{CO_2}}\left[\frac{7.52}{\phi}\right]Y_{CO_2}$$

where, Y_i and w_i are the mass fraction and molecular weight of species i. Further $Y_{i)P}$ represents the mass fraction of the species i that ought to be present for a given mass of CO_2. Histograms of product fractions at six different axial locations along the combustor centerline are shown in Figure 26. The product fraction not only increases (on average) with axial distance but also is characterized by a wider distribution. By x/D_{a_in} of 12, the product fraction reaches values as high as 2, which correspond to 67% of the incoming mixture being hot products by mass.

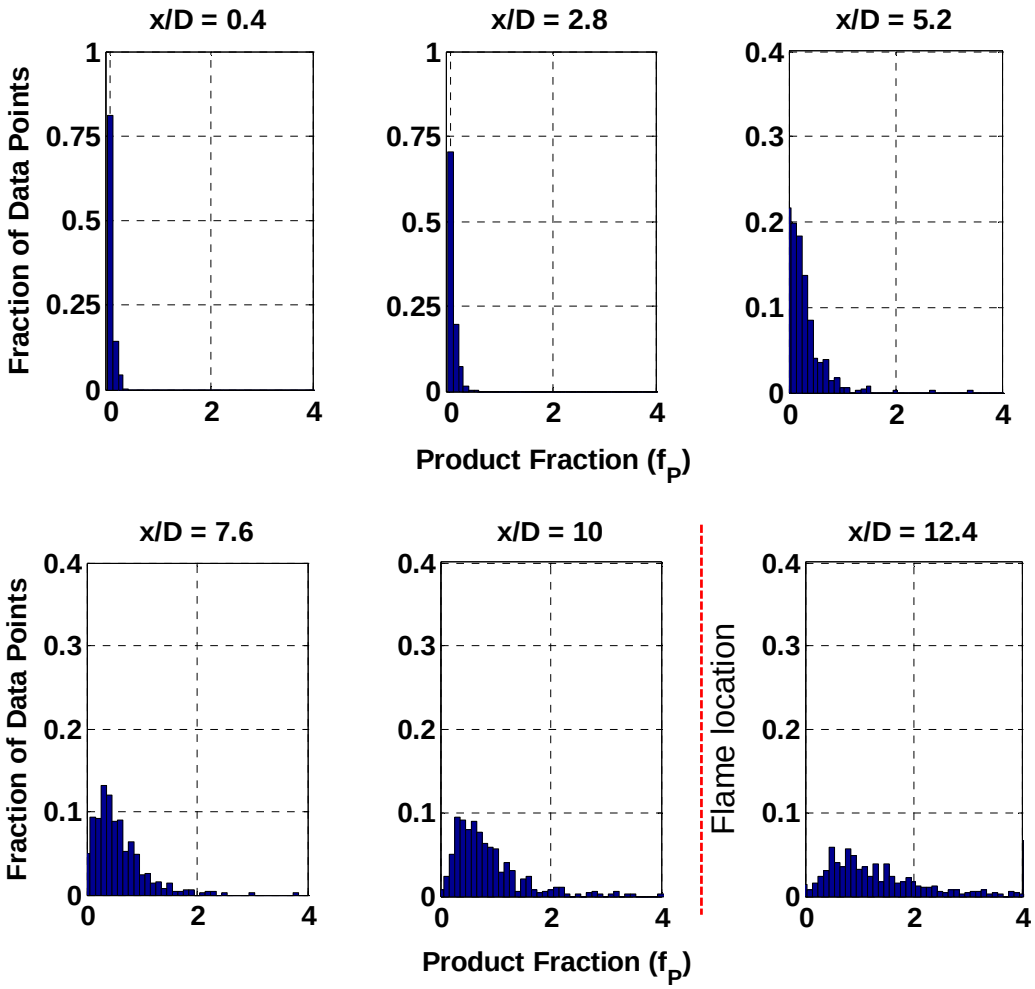

Figure 26. Histograms of the product fraction (f_P) over 500 data points measured at various axial locations along the premixed SPRF combustor centerline.

4.4 Ignition Time Scale Analysis

Combustors with large recirculation ratios and large residence times can have reactant mixtures that can reach the ignition temperature and thereby burn in what is called a flameless or mild combustion mode [15]. To explore such a possibility, we need to: (a) measure the variation of the recirculation levels in the combustor, (b) estimate ignition times given a certain level of recirculation and then (c) compare these estimates to the available flow times in the combustor.

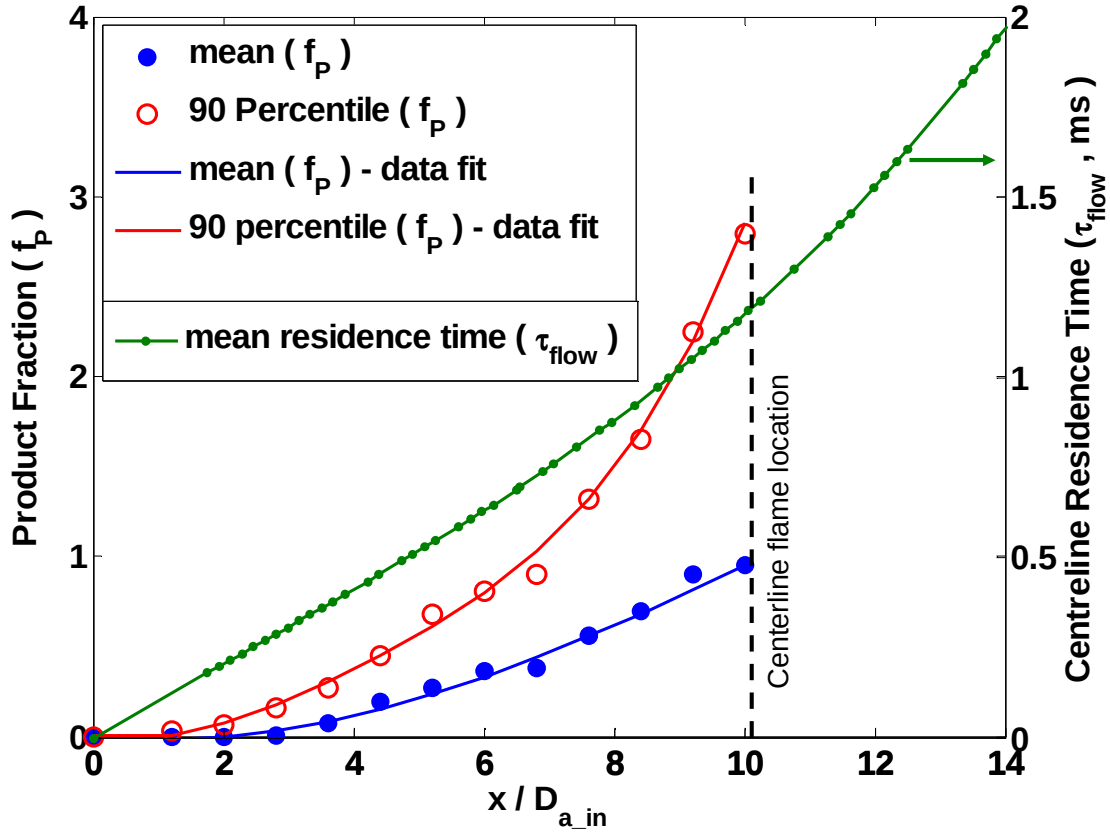

Figure 27. Axial variation of product fractions both mean and 90 percentile value along the premixed combustor centerline. Variation of mean flow times to reach a given centerline axial location calculated from the averaged flow field measurements is also shown along side.

The measured axial variation of recirculation levels along the SPRF combustor centerline is shown in Figure 27. As expected the average product fraction start at zero close to the injector and reaches a value of only about one (50% products by mass) before reaching the flame zone. It is possible that instantaneous product fractions higher than this could occur. In order to remove outliers in the data that likely result from measurement noise, we use an estimate of the local maximum product fraction that corresponds to the product fraction level below which 90% of the measured data occurs at that location. With this definition, the instantaneous product mass fractions reach

values as high as 2.8 by the flame zone region (Figure 26). The corresponding average centerline flow time needed to reach a given centerline axial location in the combustor is calculated from the mean velocity fields. These values reported in Figure 27 show that, the reactant entering the combustor has about 1.25 ms on average before reaching the flame zone.

To estimate the ignition times for various reactant mixtures, a plug flow reactor model (CHEMKIN) [9] was used. The effect of hot product gas entrainment was simulated by adding a fraction of hot, adiabatic products (produced from a pure reactant mixture) into the inlet reactant stream as indicated in Figure 28.

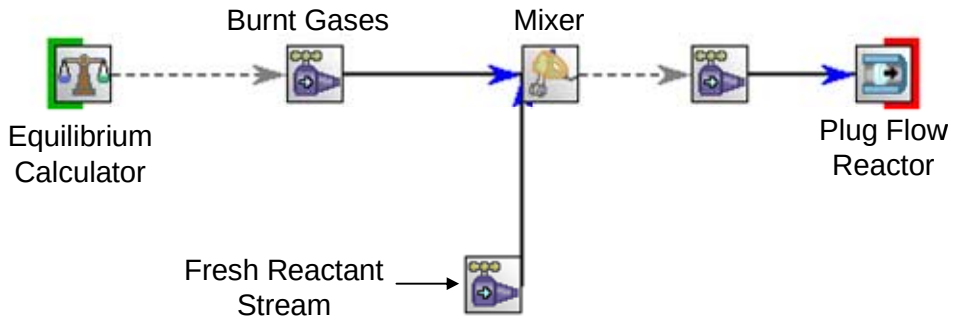

Figure 28. CHEMKIN reactor layout for ignition time scale analysis.

The initial fresh reactant temperature (before addition of products) was set to the reactant temperature determined from the injector thermocouple measurements. The PFR reactor inlet temperature further increases as hot product gases are added at different proportions, simulating the (adiabatic) entrainment of products before reaching the flame zone in the SPRF combustor. The ignition delay as a function of product fraction level in the reactant mixture is shown in Figure 29 for a range of equivalence ratios in this simulation. With increasing recirculation levels, the reactant temperature increases,

reducing the ignition delays in the combustor. Also increasing equivalence ratios cut down the ignition delay significantly as expected due to increased reactivity. Since the actual combustor is not completely adiabatic, these ignition delays should be considered lower limits for the actual ignition delays at each condition.

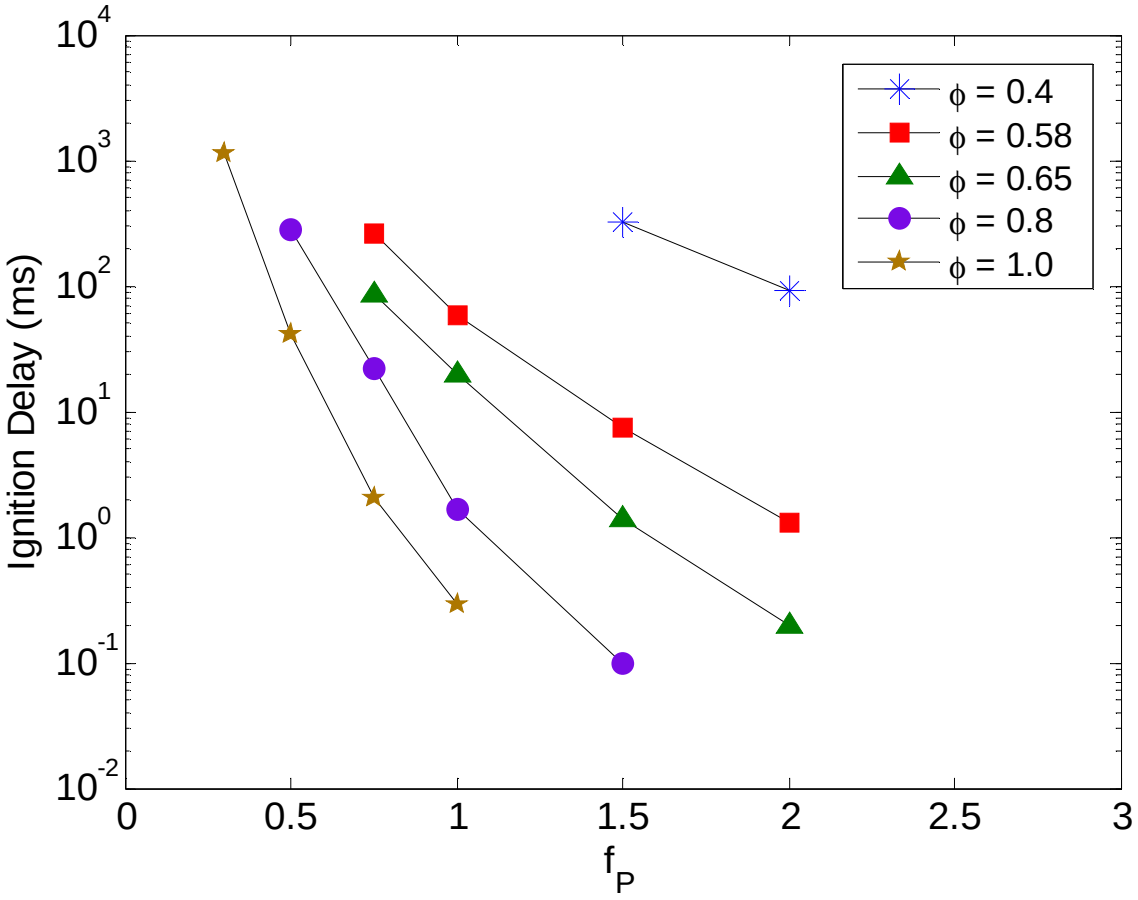

Figure 29. Variation of ignition delays in milliseconds with increasing recirculation levels represented by the product fraction (f_P) over a range of equivalence ratios.

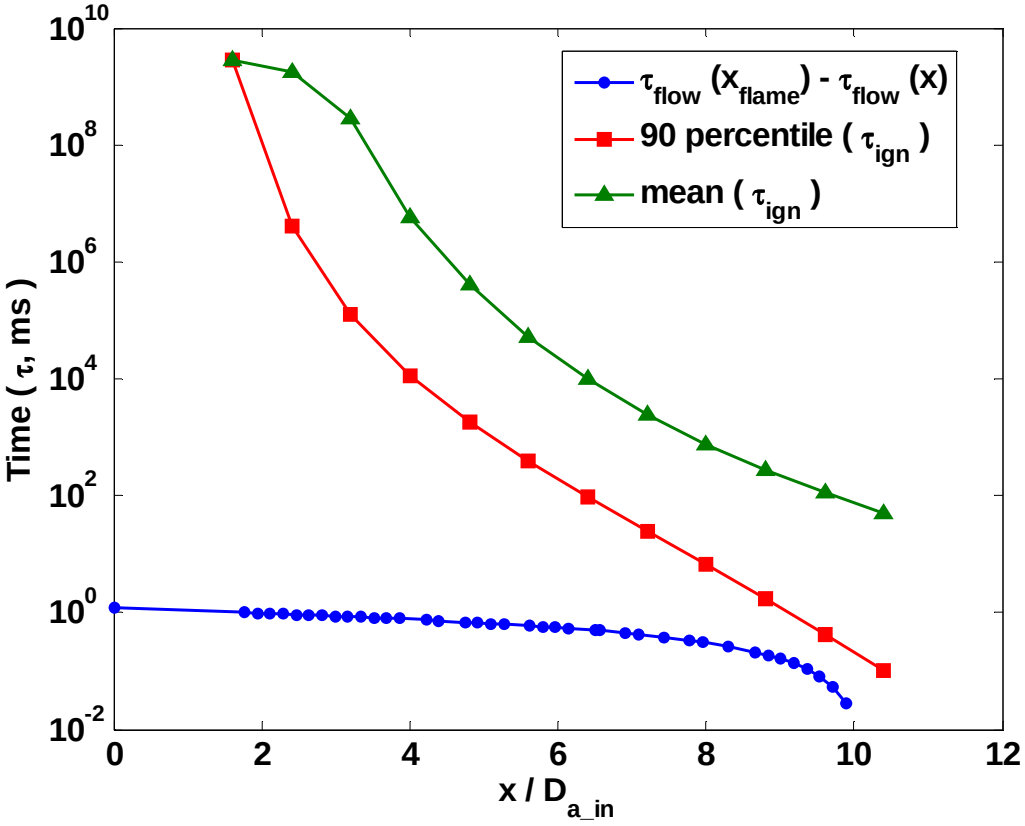

Figure 30. Axial profiles of the ignition time (in milliseconds) along the combustor centerline accounting for the change in recirculation level. Available flow time from a given axial location to the flame zone is also shown to explore the possibility of autoignition in the combustor.

By combining the modeled ignition delays and measured local compositions, the time required for the reactant mixture to ignite at a given location in the combustor can be found for both the mean and maximum (worst case) recirculation levels. The results (τ_{ign} in Figure 30) show the delay dropping a few orders of magnitude due to increasing product recirculation with axial distance. Furthermore, the time left to reach the flame zone from the current axial location ($\tau_{flow}[x_{flame}]-\tau_{flow}[x]$) is also plotted in Figure 30). For the mean recirculation measurements, the ignition time is at least two orders of magnitude more than the available flow time. Even with the worst case assumption that

the reactants reach the near maximum product fraction level of ~ 2.8, the simulations suggests that the flow times needed to reach the measured heat release region at x/D_{a_in} of 10 are too short for the mixtures to autoignite at the operating equivalence ratio (ϕ =0.58).

4.5 Flame Structure

Since the SPRF combustor does not appear to operate in a flameless, or mild combustion mode, we further examine the turbulent flame structure of the SPRF combustor using the approach developed by Borghi [47] and modified by Peters [48]. The analysis can provide valuable information about the relative roles of chemical versus mixing/flow time scales at various spatial locations, which will be useful for developing reduced order models of the combustor operation. This approach requires determining the total rms velocity (u'_{rms}), laminar flame speed (S_L), integral length scale (L_T) and flame thickness (δ_L) in the SPRF combustor. The rms velocities were obtained from 400 instantaneous PIV images. Since only two velocity components were measured, the total rms velocity was estimated by assuming the out-of-plane velocity component was comparable to the in-plane, lateral component. Further, the integral length scale is found by integrating the turbulent velocity correlation function computed from the instantaneous velocities. The flow parameters and turbulence characteristics estimated at different locations are listed in Table 5.

Table 5. Flow conditions and spatial locations used for regime analysis.

Equivalence Ratio, ϕ				0.58
Mass Loading				8.1 g/s
Reactant Injection Temperature, T_{react}				450 K
Location	**x/D**	**r/D**	**u'_{rms} (m/s)**	**L_T (mm)**
1	3	1.1	14.4	2.7
2	9	1.8	13.3	5.6
3	15	0	15.9	10.4

The flame speed and thickness, S_L and δ_L, were estimated with premixed, laminar flame simulations (CHEMKIN PREMIX and GRIMech 3.0) [9] for conditions close to the measured entrainment levels, as listed in Table 5 and Table 6. The effect of hot product gas entrainment was simulated as in the plug flow case. The flame speed was defined to be the simulated approach velocity, while the flame thickness was assumed to be the difference between the burned and unburned gas temperatures divided by the peak temperature gradient in the preheat zone.

Table 6. Flame properties obtained from CHEMKIN (GRIMECH 3.0).

f_P	**Flame Thickness δ_L (mm)**	**Laminar Flame Speed S_L (m/s)**
0	0.73	0.27
0.5	0.60	0.90
1.0	0.57	1.6
1.5	0.565	2.3
2.0	0.58	3.0

The flame structure analysis was performed for five entrainment levels and three spatial locations in the combustor. The first two locations chosen are in the shear layer, at x/D_{a_in}=3 and 9. These regions are highly strained due to high incoming reactant velocities and reverse flow, product gas velocities. The third spatial location is x/D_{a_in}=15 on the centerline, where the OH and chemiluminescence images indicate most of the heat release occurs. It can be seen from Figure 31 that the conditions at all these locations (except with zero product entrainment) fall in the thin reaction zone regime suggested by Peters [48]. In this region, one expects a distinct reaction zone unaffected by turbulence. For comparison, typical flames in stationary gas turbines are also characterized by thin reaction zones, but with extremely high turbulent Reynolds numbers ($Re_T > 10^4$), Da~1 and Ka>10 (see Figure 25) [30].

The likely turbulent flame structure is seen to evolve through the combustor. Close to the injector, u'_{rms}/S_L is high since there has been little chance for product entrainment, and L_T/δ_L is low because the shear layer is thin and the vortices are smaller. As the flow moves farther from the injector, L_T/δ_L increases and u'_{rms}/S_L decreases because the characteristic eddy size increases, and because the amount of product entrainment is expected to increase (producing faster S_L and thinner $\delta_{L)}$. Hence we expect the combustion structure to evolve as indicated by the diagonal arrow in Figure 25; making the combustion more flamelet like farther from the injector. As mentioned before, the reactant temperature increase and the presence of radicals due to product entrainment boost the mixture reactivity more than the reduction in reactivity due to dilution. This is evident from the flame speeds calculated including all these effects, shown in Table 6. Increasing product recirculation level from zero to two causes the reactant temperature to

go up to 1300 K. This translates to an order of magnitude increase in flame speed despite the reactants being diluted with twice their mass in products. It should be noted that the flame calculations assume recirculation/entrainment of equilibrium products. In practice, the concentrations of flame radicals in the entrained products may be higher, which would increase S_L further and push the combustion structure even closer to the flamelet regime. These results are consistent with the previous observations. In most of these regions, we see high OH gradients, consistent with thin reaction zone.

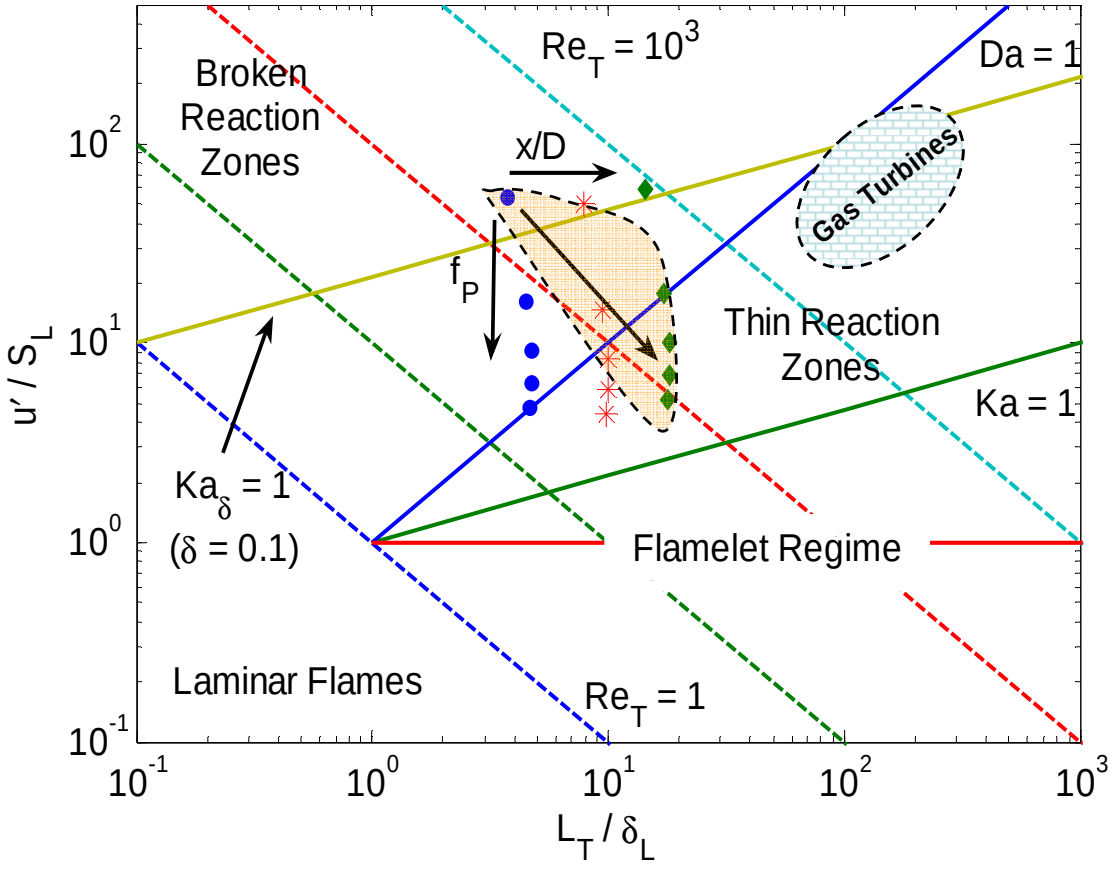

Figure 31. Estimate of turbulent combustion regimes for the SPRF combustor with points shown for conditions in Table 5 and Table 6.

Very close to the injector, the flame is lifted due to the high values of U/S_L. While the flame can exist further from the injector, in the shear layer between the forward flowing reactants and the reverse flow products, high intensity, small vortices may be able to extinguish the flame. This would permit products to be entrained into the unburned reactants. Further downstream, there would then exist reactant-product mixtures with high turbulent flame speeds, due to high S_L and u'_{rms} (but $u'_{rms}/S_L<10$). As the mean velocities drop in this region, the flame can be stabilized, even at very lean conditions where the NO_x emissions from the combustor are minimal. This relatively low velocity region in the downstream region of the combustor is the primary stabilization mechanism and the weak flame seen along the shear layer does not play a significant role in this regard as shown in non-premixed case presented later in the thesis.

To put this work in perspective with the different flame stability limits found by Wunning *et al*. [15], the operating conditions of the SPRF combustor are indicated (in red) on a schematic diagram of stability limits for different combustion modes involving exhaust gas recirculation (Figure 32). In that work, the reactants entering the combustor were diluted with cooled exhaust gases and then, preheated to the furnace temperature. Thus, the extent of product recirculation and the reactant preheat temperature were controlled independently. It should be noted that in case of the SPRF combustor, the product gases are recirculated internally and not significantly preheated (reactants are at 450K) before entering the combustor. The reactant temperature rise is therefore primarily due to mixing with near adiabatic product gases inside the combustor before the flame zone. Hence, the reactant preheat temperature is strongly coupled with the recirculation ratio. Most of the heat release in the SPRF combustor occurs in the narrow band shown,

which falls in the unstable zone where the flame is lifted and would blowout in other combustors. However, the recirculation of nearly adiabatic product gases laden with radicals along with the robust flame anchoring stagnation zone allows the SPRF combustor to operate stably at an ultra lean stoichiometry even though the flame is lifted off from the injector. The small recirculation ratio allows for a compact combustor in applications where space and weight are a concern, offering higher power densities.

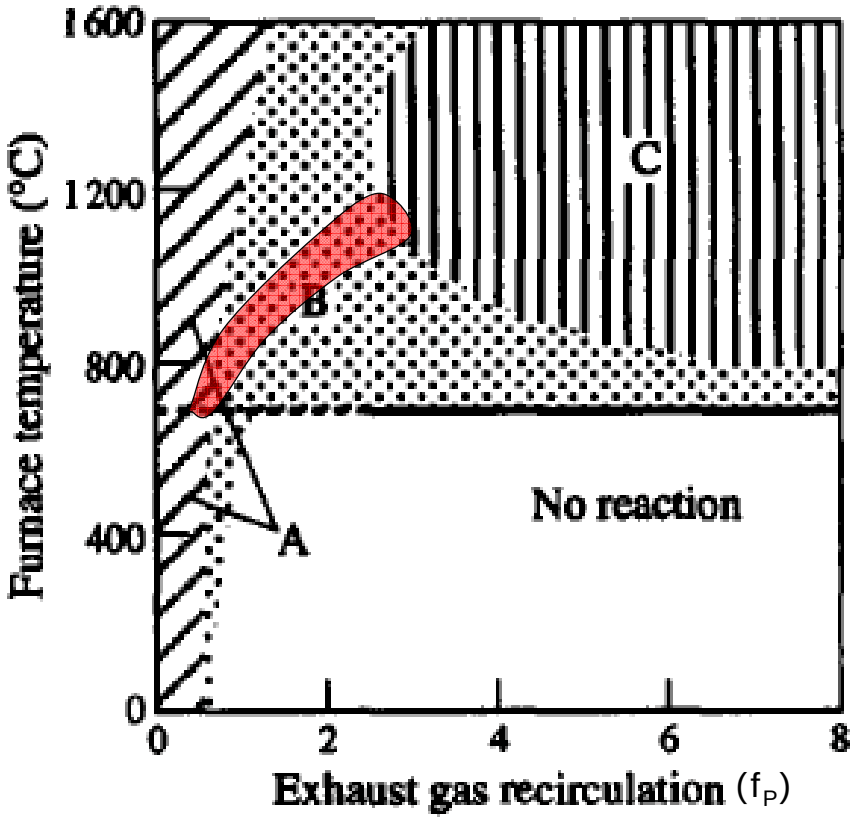

Figure 32. Schematic of flame stability limits by Wunning [15]. Also shown is the map of operating conditions of the SPRF combustor in red.

CHAPTER 5

NON-PREMIXED COMBUSTOR OPERATION AND SCALING

While the previous chapter focused on premixed operation of the SPRF combustor, a non-premixed (or only partially premixed) mode of operation is preferred for most practical combustion systems due to reliability and safety concerns. This chapter explores the non-premixed SPRF combustor, especially the reason for the low emissions that are on par with the SPRF combustor operating with fuel and air completely premixed before injection. The first section outlines the prominent features of the flow field and combustion characteristics in the non-premixed mode, including a comparison to the corresponding measurement in the premixed combustor. The second section deals with ascertaining the mixing field in the non-premixed combustor, which determines the mixture preparation before reaching the flame zone. This involves quantifying the entrainment of product gases, which have an impact on flame stability, and the fuel-air premixing levels, which influence the emission performance. Tailoring the combustor for specific applications at different power levels requires knowledge of how these processes scale with changes in combustor geometry. Therefore in the last section, the influence of various geometrical parameters on fuel-air mixing is investigated and a scaling rule is proposed.

5.1 Flow field and Combustion Characteristics

The mean velocities and turbulence intensities measured in the nonpremixed mode are compared to that of the premixed mode in Figure 33a. Near the open end of the combustor ($x<100$ mm), the centerline axial velocities are higher for premixed

combustion. This is likely due, at least in part, to the difference in effective inlet area, as the premixed operation utilizes only the annular passage of the concentric injector; the lower area induces a higher exit velocity. This difference should not persist more than a few injector diameters as the inlet jet expands. Thus further downstream, the axial velocities are seen to be approximately equal, but with the premixed mode exhibiting greater levels of unsteadiness. Still, the overall flow features are similar for both modes of operation, with the presence of a low mean (U) and high fluctuation (u'_{rms}) velocity region in the second half of the combustor, which was shown to help stabilize the flame for premixed operation.

The importance of this region for nonpremixed mode is evident from the average (100 images) chemiluminescence field (Figure 33c). Most of the heat release in this case occurs for $150<x<220$ mm. Unlike the premixed combustor (Figure 33b), there is negligible heat release close to the injector; the flame is completely lifted and stabilized only in the region of lower velocity and high unsteadiness. The large standoff distance should provide time for fuel and air to mix, and also allow the reactants to entrain significant amounts of products, thus forming a preheated and diluted mixture before combustion occurs. The reduced heat release in the first half of the combustor also explains the lower initial velocities found for nonpremixed operation; the lower heat release causes less expansion and a reduced acceleration of the flow.

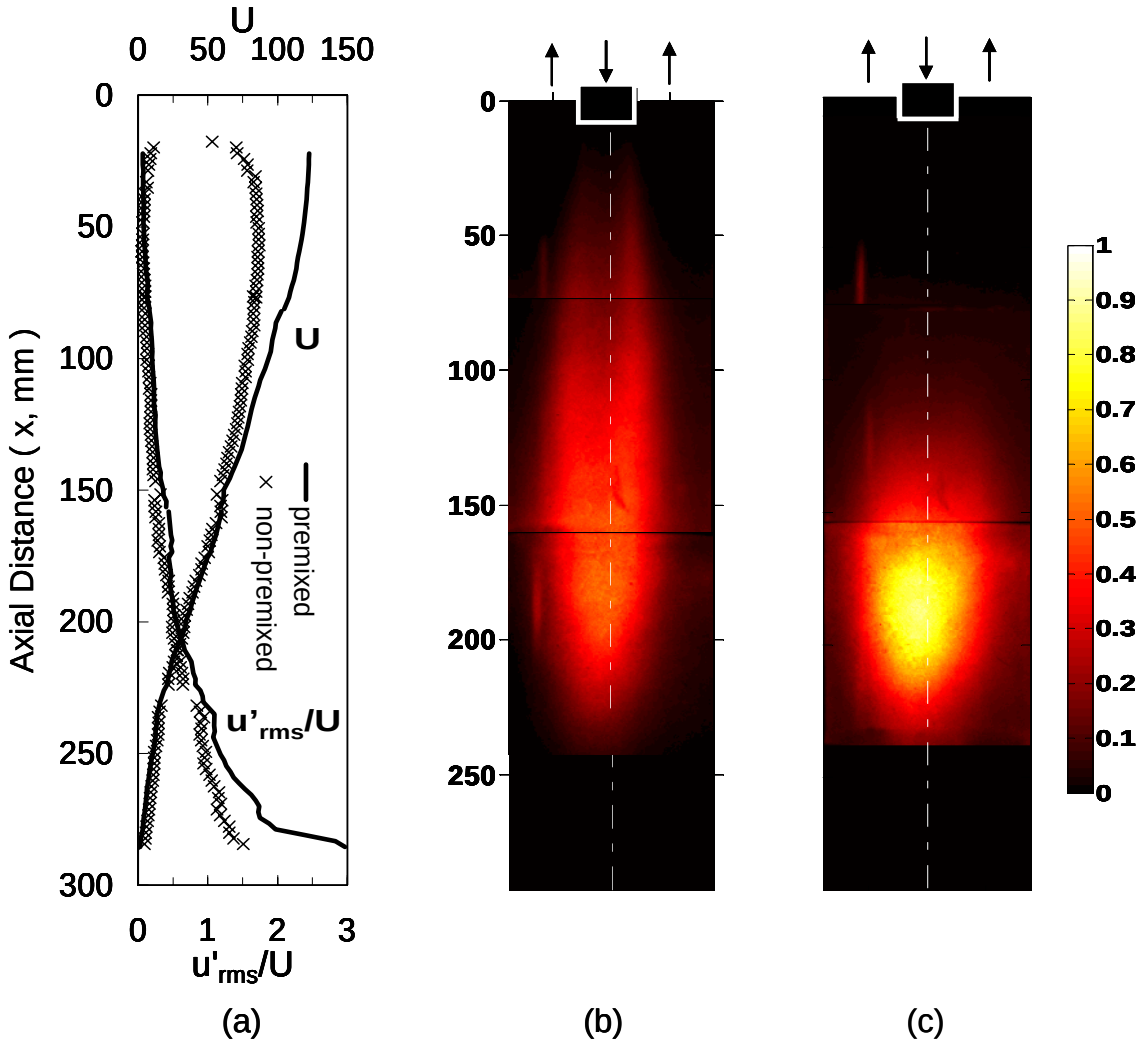

Figure 33. (a) Mean centerline velocity and turbulence intensity profiles followed by mean chemiluminescence field in the (b) premixed and (c) non-premixed modes of operation in the SPRF combustor at ϕ=0.6 and a loading of 8.1g/s.

5.2 Mixing Characteristics

The shear layer between opposing streams of hot product gases and reactants, together with shear layer between fuel and air in the non-premixed combustor, controls the mixture preparation. This in turn decides the stability and emission performance of the combustor. Hence, the mixing of these streams is of great significance. The effect of

shear on mixing quality is examined with concentration measurements for two different flow conditions, summarized in Table 7, at the same mass loading (8.1 g/s) and equivalence ratio (ϕ=0.6). Case I corresponds to the baseline combustor geometry used to produce the ultra low NO_x reported earlier. In Case II, the air velocity is reduced by increasing the outer diameter of the air injection annulus while maintaining the same size fuel tube (and fuel velocity). Both product entrainment and fuel-air premixing quality are surveyed for both the two flow conditions while all other conditions are held constant.

Table 7. Changes in flow conditions to study the effect of air velocity on mixing characteristics.

	Case I (High Shear)	**Case II (Low Shear)**
Air Tube Diameter (D_{a_in}, mm)	12.5	21
Fuel Tube Diameter (D_{f_in}, mm)	4.7	4.7
Air Injection Velocity (U_a, m/s)	117.2	34.9
Fuel Injection Velocity (U_f, m/s)	22.23	22.23
Product Return Velocity (U_P, m/s)	11.67	12.68

5.2.1 Product Entrainment

Extent of product recirculation, indicated as the mole fraction of CO_2, along the combustor centerline is shown in Figure 34. For the baseline configuration (Case I), non-premixed operation of the combustor is found to have CO_2 concentration levels similar to that of the premixed combustor before reaching the flame zone. However, appreciable levels of CO_2 appear along the centerline only later in the non-premixed case compared

to the premixed combustor. This is probably due to the reduced velocities and thereby reduced shear in the initial part of the non-premixed combustor as reported earlier. In the case with reduced air velocity (Case II), product entrainment is found to diminish for both modes of operation as expected due to the reduced shear between incoming reactants and products in addition to increased distance of product stream from the centerline. Further, the flame zone is also found to move upstream reducing the distance available for mixing.

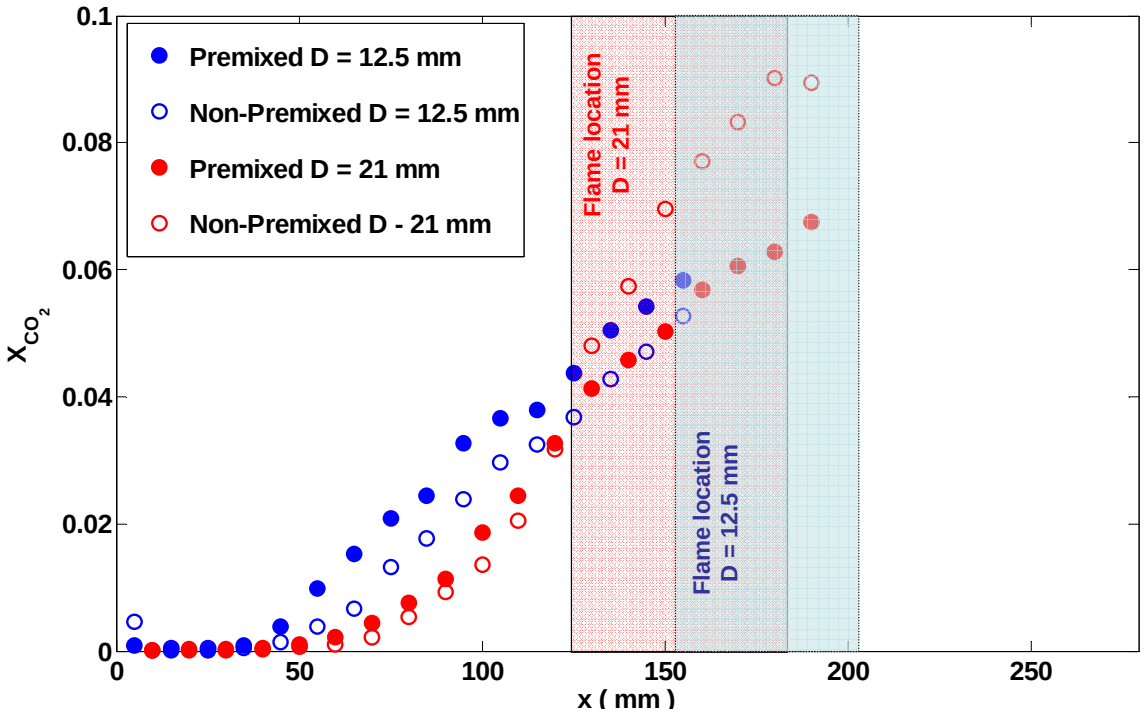

Figure 34. Variation of mean CO_2 mole fraction along the combustor centerline for premixed and non-premixed modes of operation and both the configurations in Table 7.

The baseline non-premixed configuration is able to produce NO_x emission levels comparable to the operation when the fuel and air are completely premixed. It is possible that in addition to contributing to combustor stability as outlined in the previous chapter,

the product entrainment could have altered the production of NO_x emission. To explore the possibility, that recirculation of hot product gases has an effect on NO_x emissions at a given equivalence ratio, laminar one-dimensional flame simulations (CHEMKIN, GRIMech 3.0) were carried out. The effect of hot product gas recirculation was simulated by adding a fraction of hot products ($f_P \equiv$product mass fraction in the reactants) back into the inlet reactant stream. The temperature and composition of the adiabatic products was based on results for $f_P = 0$. Results were obtained at two initial reactant temperatures (before mixing) of 300 and 600 K. The air temperature measured at the inlet of the combustor is between these values. The simulated emission levels (Figure 35) correspond to the "prompt" NO_x concentration, defined here as the NO_x just after the flame's heat release region (i.e., where the heat release has dropped to 1% of its peak value). The adiabatic flame temperatures for the two cases are 1630 K and 1860 K respectively. At these relatively low flame temperatures, the amount of thermal NO_x produced downstream is expected to be low.

In both cases, EGR of adiabatic products appears to do little to the NOx emissions. For an initial reactant temperature of 300 K, corrected NO_x emissions (at 15% O_2) obtained for different product fractions show little variation with increasing f_P. For the elevated preheat temperature of 600 K and with 50% of the preflame mixture being products (f_P=1), the NO_x emission increase from ~2 to 3 ppm. Hence, moderate amounts of product entrainment do not appear to reduce NO_x for a given level of fuel-air mixing (and in fact may increase it by a small amount). To compare the product entrainment effect to the influence of only partial premixing of fuel and air, the figure includes a third case, with a richer mixture, equivalence ratio of 0.7 (at the higher preheat temperature of

600 K), but with no product entrainment. The flame NO_x increases to 3.5 ppm, and since the adiabatic flame temperature of this condition is over 2000 K, some added thermal NO_x would be likely. These modeling results indicate that the recirculation of (adiabatic) product gases in the non-premixed SPRF combustor should not significantly effect the production of NO_x emissions compared to when the fuel and air are only partially premixed. Hence, the next section is focused on the vital aspect of fuel-air mixing in both the above mentioned combustor configurations.

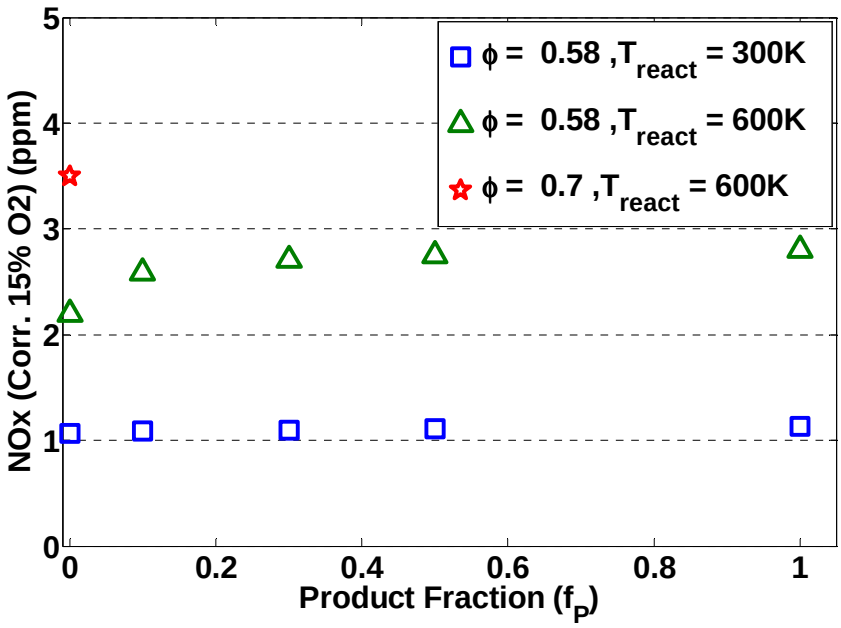

Figure 35. Effect of adiabatic exhaust gas recirculation on flame NO_x from laminar flame calculations.

5.2.2 Fuel-Air Mixing Measurements

The shear between the fuel and air streams plays a vital role in the extent of mixing. To maintain low emission levels, the fuel and air that are injected separately should have a chance to premix down to the global (lean) stoichiometry before reaching the flame. Therefore, the effect of changing shear on the premixing quality is examined in

the non-premixed mode using the concentration measurements in the two cases mentioned in Table 7.

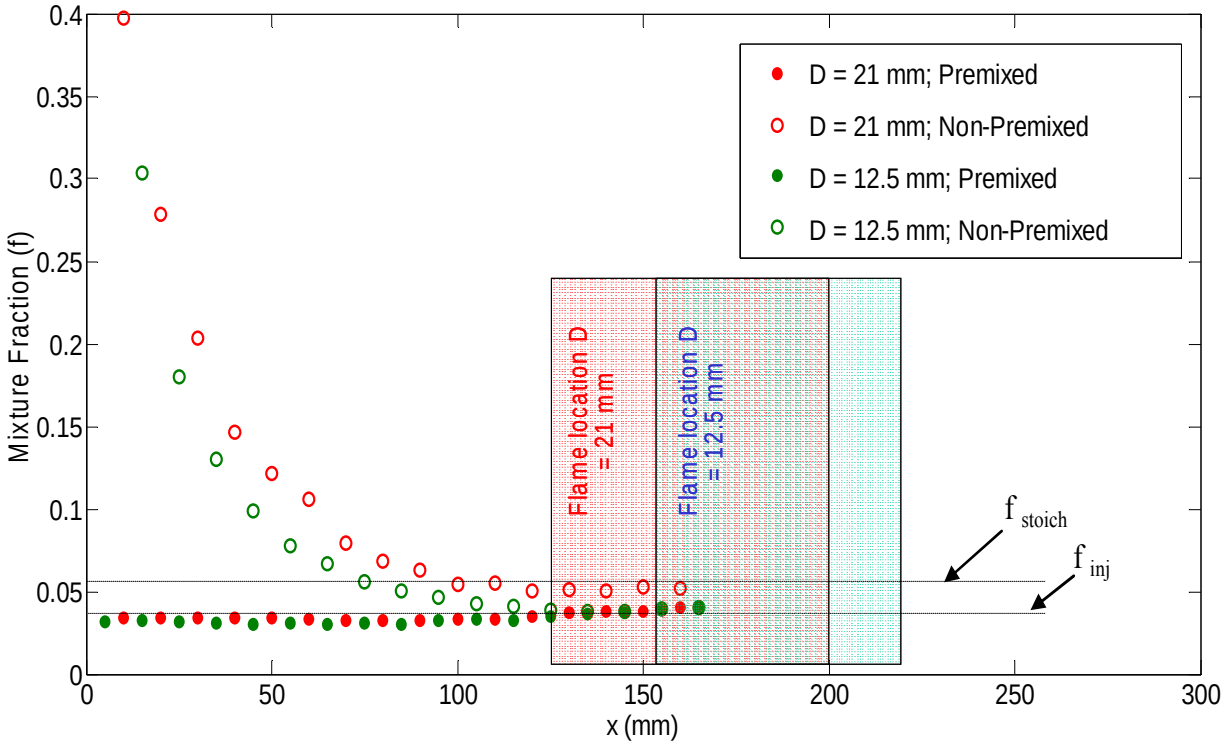

Figure 36. Axial variation of mean mixture fraction (*f*) based on C and H atoms in the SPRF combustor operating at loading of 8.1g/s and ϕ=0.6 for conditions 1 and 2 shown in Table 7. Also shown is the location of the flame in these cases. For comparison mixture fraction values in the premixed combustor are also plotted.

The extent of fuel-air premixing in the combustor is typically quantified by a single parameter, the mixture fraction (*f*) as defined by Bilger [49]. The mixture fraction represents the fraction of mass at a point that originated in the fuel jet. It can be calculated from the measured concentrations accounting for the C and H atoms in the combustor. The mixture fraction takes values between zero and one, corresponding to no mass from the fuel stream (i.e., pure air) and pure fuel. The variation of mean mixture

fraction ($\bar{f}$) along the combustor centerline is depicted in Figure 36 for both premixed and non-premixed modes of combustor operation. In the premixed mode, the mixture fraction level is found to be constant, as expected, and attains the same value for both flow conditions in Table 7, confirming that the combustor was operating at the same global stoichiometry. The stoichiometric and premixed injection mixture fraction levels are also shown in Figure 36 (dotted lines) for reference.

In the non-premixed mode, where fuel and air are injected separately, the mixture fraction in Case I is found to approach the premixed value by x = 125 mm, indicating that the injected fuel is rapidly diluted with air (and products) before reaching the flame zone which starts around x = 160 mm (shown in blue). This can be attributed to enhanced fuel-air mixing due to high shear, allowing the non-premixed mode to operate just like the premixed case. This helps explain the low values of NOx emissions measured in the non-premixed SPRF combustor as the reactants burn at a local fuel-air ratio that is lower than the stoichiometric ratio and nearly at the global stoichiometry, leading to low flame temperatures.

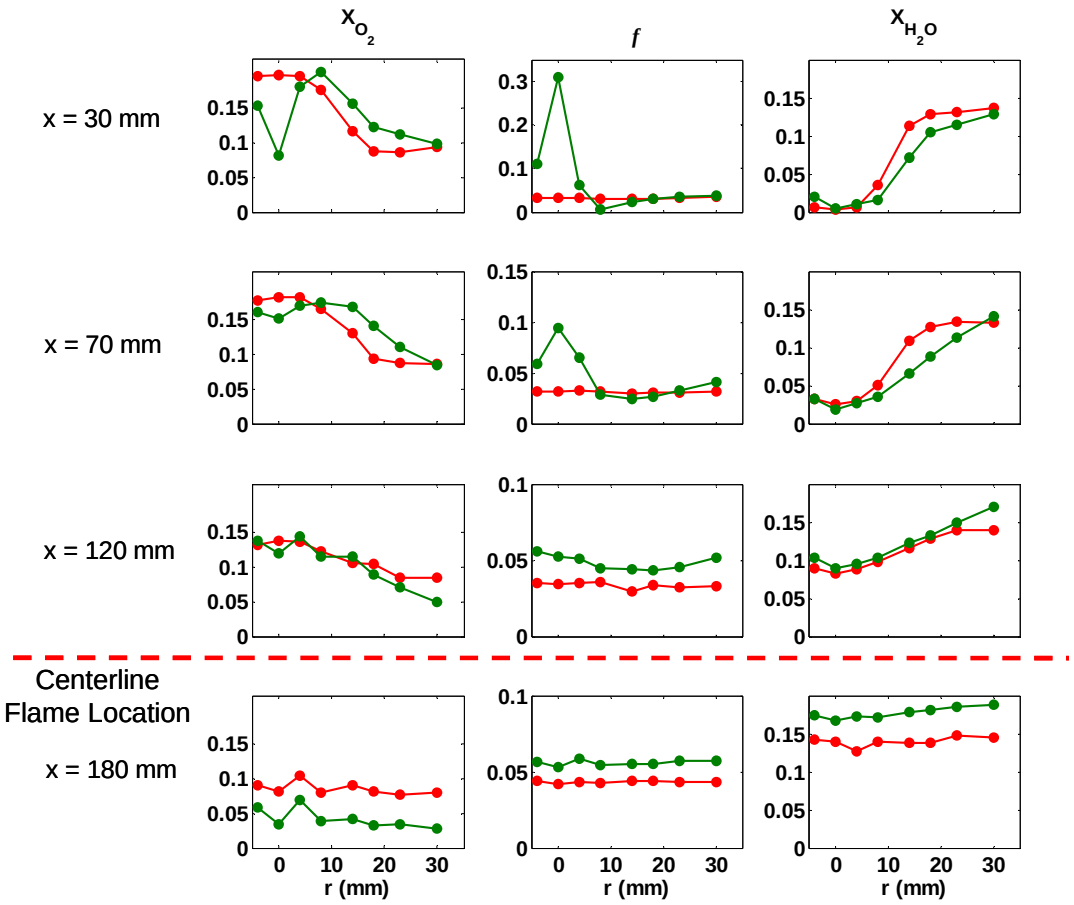

Figure 37. Radial variation of mean mole fraction of O_2 and H_2O along with mixture fractions at four different axial locations in the SPRF combustor (operating at a loading of 8.1g/s, ϕ=0.6) for Case II in Table 7. Variation in the non-premixed case is shown in green; premixed case in red. The location of the flame front along the centerline at x = 125 mm is also marked.

However for the 21 mm injector (Case II), where the shear is relatively low, the mean mixture fraction takes a significantly richer value relative to the premixed case. The fuel and air in this case reach the flame front (at x=125 mm) in almost stoichiometric proportions along the centerline. Radial profiles of the O_2, mixture fraction and H_2O are also examined for this configuration in Figure 37. The profiles in the non-premixed case (shown in green) are compared to that in the premixed case (red) at different axial

distances, showing the variation across a region slightly more than one half of the combustor diameter. Close to the injector (at x=30 mm), the fuel jet remains almost intact but the air is seen to spread out faster as evidenced by the higher O_2 and lower H_2O levels. At x=120 mm, which is just before the flame front (at 125 mm), the fuel content indicated by the mixture fraction is not just higher along the center line, but is also higher throughout much of the combustor width. The mixture fraction seems to drop with radial distance, initially indicating that fuel and air are better mixed away from the centerline but have not completely premixed, as occurred in flow Case I. This appears to be due to the lower shear velocity between the fuel and air. Further downstream in the flame zone (x=180 mm), all the profiles achieve a nearly constant value. A consistently higher mixture fraction in the non-premixed case indicates that some part of the air is not able to reach the flame zone but has previously reversed direction, leaving the combustor. Thus, when the air velocity is modified, this important aspect of reactant jet penetration has to be considered.

All the average mixture fraction data indicate incomplete mixing in the configuration with low shear on an average. To see if this is true even on an instantaneous basis, all the data points acquired in both these cases are shown in scatter plots (Figure 38). The figure shows the spread of H_2O mole fraction with the local mixture fraction at all the points on and off of the centerline at different axial distances. The equilibrium H_2O concentration for fuel burning at a given mixture fraction along with the global and stoichiometric mixture fractions are shown using dotted lines. The data points are color coded according to their axial distance from the injector (blue represents points close to the injector and red is close to the stagnation plate). Figure

38a,c shows the spread of data points acquired within an axial distance of 75 mm from the injector in both cases studies earlier. The data points with significant amounts of H_2O but a mixture fraction level below the global value, corresponds to locations in the air jet that has entrained some products but have not mixed with the fuel yet. On the other hand, points in the fuel jet (points with high mixture fraction level) show almost no H_2O. This suggests that the fuel jet is shielded from the product gases until it is reasonably diluted with the air. However when all the data points acquired in the combustor were plotted as shown in Figure 38b,d, we see a continuous variation of water levels unlike conventional diffusion flames. This is due to entrainment of product gases (containing H_2O) into the reactants.

For the baseline combustor (Case I), most of the data points in Figure 38b that have equilibrium levels of H_2O occur only around the global mixture fraction (f_{global}). We almost never find data points that appear to be completely burned (near equilibrium H_2O) and that approach stoichiometric levels. This indicates that even on a time resolved basis, the fuel burns in an almost premixed state for the Case I combustor, as suggested earlier. In contrast, Figure 38d shows a similar scatter plot for the configuration with reduced shear (Case II). Now the H_2O concentrations approach equilibrium levels for a wider range of stoichiometric, primarily for points at the bottom of the combustor. Thus the fuel burns over a wider range of fuel-air ratios from lean to stoichiometric. Hence, geometry of the combustor is seen to have a significant effect on the mixing characteristics and thereby the emission performance. How fuel-air mixing scales with changes in combustor geometry is further explored in the next section.

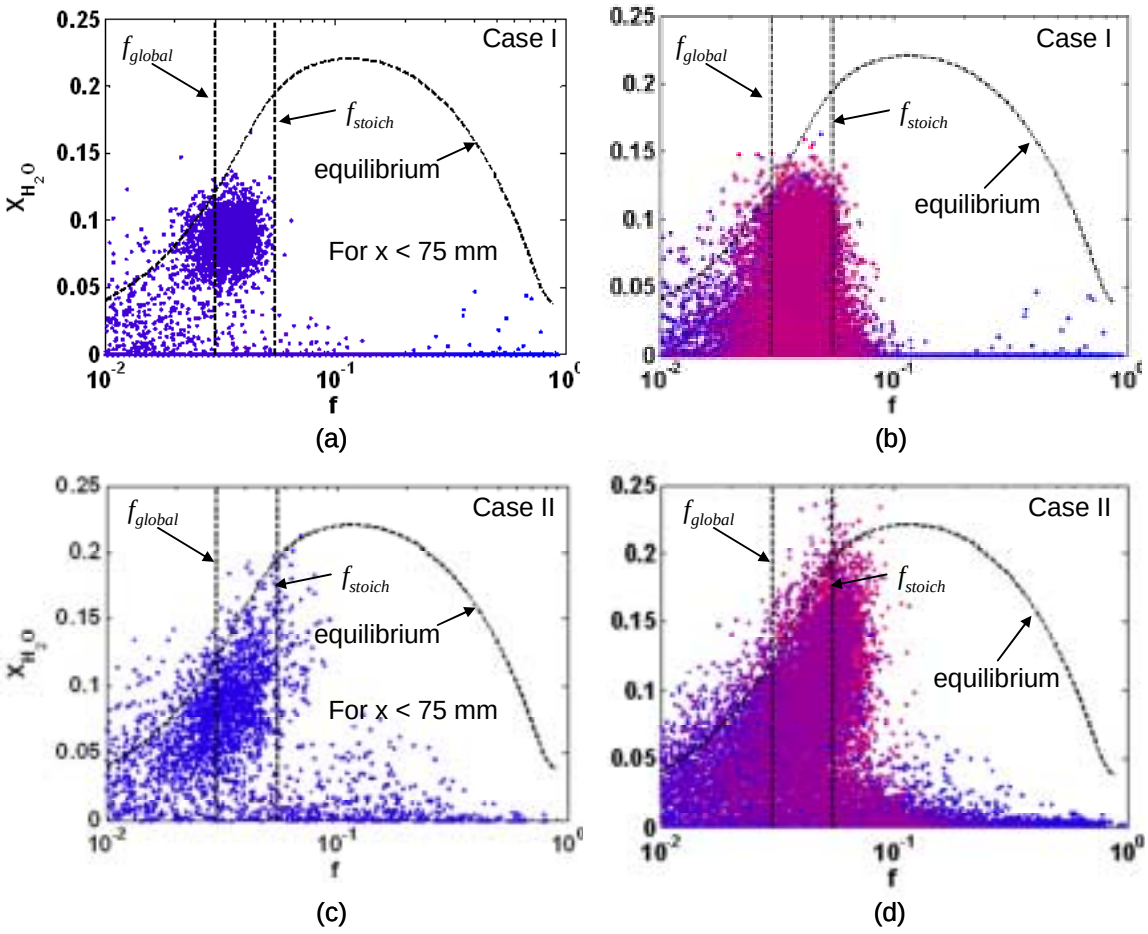

Figure 38. Distributions of instantaneous H_2O mole fraction including data points acquired in the combustor (both along the center and radial lines at different axial distances), in the non-premixed SPRF combustor for both cases in Table 7 (loading of 8.1g/s, ϕ=0.6). Data points color coded based on the distance from the injector (blue at injector and red at the stagnation plate). Equilibrium H_2O concentrations along with the global and stoichiometric mixture fractions are shown in dotted lines for reference.

5.3 Geometry Scaling of Fuel-Air Mixing

A number of issues affect the practicality of a combustor design, including maximum allowed pressure loss and combustor size, which is related to overall residence time. To estimate pressure losses inherent to the reverse flow of the SPRF combustor,

isentropic relations were used to estimate the drop in pressure due to flow stagnation. Figure 39 shows the variation of the fractional pressure loss with changing injection velocity. Pressure loss corresponding to the baseline combustor operating at a nominal loading of 8.1 g/s is estimated to be 5%. This estimate does not include the drop in pressure due to the combustion process and viscous losses. To limit these losses under 1%, the injection velocity (for air) needs to be restricted to less than approximately 50 m/s. Low velocities can be achieved for a given mass loading by modifying the injector dimensions.

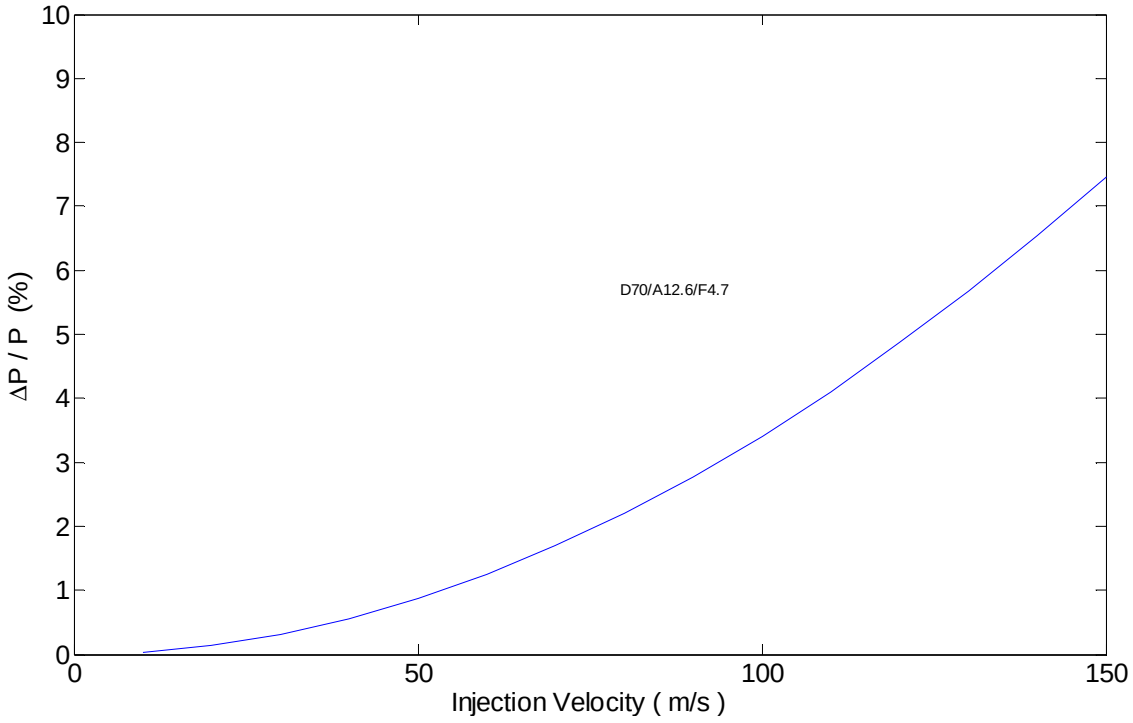

Figure 39. Percentage pressure drop variation due to stagnation in the combustor with varying injection velocity calculated using isentropic relations.

The overall residence time in a combustor is also a function of combustor geometry, including combustor length and diameter (i.e., combustor volume). For typical combustors, long residence time may elevate NO_x emission levels and contribute to

additional weight and volume. On the other hand, too short a residence time would lead to incomplete mixing and combustion. However mixing and time required for combustion can also be controlled by making other changes to the design dimensions. Changing the relative fuel and air injector areas alters the shear between these streams, altering the premixedness of the reactants at the flame zone, which has been shown to be vital for low emissions performance. The product entrainment and jet penetration can be altered by modifying the overall combustor diameter with respect to that of the injector. Hence with this basic understanding of the non-premixed combustor operation, the effect of changing various combustor and injector dimensions on mixing characteristics will be explored in subsequent sections. All the geometry scaling analysis henceforth is performed at a nominal mass loading of 8.1g/s and for an equivalence ratio of 0.6.

5.3.1 Effect of Change in Combustor Diameter

For this analysis, mixing levels are quantified using the centerline variation of the mean mixture fraction. The effect of changing the combustor diameter (D_c) on fuel-air mixing is demonstrated in Figure 40, with the outer quartz tube diameter increased from 70 to 90 mm for the same injector (21 mm air tube and 10.4 mm fuel tube) and combustor length of 279.4 mm. Decreasing the level of outer confinement from the baseline combustor seems to have a negligible effect on the mixing between the inner coaxial fuel and air jets. Hence, for the purpose of fuel-air mixing characterization, the injector configuration can be modeled as a free coaxial jet system.

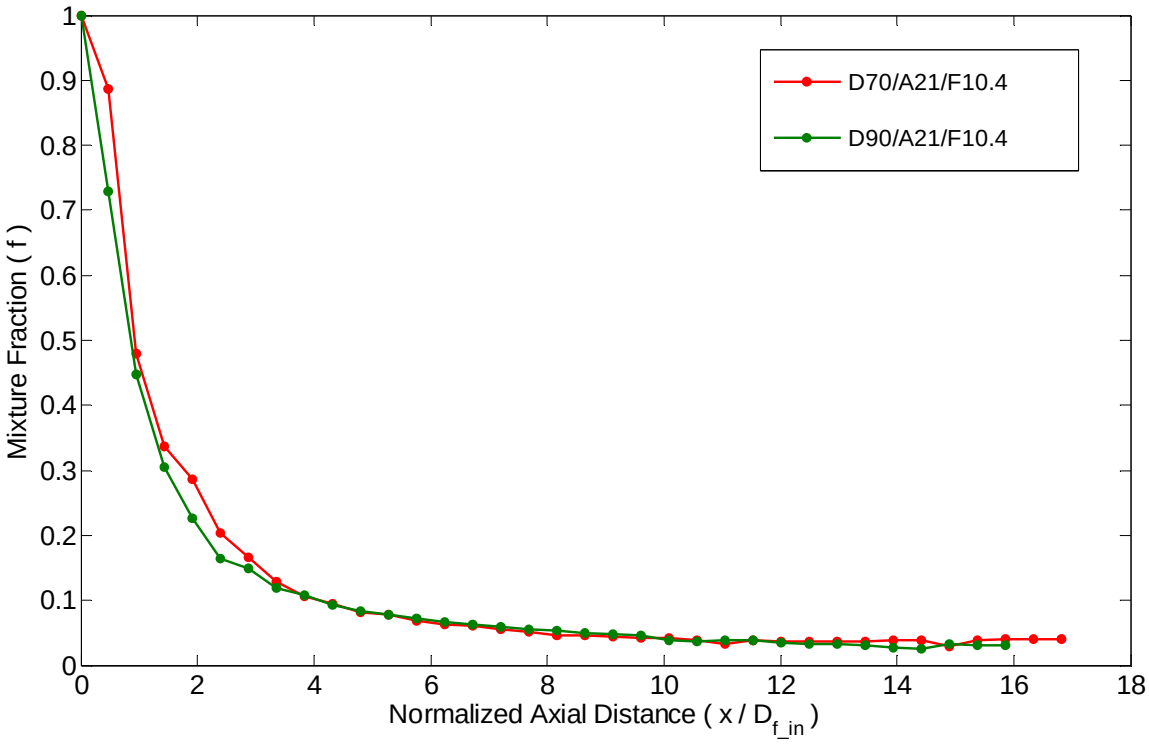

Figure 40. Variation of mean centerline mixture fraction with normalized axial distance for non-premixed SPRF combustor configuration operating at a ϕ=0.6 and loading of 8.1 g/s but for two different combustor diameters.

5.3.2 Effect of Change in Injector Dimensions

As noted above, lower injection velocities (for a given mass loading) should provide low combustor pressure drops. Thus we examine the effect of increasing air tube diameter. However to maintain the same level of premixedness as in the baseline configuration, the fuel velocity also needs to be tailored by changing the fuel tube diameter. Mixing characteristics of free coaxial jets and their scaling have been investigated in detail by many researchers. To help guide the geometry changes for scaling in the SPRF combustor, a mixing model by Villermaux et al. [24] that expresses the premixedness in terms of a dilution length is employed. The dilution length (L_d),

defined as the axial distance from the injector by which the inner jet fluid (fuel in this case) dilutes along the centerline to a given concentration level is expressed as:

$$L_d \propto \frac{D_{f\_in}}{M_{a/f}^{\frac{1}{2}}} = D_{f\_in}\left(\sqrt{\frac{\rho_f}{\rho_a}}\right)\left(\frac{U_f}{U_a}\right)$$

where D_{f_in} is the fuel tube inner diameter and $M_{a/f}$ is the momentum ratio of the air to the fuel jet. This indicates that the mixing between fuel and air is dependent on the ratio of velocities and not just shear between the jets. The dilution length can be non-dimensionalized and expressed in terms of only the geometric parameters for a given mass flow rate and an equivalence ratio.

$$\frac{L_d}{D_{f\_in}} \propto \left(\sqrt{\frac{\rho_A}{\rho_F}}\right)\left[\left(\frac{D_{a\_in}}{D_{f\_in}}\right)^2 - \left(\frac{D_{f\_out}}{D_{f\_in}}\right)^2\right]$$

In the current SPRF arrangement, we saw that low pressure drops can be obtained by keeping the air velocity under 50 m/s. This can be accomplished by increasing the air tube diameter (D_{a_in}), but to maintain the same mixing level the fuel velocity also needs to be reduced by increasing the fuel tube diameter (D_{f_in}). To test the predictions of this model, concentration measurements were performed in four different configurations with increased air and fuel tube sizes in addition to the baseline case. Figure 41 shows the variation of the centerline mean mixture fraction for these configurations and their corresponding details are listed in Table 8.

Table 8. Geometric parameters used and dilution length predictions from free coaxial jet model.

Configuration	U_a (m/s)	U_f (m/s)	D_{f_in} (mm)	D_{f_out} (mm)	D_{a_in} (mm)	$M_{a/f}$	L_d/D_{f_in}
D70/A21/F4.7	34.9	22.23	4.7	6.25	21	2.61	15.15
D70/A12.6F4.7	117.2	22.23	4.7	6.25	12.6	29.4	4.51
D70/A21/F10.4	51.59	4.54	10.4	13	21	136.6	2.09
D90/A21/F10.4	51.59	4.54	10.4	13	21	136.6	2.09
D90/A26.7/F16	40.31	1.74	16.8	19.1	26.7	567.6	1.03

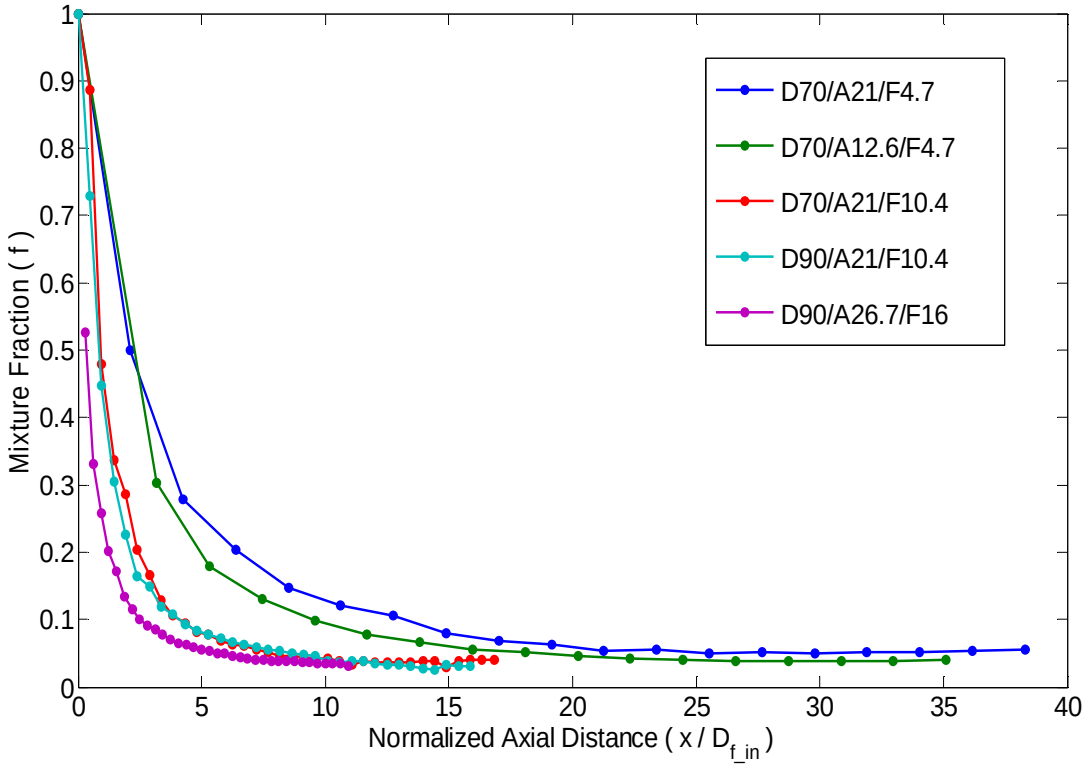

Figure 41. Variation of mean centerline mixture fraction with normalized axial distance for non-premixed SPRF combustor configuration for different injector dimensions at the same ϕ=0.6 and loading of 8.1 g/s.

It is evident from the figure that the higher momentum ratio configurations, corresponding to larger injector tubes, tend to mix well in fewer jet diameters. This follows the trend shown by the normalized dilution length predicted by the model. Even though the overall velocities and shear in the combustor are reduced for the 'D90/A26.7/F16' case, good mixing levels are achieved because the air and fuel jets have an increased interface area due to increased air and fuel tube dimensions. Even though this may appear counterintuitive, the result is that the dilution length is dependent on the ratio of fuel and air velocities rather than the shear between the streams.

This trend can be also seen from NO_x emission measurements at the exit of the combustor. Figure 42 shows these emissions for all the above cases as a function of the adiabatic flame temperature accounting for the internal preheating in the injector. All the configurations operating with premixed fuel and air behave similarly and show exponential temperature dependence; however the emissions in the non-premixed configurations differ depending on the mixing levels. The baseline configuration produces almost the same emissions in both the modes of operation indicating the best mixing performance. On the other hand, 'D70/A21/F4.7' case with the lowest air to fuel jet momentum ratio produced the highest emissions with other intermediate ratios yielding NOx emission levels in between these limits. The 'D90/A26.7/F16' configuration is able to match the performance level of that of the baseline case, for lean equivalence ratio's where temperatures are less than 1900 K, even though the air velocities are reduced by a factor of 3. Additionally, both data series corresponding to a change only in the outer combustor tube size produce similar emission levels, which supports the earlier conclusion from the mixing measurements that the lateral

confinement does not affect the inner coaxial jet mixing significantly (at least for the combustor size range investigated).

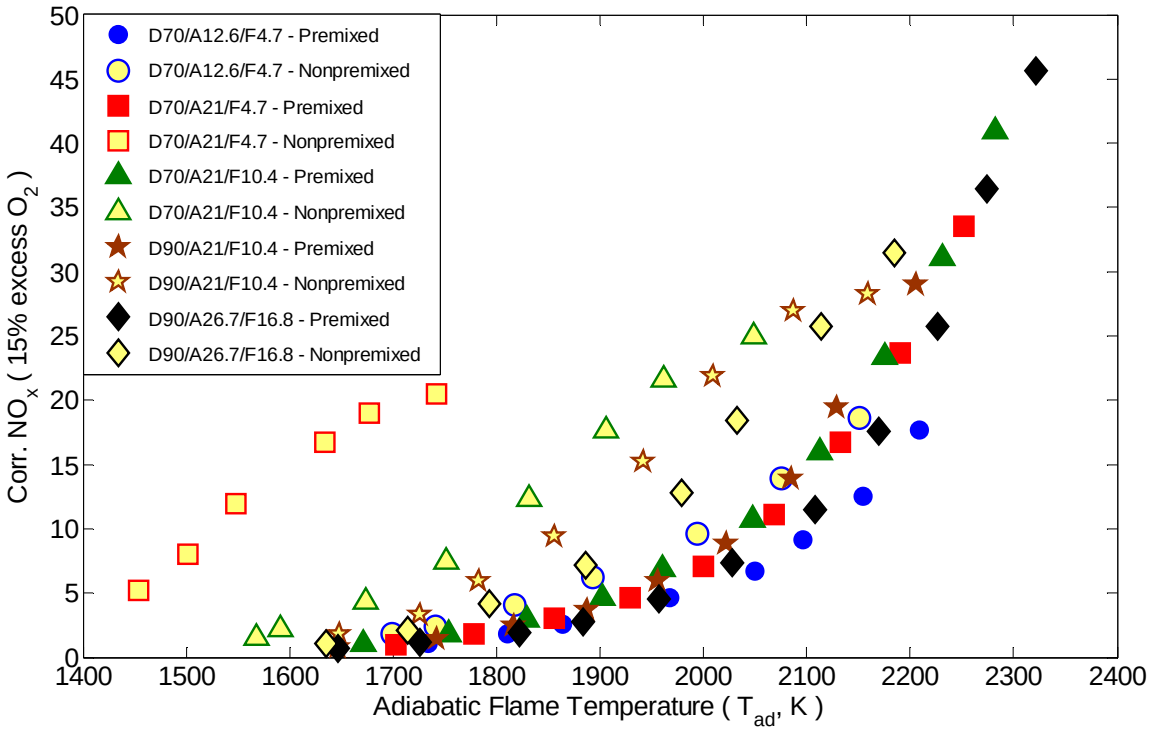

Figure 42. Variation of NOx emissions with adiabatic flame temperature based on the overall equivalence ratio and measured inlet temperature for all injector dimensions and combustor diameters explored.

To be able to scale the mixing profiles for various injectors, the axial distance is non-dimensionalized with the calculated mixing length as depicted in Figure 43 as opposed to the inner jet diameter. Using this parameter to normalize the axial distance almost collapses all the profiles on to a single curve irrespective of jet diameter and the momentum ratio.

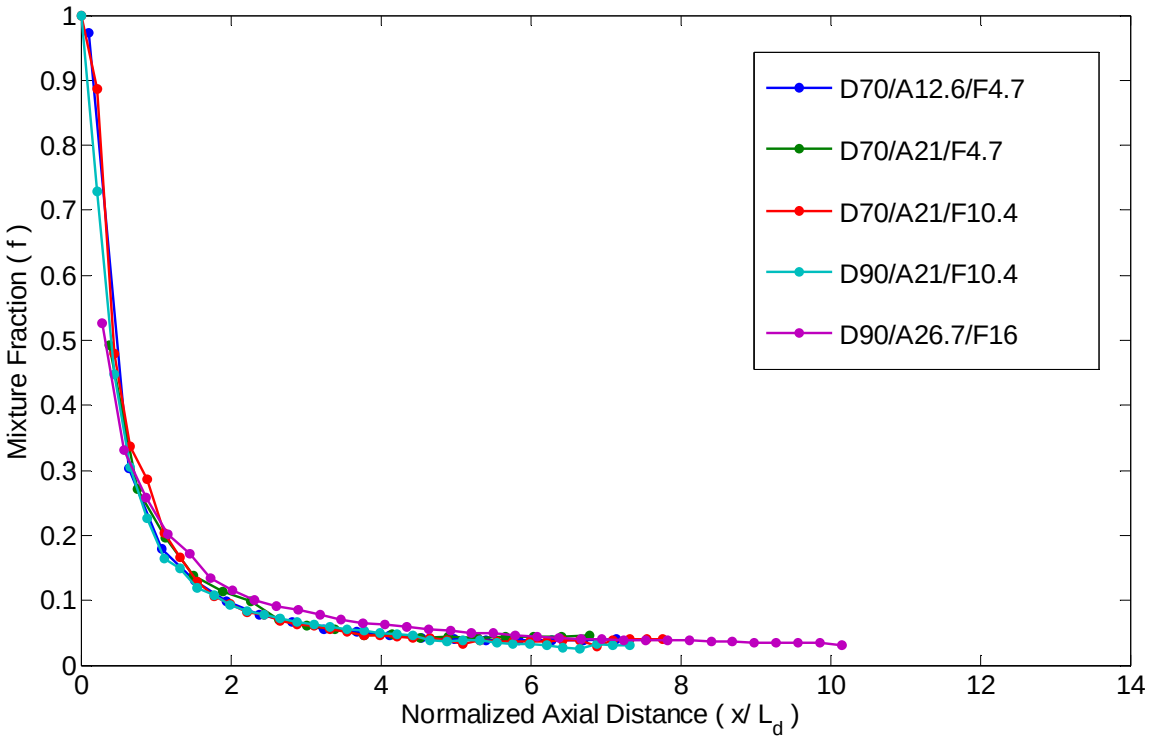

Figure 43. Mean mixture fraction variation along the combustor centerline with respect to axial distance normalized by a dilution length calculated from the model by Villermaux [24] for cases shown in Table 8.

5.3.3 Effect Combustor Length Change

Once the injector dimensions are optimized to provide mixing in a reasonably short distance, the residence time can be further controlled by varying the combustor length. The effect of reducing the combustor length (L) from 279.4 mm to as low as 152.4 mm on fuel-air mixing is shown in Figure 44. All the cases shown in the figure have a combustor diameter of 70 mm, air diameter of 21 mm and fuel tube diameter of 10.4 mm. With decreasing combustor length, the incoming jet decays more rapidly leading to shorter mixing lengths as seen in the Figure 44a. Also the amount of time available for the fuel to mix with air is reduced. This change in time available for mixing

needs to be taken into account for scaling the profiles in combustors with different lengths. With a linear correction applied to the time by scaling axial distance by combustor length, all the mixture fraction data collapse as shown in Figure 44b.

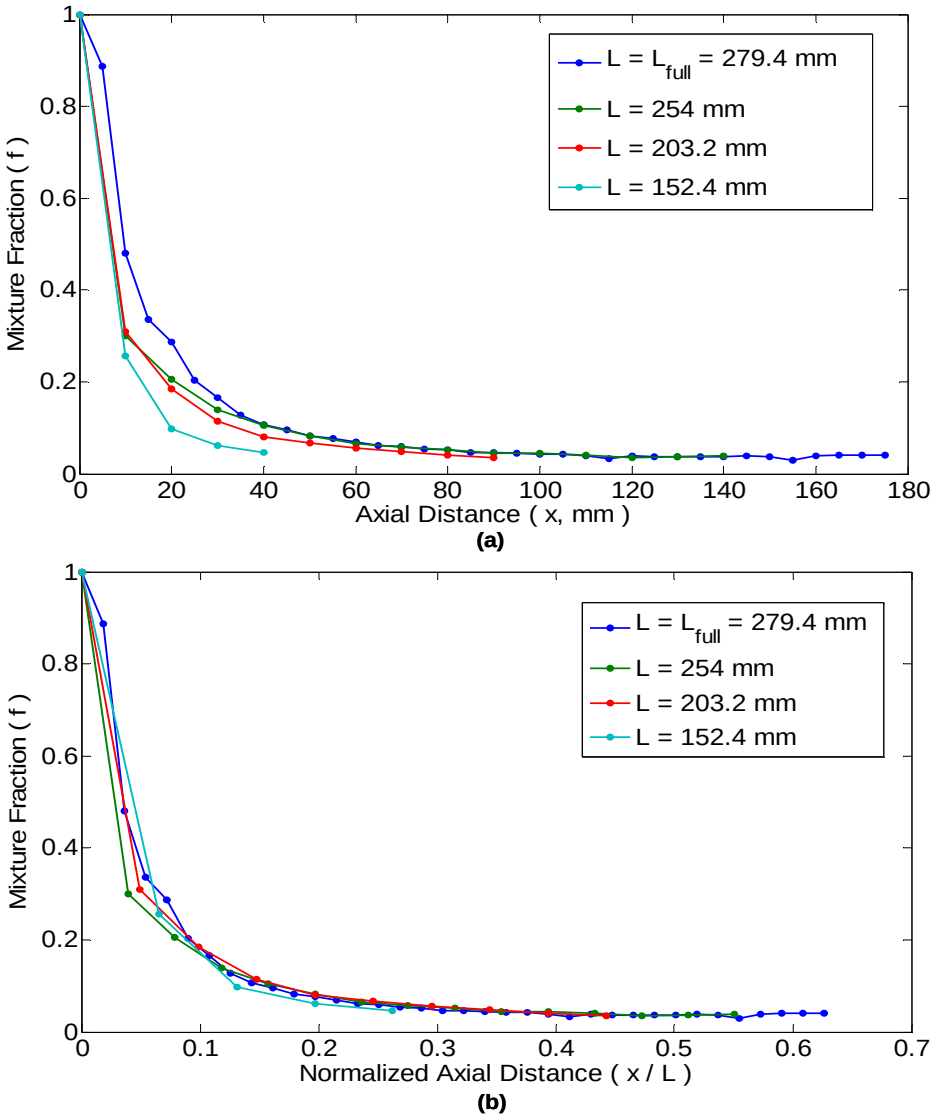

Figure 44. Profiles of mean mixture fraction shown as a function of (a) axial distance and (b) axial distance normalized by the combustor length, for 'D70/A21/F10.4' configuration operating at a loading of 8.1g/s and ϕ=0.6.

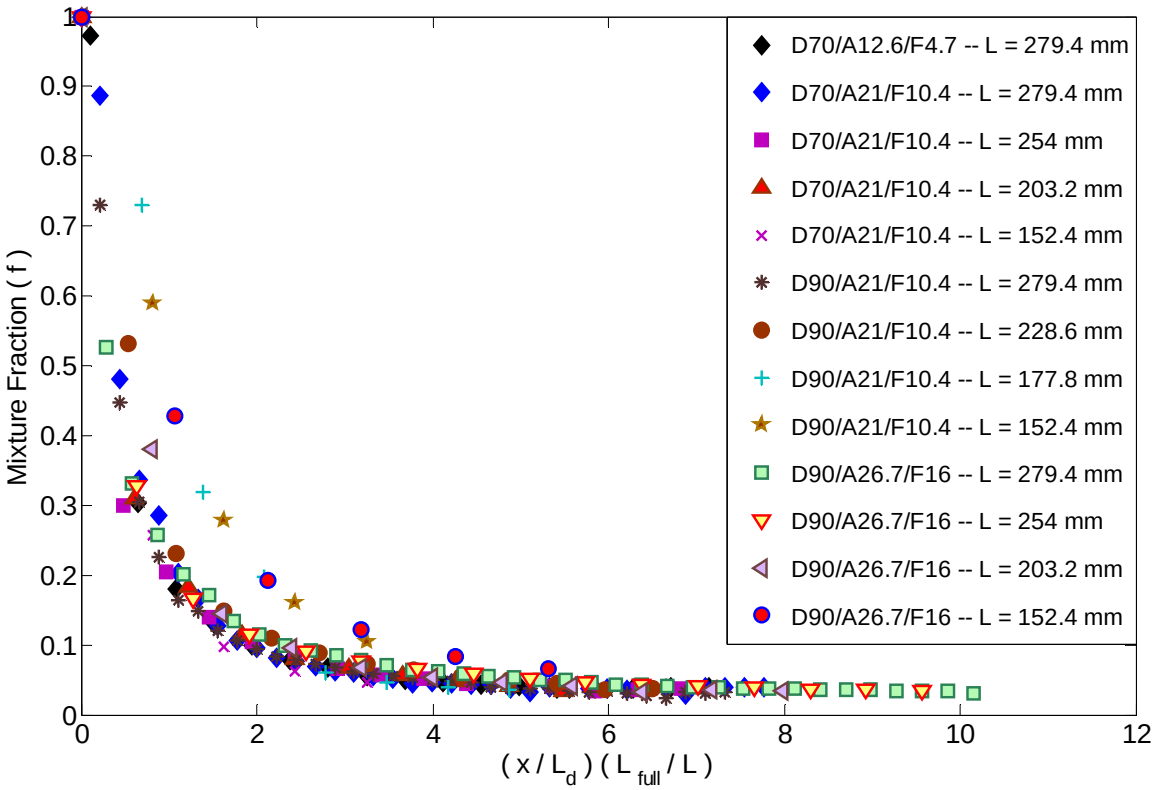

Figure 45. Measured mean mixture fraction in all the configurations tested for scaling analysis plotted against a universal scaling parameter dependent on the dilution (L_d) and the combustor lengths (L).

All the above scaling rules can be consolidated into a single parameter involving dilution length and the fraction of the combustor length with respect to the full length combustor. All the data from the various configurations is plotted against this single parameter in Figure 45. Almost all the data merges on to a single curve except for three data sets, which correspond to configurations with very short combustor lengths which are almost half the size of the full combustor and a larger combustor diameter (D_c). At these short lengths, base plate starts to have a significant effect on the near field mixing characteristics and the assumption that the injector can be modeled as a free coaxial jet is not valid. The linear correction for mixing time in these cases does not seem to hold

anymore and causes the mixing profiles to deviate from the rest of the data. Higher values of mixture fraction in these cases indicate relatively weaker mixing with decreasing combustor length. This aspect is further discussed in the next section.

5.4 Flame Liftoff and Jet Penetration Correlation

Emission performance of the non-premixed combustor depends not only on the fuel-air mixing characteristics but also on the flame lift off height. To achieve low emission levels, the flame should be lifted enough to allow complete mixing of fuel and air. Mean chemiluminescence images show the extent of flame lift-off for two different injector configurations and multiple combustor lengths in Figure 46. The 'D70/A21/F10.4' case in Figure 46a, corresponds to a combustor configuration where the mixture fraction profiles follow the scaling rule developed for geometry changes in contrast to the 'D90/A26.7/F16' case in Figure 46b with relatively weak mixing and where the profiles start to deviate for very short combustor lengths as outlined in the previous section.

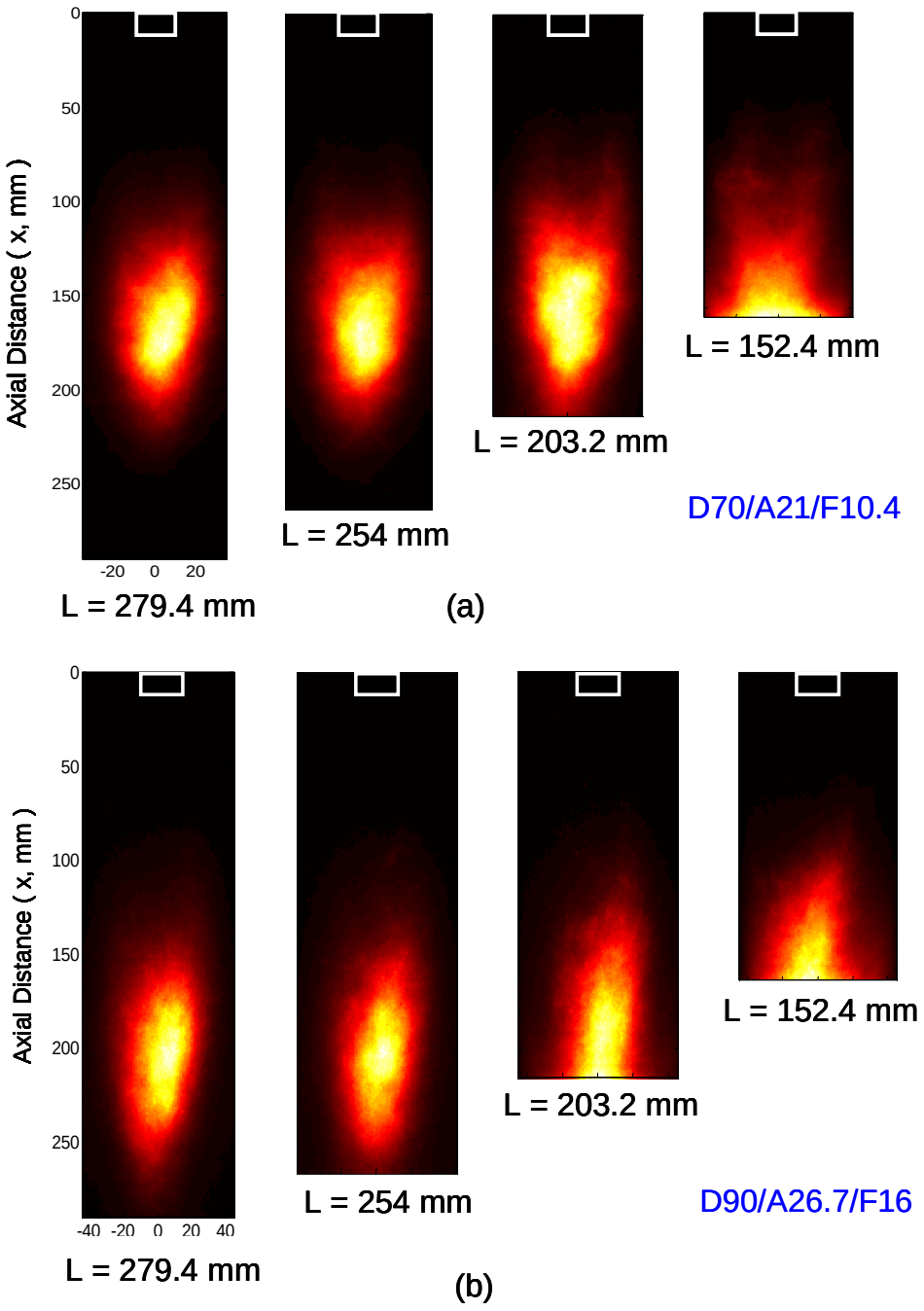

Figure 46. Mean chemiluminescence images acquired in (a) 'D70/A21/F10.4' and (b) 'D90/A26.7/F16' configurations at different combustor lengths.

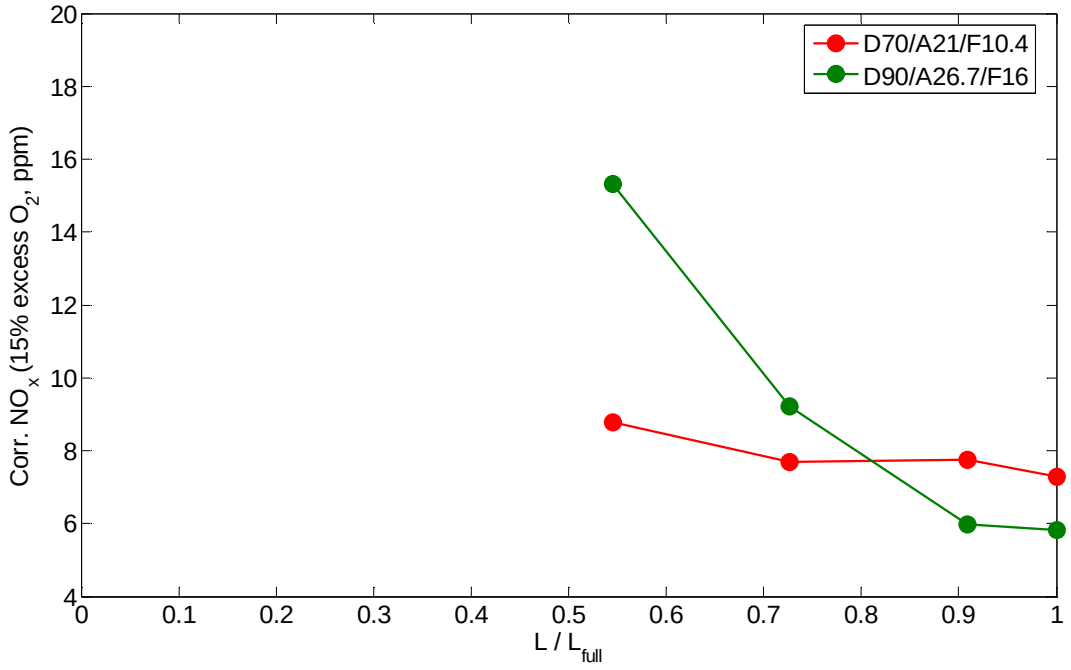

Figure 47. Variation of NOx emissions with changing combustor length as a fraction of the full combustor at a mass loading of 8.1 g/s and ϕ=0.6.

Even though the liftoff height observed for the two full length combustors is different, one of the stark differences between the cases is how liftoff height responds to the change in combustor length. For the same change in combustor length, the liftoff height in the first case is relatively invariant, as opposed to the noticeable reduction for the second case. This reduction in the liftoff height in conjunction with reduced mixing levels causes the fuel to burn at an equivalence ratio richer than the global value at short lengths. This is also reflected in the corresponding NO_x emissions measured at the exit of the combustor as reported in Figure 47. The figure shows dependence of these emissions on combustor length expressed as a fraction of the full combustor for these two geometries. For the full length combustor, the 'D90/A26.7/F16' case starts off with lower NO_x attributed to a higher momentum ratio between the air and fuel jet. However, with

reduced length, the NO_x emissions for this case start to drastically climb due to richer burning of the fuel as opposed to a minor increase in these emissions for the 'D70/A21/F10.4' combustor.

Based on arguments from the previous chapter on flame stabilization, the flame in the SPRF combustor is located at a location where the flow and flame velocities balance each other. In similar stagnation flame scenarios, like opposed jet flames [27], this location is a strong function of the momentum ratio between the impinging jets. To understand the importance of injection momentum in the SPRF combustor, the flow field is modeled as a circular jet in an ambient counter-flowing stream. In such a system, the normalized centerline penetration (x_P) of the jet into opposing flow is shown to be related to ratio of the momentum of the inlet to the return streams ($M_{a/P}$) [26].

$$\frac{x_P}{D_{a\_in}} \propto M^{\frac{1}{2}}{}_{a/P} = \sqrt{\frac{\rho_a U_a{}^2}{\rho_P U_P{}^2}}$$

In the case of the SPRF combustor, however, the momentum of the product gases is coupled with the injection conditions and is strongly dependent on the combustor diameter. The above expression is adapted to the current combustor and expressed in terms of the geometric parameters for fixed mass flow rate.

$$\frac{x_P}{D_{a\_in}} = \sqrt{\frac{\rho_P}{\rho_a}} \left(\frac{D^2{}_c - D^2{}_{a\_out}}{D^2{}_{a\_in} - D^2{}_{f\_in}} \right)$$

Penetration distances were calculated for all the different combustor configurations (injector and combustor diameter changes) used based on the assumption that the products leaving the combustor have a density equal to equilibrium products and the inlet density is based on the reactant temperature measured in the injector. The

corresponding flame liftoff height (L_f), defined as the centerline axial distance where the chemiluminescence intensity reaches 1/e of the peak chemiluminescence, were obtained from the mean chemiluminescence images. All these metrics are listed in Table 9.

Table 9. Jet penetration predictions for jet in an opposed uniform flow along with measured flame liftoff height for different SPRF configurations.

Configuration	U_a (m/s)	U_P (m/s)	D_C (mm)	D_{a_in} (mm)	$M_{a/P}$	x_P/D_{a_in}	L_f/D_{a_in}
D70/A21/F4.7	34.9	12.68	70	21	29.56	14.01	5.62
D70/A12.6F4.7	117.2	11.68	70	12.6	311.8	41.4	10.87
D70/A21/F10.4	51.59	12.68	70	21	64.56	17.04	5.8
D90/A21/F10.4	51.59	7.38	90	21	190.5	29.26	8.3
D90/A26.7/F16	40.31	7.66	90	26.7	108.2	19.62	5.75

Figure 48 shows the dependence of flame liftoff height in the full length combustors against the corresponding jet penetration distance estimated from the modified opposed jet model. We observe an increase in the flame liftoff when the momentum ratio between the inlet jet and the products is increased as in opposed jet flames. This also explain the increased liftoff in the full length combustor for the high momentum ratio 'D90/A26.7/F16' case compared to the low momentum ratio case of 'D70/A21/F10.4' in Figure 47. The flame liftoff seems to be reasonably well correlated with jet penetration and this information can be used to predict trends when combustor geometry is modified. However along with jet penetration, flame liftoff is also dependent on product entrainment levels and the flow field changes due to heat release. Hence, these

issues would also need to be accounted for to achieve better quantitative predictions of the liftoff height.

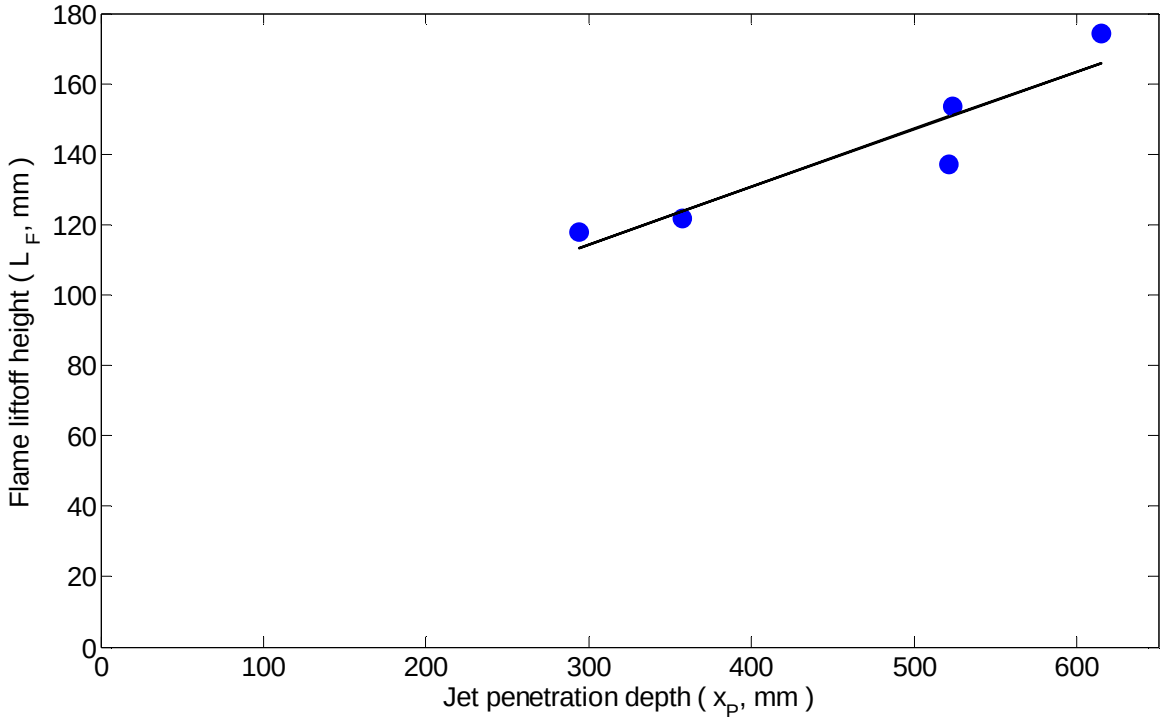

Figure 48. Measured flame liftoff height in all the tested full length SPRF configurations correlated with the corresponding jet penetration estimated from the jet against uniform flow model [26].

CHAPTER 6

CONCLUSIONS AND FUTURE RECOMMENDATIONS

6.1 Summary and Conclusions

The mixing and combustion characteristics of the SPRF combustor operating at atmospheric pressure have been examined in order to determine how the combustor is able to operate stably at very lean (low temperature) conditions and to produce low emissions even in nonpremixed operation. Various optical diagnostic techniques, specifically Particle Image Velocimetry (PIV), OH PLIF, chemiluminescence imaging and Spontaneous Raman Scattering (SRS) were employed for this purpose.

Measurements of the velocity field in both premixed and non-premixed modes show a low average velocity zone with high levels of turbulence in the bottom half of the combustor. Based on the geometry of the combustor, this zone is expected to exist over a range of flow conditions (except for very low loadings where the flow is laminar and combustion occurs before reaching the "stagnation zone"). Chemiluminescence and OH PLIF fields indicate that the flame is indeed anchored in this region of high turbulence intensity, and that this is where most of the heat release occurs. This results in stable operation of the combustor even at high loadings and very lean equivalence ratios.

Raman concentration measurements show entrainment of hot products from about 5 injector diameters into the combustor reaching an average reactant temperature of ~1300K just before the flame zone. This tends to increase chemical reactivity, especially of lean mixtures. Although the reaction rates are elevated due to product entrainment, the

reactant mixture does not autoignite as in mild combustion due to residence times that are relatively low compared to the characteristic ignition times in the reactant/product mixture. An analysis of the turbulent combustion structure in the premixed SPRF combustor indicates that the flame is primarily in the thin reaction zone regime throughout most of the combustor. However, the flame tends to become more flamelet like farther from the injector, due to increases in the turbulent length scales and increases in the chemical rates due to entrainment of heated products and radicals into the reactants.

Fuel and air injected separately in the non-premixed mode are found to mix rapidly after entering the combustor, before significant mixing with hot products has occurred. The extent of hot product gas entrainment into the reactants before the flame zone is also found to mimic the profiles of the premixed combustor. The ability for fuel and air to internally premix is facilitated by the large flame standoff observed in the non-premixed case. In addition, laminar flame calculations indicate that the entrainment of (adiabatic) products is not directly responsible for the low NO_x emissions at a given overall fuel-air ratio, but rather, is likely to contribute to a slight increase in NO_x levels compared to a system with no product entrainment. This provides further evidence that the comparable NO_x emission levels observed for both modes is due to good mixing of fuel and air in the baseline configuration, rather than an influence of recirculation of hot products on the NOx chemistry.

These mixing characteristics, however, are found to be particularly sensitive to changes in injector geometry. Increasing the size of the outer (air) tube of the injector decreases the air velocity, adversely affecting the fuel-air mixing characteristics. The

product entrainment rates are also diminished in this case, illustrated by the appearance of hot products later in the combustor along the centerline. This reduced mixing resulting from the lower air velocity, confirmed not just on an average sense but also with time resolved measurements (SRS scatter plots), should cause the fuel to burn in mixtures richer than the global stoichiometry, thereby increasing the NOx emissions.

The effect of changing combustor geometry, specifically combustor length and diameter in addition to injector dimensions, on fuel-air mixing was also investigated. Varying the combustor diameter, in the range tested, has little effect on fuel-air mixing characteristics. This suggests that mixing in the near field of the injector is not influenced by the returning product stream and can be modeled as a free coaxial jet system. The mixing quality represented by a dilution length in such a configuration is dependent only on the ratio of air to fuel momentum. Hence, mixing levels similar to the baseline configuration should be obtainable at lower injection velocities (and thus lower pressure drops), by reducing the air and fuel velocities proportionately. With reduced combustor length, fuel and air also mix in a shorter distances, due to a faster decay of the reactant jet velocity. A linear correction in terms of fractional change in combustor length, applied to account for the change in time available for mixing, was able to capture the variation in this mixing length. Mixture fraction profiles, representative of fuel dilution in the combustor, were therefore shown to follow a universal scaling for changes in combustor length, combustor diameter and injector dimensions. A few configurations with very short lengths (half the baseline combustor length) and low injection momentum were found to deviate from the scaling rule, but were also found to produce high NOx emission levels. The flame liftoff distance was seen to be another important parameter for

determining NOx emission performance in the non-premixed SPRF combustor. A qualitative correlation between this liftoff distance and penetration of the reactant jet was obtained using a simplified opposed jet model.

In summary, the geometry of the SPRF combustor creates a combination of a low velocity, high turbulence region, "the stagnation point," and internal product recirculation due to the "the reverse flow" that creates a stable combustion process under a large range of combustor operating conditions. Low emission levels in the non-premixed mode are attributed to shielding of fuel from the hot products, and efficient mixing of most of the fuel and air (and some products) before combustion occurs. Combustor geometry scaling rules based on coaxial jet and opposed jet models that are needed to ensure good fuel-air mixing in the non-premixed SPRF combustor, have been developed.

6.2 Future Work

Although this thesis provides the basis for a comprehensive understanding of the operation of the SPRF combustor, many aspects of its performance need to be studied further. Detailed measurements of the mixing field have been performed in the SPRF combustor, but the fluid mechanic aspects, like turbulence generation, responsible for this mixing process have not been addressed here. Relative roles of the turbulence generated by various features like shear layer between the opposed streams, the stagnation zone and velocity fluctuations due to the unsteady heat release can be quantified by extending the velocity measurements to a wider range of configurations. Also modifications in combustor flow field at very short combustor lengths may provide insight into the effect of confinement on the injector near-field mixing characteristics and help develop a better combustor length scaling rule. In addition scaling rules developed for changes in

combustor geometry presented here have to be extended to account for changes in mass loading and higher pressures as well.

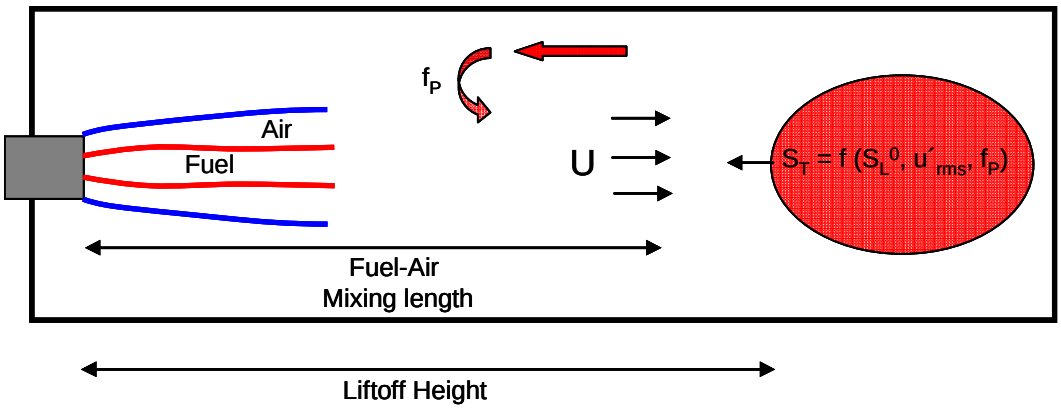

Figure 49. Schematic of different processes controlling the emission performance in the SPRF combustor.

For example, it is important to examine how the processes in the atmospheric burner scale with pressure. In high pressure operation, as indicated in Figure 49, the injected fuel will still need to mix well with the air before encountering the flame. For a combustor with the same geometry and injection velocities (i.e. though at higher *Re* due to the density increase), the jet penetration and mixing lengths are not expected to change significantly as they are a function of only the corresponding momentum ratios. On the other hand, flame liftoff height (determined by a balance of the flow and flame propagation velocities) is a function of the laminar propagation speeds, turbulence levels and product entrainment levels into this zone. At high pressure conditions, the laminar flame speeds for methane (or natural gas) are lower, which would cause the flame to liftoff further than at atmospheric conditions. With additional knowledge about how the turbulence generation and product entrainment are affected, more accurate predictions can be made. Along with the predictions of the mixture preparation before burning, the

impact on chemical kinetics of increasing pressure is also important. Increased pressures will tend to increase reaction rates, which reduces the time available for mixing to occur. The influence of pressure on flame front NO_x production also needs to be addressed.

Further, this thesis primarily deals with combustor operation only at very lean conditions where almost all the NO_x is produced at the flame front and this is found to be insensitive to product entrainment levels. However, for combustors operating closer to stoichiometric conditions, thermal NO_x produced is also important. The effect of recirculation of hot or partially cooled product gases on this NO_x produced in the post flame region should also be investigated. This is relevant for applications like boilers, where fuel is burned at near (overall) stoichiometric proportions in order to obtain high thermal efficiency. Also of importance in such systems is the combustor heat loss, which was minimal for the SPRF configuration employed in this work. Further experimentation on the SPRF combustor with cooled walls can be used to understand how the stability and emission performance is dependent on these heat losses. Moreover, flame stabilization and mixing characteristics provided in this thesis could potentially be used to model the combustor operation with a network of appropriate reactor and flame elements that would be able to predict blowout equivalence ratios and emission levels.

The SPRF combustor used for this work is a simplified device; various ways to adapt this new technology for implementation in a real gas turbine should be explored. In addition, the understanding developed here needs to be extended to operation with liquid fuels like Jet-A, and to realistic high pressure conditions seen in typical gas turbines. Ability of the SPRF combustor to operate stably at ultra lean equivalence ratios makes

this technology an exciting possibility to burn non-conventional low BTU fuels like biomass gas effectively.

APPENDIX A

RAMAN MEASUREMENT UNCERTAINITIES

Various sources of error that introduce discrepancies in the instantaneous SRS measurements have been identified in literature. The most prominent among these are due to (a) variation in laser power, (b) inherent noise in the detection scheme, (c) steering of the incident beam due to gradients in density in the combustor, (d) interference from fluorescence signals and (e) neglecting minor species such as CO in the measurement volume.

The Spectra Physics Nd:YAG (Quanta Ray Pro 250) laser used for these measurements is capable of providing a relatively steady power to within 2% of the mean value of 250 mJ/pulse. At low light levels typical in Raman scattering measurements, noise from the detection system is primarily due to shot noise arising from statistical variation in the number of detected photons. The combined error due to these two effects in the current setup was estimated from measurements taken in ambient air which has a steady and known composition. The calculated instantaneous mole fractions of O_2 and N_2 varied within 3% of the standard atmospheric composition.

In closing the system of equations to solve for mole fractions of the major species and temperature, it is assumed that concentration of the minor species (notably CO) is negligible. However, this might not be true in gas mixtures with composition close to stoichiometric values. This effect of neglecting minor species in determining the major species mole fractions is estimated from equilibrium calculations presented in Figure 50. As shown, the percentage error in calculated mole fractions of the major species is

typically under 5% of the equilibrium value and increases with equivalence ratio. All measurements presented in this thesis were acquired in gas mixtures with equivalence ratio of 0.6, where these errors are less than one percent.

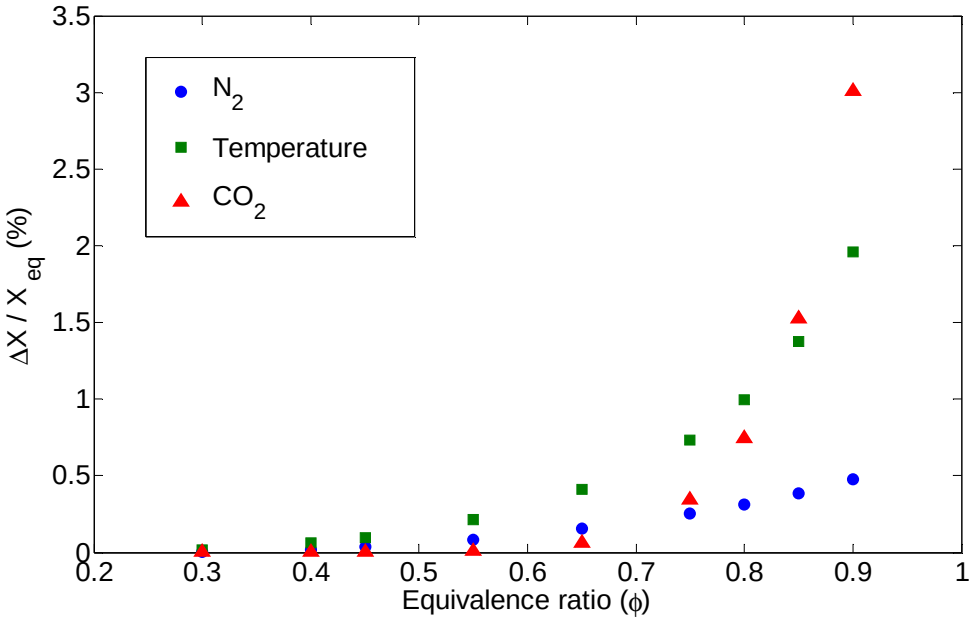

Figure 50. Percentage error in calculated mole fractions and Temperature due to neglecting minor species.

Further, the laser beam introduced into the combustor encounters regions of varying density causing it to deviate from the initial path. This deviation is estimated by modeling the worst case scenario where the beam arrives at an interface between reactants (450 K) and hot products (1800 K) at grazing incidence. The resultant maximum displacement due to steering of the beam was found to be within dimensions of the probe volume suggesting these errors are negligible. Lastly, as all measurements were made at lean operating conditions (ϕ=0.6) where the concentrations of heavy hydrocarbons such as PAH's are negligible, non-resonant fluorescence interactions from these species are insignificant.

The cumulative effect of all the aforementioned errors on the mole fractions of various species at different temperatures is tabulated in Table 10.

Table 10. Cumulative errors in measurement of major species mole fractions and temperature at different temperatures

	450 K	1000 K	1700 K
CO_2	6.6 %	9.9 %	12.9 %
O_2	7 %	10 %	13.1 %
CH_4	5.8 %	8.7 %	11.3 %
T	5 %	7.7 %	10 %

APPENDIX B

FLOW SYSTEM CALIBRATION

The flow rates of natural gas and air injected into the combustor were monitored using rotameters. The fuel flowmeter (Dwyer RMC-102-SSV) could measure flow rates ranging from 10-100 SCFH while the air flowmeter (Dwyer RMC-107) had a range of 120-1200 SCFH. They were calibrated by connecting them in series with a pressure gauge and a Ritter TG25-5 drum-type gas meter. This device is used to measure the gas flow rate by timing the rotation of the drum. Air was sent at several constant flow rates and the corresponding pressure readings were noted and corrected for. In addition to the pressure correction, flow rates for the fuel flowmeter were also corrected for the difference in molecular weight.

The actual flow rate measured by the drum-type gas meter is plotted against the flowmeter readings corrected for pressure and molecular weight in Figure 51. The corrected flow rates, in case of the fuel flowmeter, were found to correlate well with the actual flow rate. However for the air flowmeter (Figure 51b), the corrected values ($\dot{Q}_{corr}$) deviate slightly from the actual flow rates ($\dot{Q}_{actual}$) necessitating a further correction given by

$$\dot{Q}_{actual} = 1.0114 \ \dot{Q}_{corr} + 16.626$$

The calibration was also verified using a Horiba gas analyzer. The ratio of air to fuel flow rates obtained from the product composition measured at the exit of the

premixed SPRF combustor was found to match the values from the rotameter calibration closely.

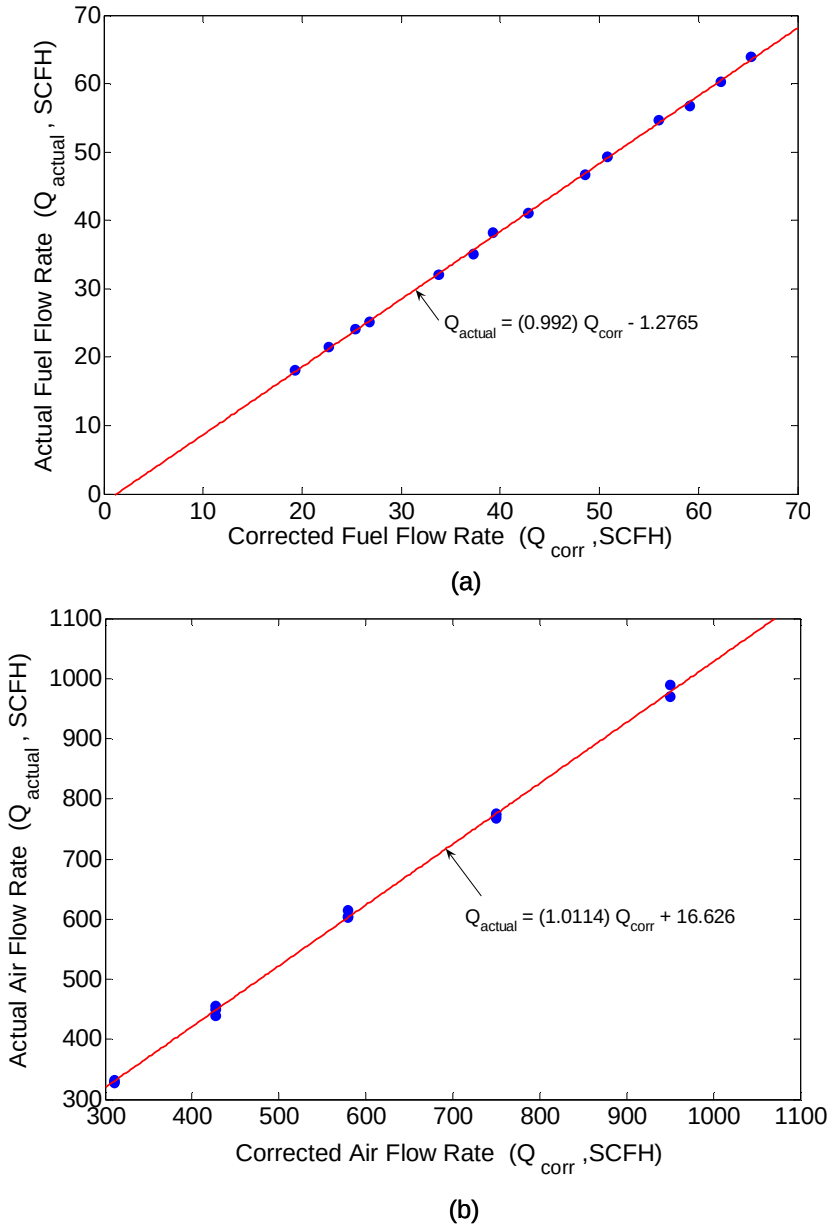

Figure 51. Comparison of the actual flow rates with respect to ball reading corrected for pressure and molecular weight for (a) fuel and (b) air rotameters.

REFERENCES

[1] Miller, J. A., and Bowman, C. T., "Mechanism and modeling of nitrogen chemistry in combustion," *Progress in Energy and Combustion Science*, Vol. 15, 1989, pp. 287–338.

[2] Hayhurst, A. N.; Lawrence, A. D., "Emissions of nitrous oxide from combustion sources", *Prog. Energy Combust.* Sci., 1992, 18, 529-552.

[3] Zeldovich, J., "The oxidation of nitrogen in combustion and explosions", Acta. Physiochem., 21(4), 1946.

[4] Kim, S-H., Yoon, Y. and Jeung, I-S., "Nitrogen oxides emissions in turbulent hydrogen jet non-premixed flames: Effects of coaxial air and flame radiation", Proc. Combust. Inst., 28: p463-470, 2000.

[5] Smart J P, Morgan D J, "The effectiveness of multi fuel reburning in an internally staged burner of NOx reduction", Fuel 73, pg 1437-1442, 1994

[6] Spliethoff H., Greul U., Rudiger H. and Hen K. R. G., "Basic effects of NO_x emissions in air staging and reburning at a bench scale test facility", Fuel, 75, pg 560-564, 1996.

[7] Arai, M., "Flue gas recirculation for low NO_x combustion system", Proceedings of 2000 International Joint Power Generation Conference Miami Beach, Florida, vol. 7, 2000.

[8] Neumeier, Y., Weksler, Y., Zinn, B. T., Seitzman, J. M., Jagoda, J. and Kenny, J., "Ultra low emissions combustor with non-premixed reactants injection," AIAA 2005-3775 41st AIAA/ASME/SAE/ASEE Joint Propulsion Conference & Exhibit 10 - 13 July 2005, Tucson, Arizona.

[9] Smith, G. P., Golden, D. M., Frenklach, M., Moriarty, N. W., Eiteneer, B., Goldenberg, M., Bowman, C. T., Hanson, R. K., Song, S., Gardiner Jr.,W. C., Lissianski, V., and Qin, Z., GRI-Mech homepage, Gas Research Institute, Chicago, 1999, www.me.berkeley.edu/ gri_mech/.

[10] Henry C. Barnett, Robert R. Hibbard, "Basic considerations in the combustion of hydrocarbon fuels with air", Naca-report-1300, Jan 1957.

[11] Gupta, A.K. Bolz, S. and Hasegawa, T, "Effect of air preheat and oxygen concentration on flame structure and emission", Proc. ASME J. Energy Resources and Technology, Vol. 121, September, 1999, pp. 209-216.

[12] Gupta, A. K., "Flame characteristics with high temperature air combustion,"

AIAA-2000-0593, 38th Aerospace Sciences Meeting & Exhibit, January 2000.

[13] J. R. Kalb and T. Sattelmayer, "Lean blowout limit and NO_x production of a premixed sub-ppm NO_x burner with periodic flue gas recirculation," GT 2004-53410, Proceedings of ASME Turbo Expo 2004.

[14] Driscoll, J. F., Chen, R-H. and Yoon, Y., "Nitric oxide levels of turbulent jet diffusion flames: Effects of residence time and Damkohler number", Combust. Flame, 88, pp 37-49, 1992.

[15] Wünning, J. A., and Wünning, J. G., "Flameless oxidation to reduce thermal NO-formation", Progress in Energy and Combustion Science, Vol. 23, 1997, pp.81-94.

[16] Hawthorne, W. R., Weddell D. S., and Hottel H. C., "Mixing and combustion in turbulent gas jets", Proc. Combust. Inst,. 3, pp 266–288, 1948.

[17] Ricou, F. P. and Spalding D. B., "Measurements of entrainment by axisymmetrical turbulent jets", Journal of Fluid Mechanics, 11, pp 21–32, 1961.

[18] Vanquickenborne, I. and Van Tiggelen A., "The stabilization mechanism of lifted diffusion flames", Combustion and Flame, 10, pp 59–69, 1966.

[19] Effelsberg, E. and Peters N., "Scalar dissipation rates in turbulent jets and jet diffusion flames", Proc. Combust. Inst. 22, pp 693–700, 1988.

[20] Muniz, L. and M. G. Mungal, "Instantaneous flame-stabilization velocities in lifted-jet diffusion flames," Combustion and Flame, 111 (1-2), pp 16-31, 1997.

[21] Donghee Han, "Study of turbulent nonpremixed jet flames using simultaneous measurements of velocity and CH distribution", Ph. D Thesis, Stanford University, 2001

[22] Reza Sadr, "An experimental investigation of the near-field flow development in coaxial jets", Physics of Fluids, Vol. 15, No. 5, 2003.

[23] A. S. H. Kwan and N. W. M. Ko, ''The initial region of subsonic coaxial jets. Part 2'', J. Fluid Mech. 82, 273, 1977.

[24] Villermaux E., and Rehab D. H., "Mixing in coaxial jets", Journal of Fluid Mechanics, Vol. 425, p 161, 2000.

[25] Beltaos S. and Rajaratnam N., "Circular turbulent jet in an opposing infinite stream", Proc. 1st Can. Hydrotechnical Conf., Edmonton, Cananda, 220-237, 1973.

[26] Lam K. M., and Chan C. H. C., "Time-averaged mixing behavior of circular jet in

counterflow: velocity and concentration measurements", Journal of hydraulic engineering, vol. 128, p 861, 2002.

[27] Beltaos S., "Turbulent impinging jets", PhD thesis, Dept. of Civil Engineering, University of Alberta, Edmonton, Canada, 1974.

[28] Lam K. M., and Chan C. H. C., "Round jet in ambient counterflowing stream", Journal of hydraulic engineering, vol. 123, p 895, 1997.

[29] Adrian, R.J., "Particle-imaging techniques for experimental fluid mechanics," Annual Review of Fluid Mechanics, 22, pp 261-304, 1991.

[30] P. Griebel, R. Bombach, A. Inauen, R. Schären, S.,Schenker, P. Siewert, "Flame Characteristics And Turbulent Flame Speeds Of Turbulent, High-Pressure," Lean Premixed Methane/Air Flames, GT2005-68565, Proceedings of GT2005 ASME Turbo Expo 2005: Power for Land, Sea, and Air June 6-9, 2005, Reno-Tahoe, Nevada, USA.

[31] Seitzman, J. M. and Hanson, R. K. "Planar fluorescence imaging in gases: Instrumentation for Flows with Combustion", ed. A. M. K. P. Taylor, 1993.

[32] Cessou A., Meier U. and Stepowski D., "Applications of planar laser induced fluorescence in turbulent reacting flows," Meas. Sci. Technol., Vol. 11**,** 2000, 887–901.

[33] Sutton J. A. and Driscoll J. F., "Optimization of CH fluorescence diagnostics in flames: range of applicability and improvements with hydrogen addition," Applied Optics, Vol. 42, No. 5, pp 2819-2828, 2003.

[34] V. Nori and J. Seitzman, "Chemiluminescence Measurements and Modeling in Syngas, Methane and Jet-A Fueled Combustors," paper AIAA-2007-0466 at the 45th Aerospace Sciences Meeting, Reno, NV, Jan 8-11, 2007.

[35] R. Morrell, J. Seitzman, M. Wilensky, J. Lee, E. Lubarsky, , and B. Zinn, "Interpretation of Optical Flame Emissions for Sensors in Liquid-Fueled Combustors," paper AIAA-2001-0787 at the 39th AIAA Aerospace Sciences Meeting, Reno, NV, January 8-11, 2001.

[36] Nooren P A, Versluis M, van der Meer T H, Barlow R S and Frank J H, "Raman–Rayleigh–LIF measurements of temperature and species concentrations in the Delft piloted turbulent jet diffusion flame," Appl. Phys. B, 71, 2000, 95–111

[37] Eckbreth, A. C.,"Laser diagnostics for combustion temperature and species", (second ed.). Amsterdam, Netherlands: Gordon and Breach, 1996.

[38] Lederman S., "The use of laser Raman diagnostics in flow fields and combustion," Prog. Energy Combust. Sci., 3, pp 1-34, 1977.

[39] Masri A. R., Dibble R. W., and Barlow R. S., "Chemical kinetic effects in nonpremixed flames of H_2/CO_2 fuel", Combustion and Flame, Vol. 91, 0285, 1992.

[40] Cheng, T. S., Wehrmeyer, J. A. and Pitz, R. W., "Simultaneous temperature and multispecies measurement in a lifted hydrogen diffusion flame", Combustion and Flame, 91, pp 323, 1992.

[41] Lipp F., Hartick J., Hassel E. P. and Janicka J., "Comparison of UV Raman Scattering Measurements in a Turbulent Diffusion Flame with Reynolds-Stress Model Predictions", Twenty-Fourth Symposium (International) on Combustion, pp.287-294, 1992.

[42] Gulati, A. and Correa, S. M., "Local extinction due to turbulence in non-premixed flames", AIAA/SAE/ASME/ASEE 23rd Joint Propulsion Conference, AIAA 87-1717, 1987.

[43] A. R. Masri, R. W. Dibble and R. S. Barlow, "The structure of turbulent nonpremixed flame revealed by Raman-Rayleigh-LIF measurements", Prog. Energy and Combust. Sci., Vol. 22, pp. 307-362, 1996.

[44] Nguyen, Q V., Dibble, R. W., Carter, C. D., Fiechtner, G. J. and Barlow, R. S., "Raman-LIF measurements of temperature, major species, OH, and NO in a methane-air bunsen flame", Combustion and Flame, 105, pp 499, 1996.

[45] David F. Marran, Jonathan H. Frank, Marshall B. Long, Sten H. Starner and Robert W. Bilger, "Intracavity technique for improved Raman/ Rayleigh imaging in flames", Optics Letters, vol. 20, No. 7, 1995.

[46] Paul P. H., Cruyningen I. van, Hanson R. K., and Kychakoff G.,"High resolution digital flowfield imaging of jets", Experiments in Fluids, vol. 9, p241, 1990

[47 Borghi R., "Recent Advances in Aerospace Science", ed C Bruno and S Casci, p. 117, 1985.

[48] Peters, N., "The turbulent burning velocity for large-scale and small-scale turbulence", Journal of Fluid Mechanics, 384, pp 107-132, 1999.

[49] Bilger, R. W., "The structure of turbulent non-premixed flames", Twenty-Second Symposium (International) on Combustion, The Combustion Institute, Pittsburgh, 1988.